

Versuchsanstalt für Wasserbau
Hydrologie und Glaziologie
der Eidgenössischen
Technischen Hochschule Zürich

Mitteilungen

212

**Seismic Activity on Gornergletscher
During Gornersee Outburst Floods**

Fabian Walter

Zürich, 2009

Herausgeber: Prof. Dr. Robert Boes

Zitiervorschlag für VAW-Mitteilungen:

Walter, F. (2009).

Seismic Activity on Gornergletscher During Gornersee Outburst Floods

Mitteilungen 212, Versuchsanstalt für Wasserbau, Hydrologie und Glaziologie (VAW),

R. Boes, Hrsg., ETH Zürich.

Im Eigenverlag der
Versuchsanstalt für Wasserbau,
Hydrologie und Glaziologie
ETH Zürich
CH-8092 Zürich

Tel.: +41 - 44 - 632 4091

Fax: +41 - 44 - 632 1192

e-mail: info@vaw.baug.ethz.ch

Zürich, 2009

ISSN 0374-0056

Preface

This PhD thesis of Fabian Walter was undertaken as part of a large collaborative SNF project on the processes triggering the sudden outburst of glacier dammed lakes (termed jökulhlaup in the glaciological literature). Prior to or during the outburst event, hydrofracturing of glacier ice can contribute substantially to englacial water channel formation. Furthermore, basal motion may lead to fracturing of basal ice layers when lake water suddenly penetrates into the subglacial drainage system. The goal of this study was to monitor the seismic activity during a jökulhlaup using high-density seismic networks in order to identify the key processes leading to the initiation of the drainage event.

An important new aspect of this study is the use of seismic moment tensors to characterize selected icequake sources. The main result was the identification of two fracture modes within the ice: tensile and shear dislocations. The author estimates that 99% of all recorded events are tensile dislocations. Surprisingly, this fracture mode appears not only at the glacier surface, but also at intermediate depths and at the glacier base. It is suggested that the basal events occur during the rapid closure of draining water-filled cavities. The shear dislocation events were located near the surface. Although only a dozen such events were found, it shows that glacier ice can also fail under shear straining, which is an interesting result.

It was expected that the outburst floods influence the basal seismicity. Interestingly, the basal seismic events occurred at low or decreasing water pressures. This suggests that these signals are emitted during fracturing of the basal ice layer when the glacier couples to its bed after periods of water-pressure-enhanced basal motion.

The identified link between the fracture processes within Gornergletscher and the outbursts floods of Gornensee was somewhat surprising: contrary to our expectations, the author found that the lake drainage inhibits basal seismicity rather than favoring it. While the presence of tensile seismic sources at intermediate depths are strong indicators that ice fracturing occurs because pressurized water within the glacier reduces the effective pressure to allow for the extension of tensile cracks (process termed "hydrofracturing"), the author's results show that fracturing as a consequence of changes in glacier sliding more effectively emits seismic energy than hydrofracturing. As the author claims, this does not mean that hydrofracturing does not occur, especially at the beginning of the lake drainage, in connection with the breaching of the seal. It is possible that the concurrent increase of surface seismicity simply masks other types of seismic signals and prohibits the detection of basal icequakes.

This study was performed in close collaboration with the Institute of Geophysics at ETH Zurich. The strong support of Dr. N. Deichmann, Dr. J. Clinton and Prof. Dr. D. Giardini is greatly acknowledged. This study was supported by the Swiss National Science Foundation (Grants 200021-103882/1 and 200020-111892/1).

Zurich, February 2009

Martin Funk

Contents

List of Figures	vii
List of Tables	ix
Abstract	xi
Zusammenfassung	xiii
1 Introduction	1
1.1 Context	1
1.2 Aim	2
1.3 Thesis Outline	2
2 Icequake Moment Tensors	3
2.1 Introduction	4
2.2 Field Investigations and Instrumentation	6
2.2.1 Study of Gornersee Outburst Floods	6
2.3 Icequake Waveform Discrimination and Locations	8
2.3.1 Characteristics of near-surface events	9
2.3.2 Characteristics of Deep Icequakes	9
2.4 Moment Tensor Inversions	12
2.4.1 Motivation for Study of Various Source Types	12
2.4.2 Numerical Tools	14
2.4.3 Moment Tensor Inversion for Icequakes	14
2.5 Discussion of Inversion Results	17
2.5.1 Inversion of Explosion Signals	17
2.5.2 Source Discrimination	19
2.6 Discussion	30
2.7 Conclusion	32

3	Moment Tensors of a Basal Icequake Cluster	35
3.1	Introduction	36
3.2	Study Site	38
3.3	Basal Icequakes	40
3.4	Inversion Scheme	43
3.4.1	Formulation of Inverse Problem	43
3.4.2	3D Moment Tensor Inversion	44
3.5	Sensitivity to Velocity Model	45
3.6	Results of Full Moment Tensor Inversion	51
3.7	Results of Tensile Crack Moment Tensor Inversion	55
3.8	Discussion	58
4	Temporal Evolution of Basal Icequake Activity	61
4.1	Introduction	62
4.2	Field site	64
4.3	Seismic Setup and Instrumentation	64
4.3.1	2004 configuration	65
4.3.2	2006 configuration	68
4.4	Seismic data	68
4.4.1	Identification of deep events	68
4.4.2	Hypocenter location procedure	69
4.5	Results	69
4.5.1	Deep icequake locations	69
4.5.2	Icequake activity	70
4.5.3	Background glacier seismicity (2004)	73
4.5.4	Diurnal activity	74
4.6	Discussion	75
4.6.1	Comparison with basal water pressure	75
4.6.2	Comparison with surface motion	77
4.6.3	Source mechanism	79
4.6.4	Basal processes	79
4.7	Conclusion	82

5 Outlook	85
5.1 Overview of Future Work	85
5.2 2007 Data Set	86
5.2.1 2007 Seismic Array	87
5.2.2 2007 Basal Icequakes: Results	87
5.2.3 Basal Cluster 2007: Future Work	89
5.2.4 2007 Calving Event	89
5.2.5 Seismicity During 2007 Calving Event	89
5.2.6 2007 Calving Event: Future Work	90
5.2.7 Seismic Noise Cross-Correlation with 2007 Continuous Data . . .	90
5.2.8 Noise Correlation: Future Work	92
5.3 Array Techniques	93
5.3.1 Array Techniques: Future Work	94
6 Conclusion	97
A Decomposition of Tensile Crack Moment Tensor	101
B Results of Moment Tensor Inversion of Chapter 2	102
C Moment Tensor Inversion Scheme Using Vector Dipoles	104
D Overview of Seismic Measurements	106
D.1 Seismic Networks	106
D.2 Seismic Data	109
E Instrumentation	115
E.1 Specification of Selected Components	121
E.2 Seismometer Specification	122
F Description of Software	124
F.1 Data Processing	124
F.2 Location and Waveform Discrimination	125
F.3 Waveform Modelling	125
Bibliography	127
Acknowledgements	135

List of Figures

2.1	Overview of Gornergletscher	7
2.2	Velocity seismograms of four types of icequakes	10
2.3	Hypocentral locations of icequakes at different depths	11
2.4	Distribution of compressive and dilatational arrivals around a 2004 surface cluster event	11
2.5	Waveform fits of explosions set off at depths of 0.5 m and 50 m	18
2.6	Grid for source-type plot	20
2.7	Source-type plot for shallow and deep explosions	21
2.8	Waveform fits obtained with the full moment tensor inversion of an icequake associated with a crevasse opening	22
2.9	Source-type plots for three types of icequakes	23
2.10	Waveform fits obtained with the deviatoric moment tensor inversion of a shear-type icequake	25
2.11	Waveform fits of an intermediate-depth icequake	27
2.12	Photograph of englacial fracture	31
3.1	Possible fracture processes in glacier ice	37
3.2	Overview of Gornergletscher	39
3.3	Ground displacement seismograms of a basal event recorded in 2004	41
3.4	Ground displacement seismograms of a basal event recorded in 2006	42
3.5	Sensitivity tests of full moment tensor inversion	47
3.6	Sensitivity tests of crack moment tensor inversion	50
3.7	Waveform fits of the full moment tensor inversion of a basal icequake using TILL3D Green's Functions	51
3.8	Waveform fits of the full moment tensor inversion of a basal icequake using GRANITE3D Green's Functions	52
3.9	Source type plots of full moment tensor inversions using different Green's Functions.	54

3.10	Waveform fits of the tensile crack moment tensor inversion with TILL3D Green's Functions	56
4.1	Overview of Gornergletscher	63
4.2	Ortho-photographs of the areas of the seismic networks in 2004 and 2006	66
4.3	Epicenters and hypocenters of deep icequake clusters detected in 2004 and 2006	67
4.4	Vertical velocity seismograms of 2004 basal icequakes	71
4.5	Seismic activity on Gornergletscher measured by the 2004 seismic array	72
4.6	Stacked times of icequake occurrences	76
4.7	Comparison between basal icequakes and subglacial water pressures	78
4.8	Comparison between surface uplift, basal water pressure and the source times of basal icequakes	80
5.1	2007 seismic array and event epicenters	87
5.2	Activity of a basal cluster near J7 recorded in 2007	88
5.3	Seismograms of two events belonging to a 2007 basal cluster beneath J8	89
5.4	Seismic record of calving event on July 1, 2007	91
5.5	Cross-correlation of two one-hour segments of continuous data	92
5.6	2D illustration of ambient noise cross-correlation	93
5.7	Example of beam-forming location	94
D.1	Map of 2004 seismic network	111
D.2	Map of 2005 seismic network	112
D.3	Map of 2006 seismic network	113
D.4	Map of 2007 seismic network	114
E.1	2004 seismic setup	116
E.2	2005 seismic setup	117
E.3	2006 seismic setup	118
E.4	2007 seismic setup	119
E.5	Photographs of instrumentation	120

List of Tables

2.1	Variance reductions of moment tensor inversion fits	20
2.2	Source parameters calculated from moment tensors given by the crack+DC inversion	30
3.1	Specifications of seismic velocity models	45
3.2	Variance reductions of full moment tensor inversions using different 3D Green's Functions	53
3.3	Variance reductions of full and tensile crack moment tensor inversions using different 3D Green's Functions	55
4.1	Seismic recording specifications of the 2004 and 2006 networks	65
B.1	Summary of moment tensor solutions for inversions presented in Chapter 2	103
D.1	Operational period of seismometer networks	106
D.2	Approximate data volume.	109
D.3	Recording and trigger specifications	110
E.1	Seismometer specifications for 2004 and 2005 networks	122
E.2	Seismometer specifications for 2006 and 2007 networks	123

Abstract

In the present work I investigate the seismic activity of Gornergletscher, Switzerland's second largest glacier, during the annual drainages of Gornensee, a nearby ice-marginal lake. During the summers 2004, 2005, 2006 and 2007, about 200,000 'icequakes' were recorded on Gornergletscher. Most events are consequences of crevasse opening near the surface. Moment tensor inversions of such events are consistent with a tensile dislocation, which is a highly isotropic seismic source. I also found about one dozen of near-surface icequakes whose moment tensors are double-couples. This is solid evidence for shear fracturing within alpine glacier ice. Icequakes near the glacier bed or at intermediate depths were identified, although they make up only a small fraction of the recorded events. I perform moment tensor inversions for one intermediate and one basal icequake cluster and find that the source mechanisms are tensile dislocations, like the typical near-surface icequake. However, the catalog of basal icequakes also contains events whose waveforms show significant differences to those that were used in the moment tensor inversion. This suggests that events with a variety of source mechanisms occur near the glacier bed.

During the warm day hours of the summer, large amounts of surface melting occurs on Gornergletscher. This meltwater accumulates at the glacier bed, where it can raise subglacial water pressures close to flotation level. Consequently, the water level inside boreholes can fluctuate by up to 100 m on a diurnal scale. The diurnal peak of near-surface seismic activity occurs during warm day times, as well. This is explained by increased surface deformation caused by melt-water enhanced basal sliding. On the other hand, basal seismic sources are active during night times, when basal water pressures are low or decreasing. This type of seismicity is therefore not likely a consequence of melt-water enhanced basal sliding or hydrofracturing. Instead I suggest that basal seismicity is caused by large deformation rates of the basal ice layer, which occur when the glacier couples to the bed after a period of melt-water enhanced sliding. These findings are consistent with seismic observations concurrent with the drainage of Gornensee. During the drainage event, large amounts of lake water are routed to the subglacial drainage system, thus maintaining the subglacial water pressure at a high level even during night. The resulting increase in ice deformation causes a surge in near-surface seismicity. On the other hand, the activity of basal icequakes near the lake decreases with the onset of the lake drainage.

Zusammenfassung

In dieser Arbeit untersuche ich die seismische Aktivität auf dem Gornergletscher, dem zweitgrössten Gletscher in der Schweiz, während der jährlichen Entleerung des gletschergestauten Gornersees. Während der Sommer 2004, 2005, 2006 und 2007 wurden ca. 200,000 'Eisbeben' auf dem Gornergletscher aufgezeichnet. Die meisten Beben resultieren aus Spaltenöffnungen nahe der Gletscheroberfläche. Momententensorinversionen solcher Ereignisse deuten auf Spannungsbrüche hin, was eine seismische Quelle mit besonders hohem isotropen Anteil darstellt. Ausserdem fand ich etwa ein Dutzend Oberflächenereignisse mit 'double-couple' Momententensoren. Dies ist ein deutlicher Hinweis auf Scherbrüche in alpinem Gletschereis. Eisbeben nahe des Gletscherbettes oder auf mittleren Tiefen stellen nur einen geringen Anteil der aufgezeichneten Ereignisse dar. Ich berechne Momententensoren für einen Eisbebencluster auf mittlerer Tiefe und einen Eisbebencluster nahe des Gletscherbettes. Die berechneten Quellmechanismen sind Spannungsbrüche wie die typischen seismischen Quellen nahe der Oberfläche. Der Katalog basaler Eisbeben enthält jedoch auch Ereignisse, deren Wellenformen sich stark von denen, die in der Momententensorinversion verwendet wurden, unterscheiden. Dies deutet darauf hin, dass verschiedene Quellmechanismen am Gletscherbett auftreten.

Während des Sommers tritt auf der Oberfläche des Gornergletschers zu warmen Tageszeiten eine starke Schmelze ein. Dieses Schmelzwasser sammelt sich am Gletscherbett an, wodurch der subglaziale Wasserdruck fast bis an das Schwimmgleichgewicht ansteigen kann. Dadurch können die Bohrlochwasserspiegel täglich um bis zu 100 m schwanken. Die täglichen Maxima der seismischen Aktivität nahe an der Gletscheroberfläche treten ebenfalls zu warmen Tageszeiten auf. Als Grund dafür kommen vor allem erhöhte Verformungsraten an der Gletscheroberfläche in Frage, weil der hohe subglaziale Wasserdruck die basale Gleitgeschwindigkeit verstärkt. Basale Eisbebenquellen sind jedoch aktiver während der Nacht, wenn der subglaziale Wasserdruck niedrig oder am Fallen ist. Diese Art von Seismizität wird deswegen wahrscheinlich nicht durch verstärktes basales Gleiten oder 'hydrofracturing' hervorgerufen. Stattdessen interpretiere ich diese Beben als Bruchvorgänge während starker Verformungen am Gletscherbett. Starke basale Eisdeformationen werden vor allem dann erwartet, wenn der Gletscher nach einer Phase mit grossen Gleitgeschwindigkeiten wieder an das Gletscherbett gekoppelt wird. Diese Ergebnisse decken sich mit seismischen Beobachtungen während der Entleerung des Gornersees. Dann werden grosse Mengen Seewasser dem subglazialen Abflusssystem zugeführt, wodurch der subglaziale Wasserdruck auch während der Nacht auf einem hohen Niveau bleibt. Die resultierende Eisverformung bewirkt einen Anstieg der oberflächennahen Seismizität. Auf der anderen Seite wird eine Abnahme von basalen Eisbeben verzeichnet.

Chapter 1

Introduction

1.1 Context

The Icelandic term 'jökulhlaup' refers to the sudden drainage of water from a glacial body. During such a glacier outburst flood, glacier-dammed lakes release their water masses, which are then routed to the glacier snout via englacial or subglacial conduits. As a consequence, the discharge of the proglacial stream can increase by more than one order of magnitude, often within hours. To date, these drainage events are difficult to predict and thus pose a serious threat to human life and infrastructure near glaciated areas.

Theoretical descriptions of jökulhlaups are concerned with three particular glaciological processes: 1. The description of water flow through its solid phase. 2. The mechanism leading to the initiation of the lake drainage (the 'trigger'). 3. The interaction of the lake drainage with the glacier's flow dynamics. The first process has been scrutinized in several investigations (e. g. Nye, 1976; Spring and Hutter, 1982; Clarke 2003), which describe the evolution of englacial channels as a competition between melt-enlargement and creep-closure. With this model, 'slowly rising' jökulhlaups, which are characterized by exponentially rising discharge hydrographs, can be well explained. In these cases, the lake drainage is initiated (process 2), when a hydraulic connection between the lake and the subglacial drainage system is established. Concerning the third process, glacial lake drainages can significantly influence the glacial dynamics when the lake water input into the subglacial drainage system leads to water-enhanced sliding (Iken, 1981, Sugiyama et al., 2007).

To this juncture, theoretical treatments of these glaciological aspects of jökulhlaups do not include fracture processes which may be involved during the lake water release. At the same time, high subglacial water pressures during jökulhlaups possibly leading to 'hydrofracturing' as well as calving events prior to the drainage initiation (Sugiyama et al. 2008) suggest a pivotal role of fracture processes for jökulhlaup dynamics. Specifically, during 'rapidly rising' jökulhlaups, calving events during ice-dam flotation may trigger the lake drainage, and hydro-fracturing can contribute substantially to englacial water channel formation. Furthermore, basal motion, which is strongly dependent on subglacial water pressure, may lead to fracturing of basal ice layers, especially during drastic perturbations like the sudden lake water input into the subglacial drainage system.

Beginning with the work of Neave and Savage (1970), fracture processes in glacier ice have been shown to emit seismic energy. The seismic events that accompany crevasse formation or stick-slip motion are commonly known as 'icequakes'. In the present investigation I present a seismic approach to the study of glacier outburst floods. Gornersee, an ice-marginal lake at the confluence of Gornergletscher and Grenzgletscher in Switzerland's Canton Valais, was chosen as the study site. I monitored the glacier's icequake activity using high-density seismic networks during four Gornersee jökulhlaups. As this was part of a comprehensive field and modelling investigation, a wealth of data on glacier dynamics and hydrology was available for comparison with the findings from the seismic study.

1.2 Aim

The present thesis has two primary goals. First, a quantitative characterization of icequakes is given. I focus on seismic events associated with crevasse opening, the most common icequake type on Gornergletscher, as well as on seismic events, which occur near the glacier base. As a tool to describe the fracture modes, volumetric changes and fault plane orientations, I use the seismic moment tensor, which I calculate via full waveform inversions. The second goal is to link the basal icequake activity to subglacial processes, which are influenced by the Gornersee jökulhlaup. In the vicinity of Gornersee, an increase of the overall seismic activity can be noted as a reaction to the lake drainage (Aschwanden et al, 1992; Walter et al, 2008). The majority of these seismic events accompany the opening of surface fissures and crevasses and can be explained by the abrupt ice-dynamic changes induced by the jökulhlaup: First, the lake water input to the glacier bed enhances basal sliding and, second, the pressure boundary condition along the ice dam changes as the water level quickly drops (Riesen, 2007). Despite an increase of near-surface seismicity, I focus the present study on seismic events near the glacier bed, as this part of the glacier is particularly affected by high water pressures and fluctuations thereof.

1.3 Thesis Outline

This thesis is composed of three independent and self-contained parts. In the first part (Chapter 2) I perform full-waveform inversions to determine the seismic moment tensors of a variety of icequake sources. Using Green's Functions for a homogeneous half space I determine source mechanisms which are responsible for icequakes near the surface and at intermediate depths. The developed techniques are extended in the second part of this thesis (Chapter 3) to moment tensor inversions of basal icequakes, which require the generation of 3D Green's Functions. Chapter 4 is devoted to the third part, in which temporal fluctuations of basal icequake activity are analyzed. The findings are compared with other glaciological data and thus linked to the drainage of Gornersee.

Before concluding, I also present an outlook for further analysis of the seismic data recorded during the summers of 2004, 2005, 2006 and 2007. These data sets are suitable for a variety of additional studies on glacial seismicity which the present investigation does not cover. Finally, in the appendices, I give some technical details of the seismic instrumentation, software tools and the various moment tensor inversion schemes.

Chapter 2

Moment Tensor Inversions of Icequakes on Gornergletscher, Switzerland

FABIAN WALTER¹, JOHN F. CLINTON², NICHOLAS DEICHMANN²,
DOUGLAS S. DREGER³, SARAH E. MINSON⁴, MARTIN FUNK¹

¹Versuchsanstalt für Wasserbau, Hydrologie und Glaziologie (VAW), ETH Zürich, 8092 Zürich, Switzerland

²Institut für Geophysik, ETH Hönggerberg, CH-8092 Zürich, Switzerland

³Berkeley Seismological Laboratory, Berkeley, California-94720, U.S.A.

⁴Department of Geological and Planetary Sciences,
California Institute of Technology, Pasadena, California, U. S. A.

Published, Bulletin of the Seismological Society of America

Citation: Walter, F., J. F. Clinton, N. Deichmann, D. S. Dreger, S. E. Minson and M. Funk (2009). Moment Tensor Inversions of Icequakes on Gornergletscher, Switzerland. *Bulletin of the Seismological Society of America*, 99-2A, doi:10.1785/0120080110.

ABSTRACT: We have determined seismic source mechanisms for shallow and intermediate-depth icequake clusters recorded on the glacier Gornergletscher, Switzerland, during the summers 2004 and 2006. The selected seismic events are part of a large data set of over 80,000 seismic events acquired with a dense seismic network deployed in order to study the yearly rapid drainage of lake Gornersee, a nearby ice-marginal lake. Using simple frequency and distance scaling and Green's Functions for a homogeneous half space, we calculated moment tensor solutions for icequakes with $M_w \approx -1.5$ using a full-waveform inversion method usually applied to moderate seismic events ($M_w > 4$) recorded at local to regional distances ($\approx 50 - 700$ km). Inversions from typical shallow events are shown to represent tensile crack openings. This explains well the dominating Rayleigh waves and compressive first motions observed at all recording seismograms. As these characteristics can be observed in most icequake signals, we believe that the vast majority of icequakes recorded in the two years is due to tensile faulting, most likely caused by surface crevasse openings. We also identified a shallow cluster with somewhat atypical waveforms in that they show less dominant Rayleigh waves and quadrantal radiation patterns of first motions. Their moment tensors are dominated by a large double-couple component which is strong evidence for shear faulting. Although less than a dozen such icequakes have been identified this is a substantial result as it shows that shear faulting in glacier ice is generally possible even in the absence of extreme flow changes such as during glacier surges. A third source of icequakes was located at 100 m depth. These sources can be represented by tensile crack-openings. Due to the high hydrostatic pressure within the ice at these depths, these event are most likely related to the presence of water lenses that reduces the effective stress to allow for tensile faulting.

2.1 Introduction

Despite recent progress in numerical modelling in glaciology, the effect of brittle deformation on glacier dynamics has received relatively little attention. Yet surface crevassing, glacier calving, breaking-off of hanging glaciers and basal stick-slip motion indicate that fracture processes play a substantial role in glacier motion. Seismic techniques can be of pivotal importance in the studies of these phenomena as the elastic waves emitted by fracturing can be measured at distance from the source. The sites of interest range from small alpine glaciers to the Antarctic and Greenland ice sheets including their largest outlet glaciers. In every case, accurate timing, locations and waveforms of glacier-related seismic events allow for valuable insights into the physical processes that govern glacier flow.

Glacial earthquakes are seismic signals associated with large glaciers in Alaska, Antarctica and Greenland (Ekström et al., 2003). Although they are strong enough to be detected on global seismic networks they have only recently been identified. Their seismograms lack the high frequency initial arrivals traditional event detection techniques are based upon. The long-period surface waves generated by these glacial events can, on the other hand, be modelled by single forces representing a slip motion in a direction consistent with the flow of glaciers near or at epicentral locations. Recently, Joughin et al. (2008) published sound evidence that glacial earthquakes are related to major calving events.

The actual mechanism that produces the single forces needed to model the surface waves has not been identified. Glacier slip motion in response to the force imbalance following a calving event or rotational motion of a calving iceberg are two possible candidates (Tsai et al., 2008). Detailed analyses of temporal variations of glacial earthquakes in Greenland furthermore suggest a relationship with surface melt, ice dynamics and changing global climate (Ekström et al., 2006 and Tsai and Ekström, 2007). Wiens et al. (2008) have recently reported stick-slip motion of the Whillans Ice Stream in West Antarctica recorded with simultaneous GPS and seismic instruments. The latter were located up to 1000 km away from the West Antarctic Ice Sheet. Unlike the 'Ekström events', at least some parts of the seismic waveforms could be modelled with a double-couple source. This raises the question if a new type of glacial earthquake has been discovered and if there are systematic differences between the seismic activity emitted by the Greenland and Antarctic Ice Sheets.

A much weaker type of seismic activity associated with glacier slip motion originates at the base of Antarctic ice streams and has been investigated for several decades. These events can only be studied locally, because they are too weak to be detected by global or even regional seismic networks. From the frequency content of the seismograms it can be deduced that the slip during these events does not significantly contribute to the motion of the ice stream (Anandakrishnan and Bentley, 1993 and Danesi et al., 2007). Smith (2006) showed that spatial variations in basal seismic activity can be linked to variations in subglacial conditions such as deforming and lodged underlying sediments. Seismic signal characteristics and spatial and temporal variations in seismic activity also played an important role in studies that aimed at explaining the recent stagnation of Ice Stream C at the Siple Coast of the West Antarctic Ice Sheet (Anandakrishnan and Bentley, 1993; Anandakrishnan and Alley, 1994; Anandakrishnan and Alley, 1997a and 1997b).

Recently, O'Neel et al. (2007) and O'Neel and Pfeffer (2007) studied seismic signals radiated from calving events at Columbia Glacier, AK. The frequency content of these 'icequakes' allows for detection and thus monitoring of the calving activity via seismic measurements. Furthermore, frequency contents of the recorded signals led the authors to argue for a fluid-filled crack source model as the mechanism weakening the ice and eventually leading to calving.

Icequakes in alpine glaciers have been investigated in a variety of contexts. Several types of source mechanisms have been postulated or assumed such as surface crevasse formation (e. g. Neave and Savage, 1970; Deichmann et al., 2000), stick-slip motion (Roux et al., 2008; Weaver and Malone, 1979), resonant water-filled cavities (Métaxian et al., 2003) or bottom crevasse formation due to increased basal drag during low subglacial water pressures (Walter et al., 2008). Whereas these conclusions were drawn on the basis of hypocentral locations, temporal variations in activity or frequency content of the seismograms, we are unaware of any publication on full waveform inversions for the source parameters for these classes of events. Information about source-types, source geometry and volumetric changes open new possibilities to study glacier dynamics and hydrology via seismic techniques. A specific question to be answered is what kind of fracture modes are possible in ice. Are all icequakes a result of tensile fracturing or can they also be due to shear faulting? Furthermore, the source mechanisms of icequakes at greater depths may also shed some light on the influence that water has on fracturing (hydrofracturing). Presence of pressurized water can generally reduce the effective stress and thus drive tensile cracks into basal ice layers (Van der Veen, 1998b). Similarly, englacial water flow

may open up or enlarge cavities within the ice.

In this manuscript we present a method for moment tensor inversions using full waveforms of icequakes that were recorded on Gornergletscher, Switzerland, during the summers of 2004 and 2006. The data used for the present analysis were acquired as part of an investigation of the yearly subglacial drainages of Gornersee, a nearby ice-marginal lake (e.g. Huss et al., 2007; Sugiyama et al., 2007; Walter et al., 2008). The moment tensor is a concise representation of the seismic source in terms of force couple equivalents and its determination is a standard practice in earthquake seismology (e. g. Jost and Hermann, 1989; Aki and Richards, 2002). Whereas tectonic earthquakes are expected to have pure double-couple sources, typical icequakes can be expected to be related to tensile failure. Their sources can thus be expected to have significant isotropic and compensated linear vector dipole (CLVD) components (see Appendix A). Thus deviatoric moment tensors inversion routines used to describe typical earthquakes are not adequate for icequake sources. Using the general method developed by Dreger (2003) we follow Minson and Dreger (2008) to calculate full moment tensors as well as investigate the applicability of constrained moment tensors that constitute physical models of specific sources such as tensile crack openings and shear faults. We will focus the analysis on seismic events that originate from near the glacier surface as well as from intermediate depths, a considerable distance from the surface crevassing zone and from the glacier bed.

2.2 Field Investigations and Instrumentation

2.2.1 Study of Gornersee Outburst Floods

Ice-dammed masses of water exist essentially in any type of glacial environment. Their sudden drainage can increase the discharge of the proglacial streams in a catastrophic way (see Roberts, 2005, for a review). This phenomenon is also known by the Icelandic term 'jökulhlaup'. The physics behind such drainage events has been studied theoretically (Nye, 1976; Spring and Hutter, 1981; Spring and Hutter, 1982; Clarke, 2003). Yet jökulhlaups remain a considerable threat to human life and infrastructure, because they tend to occur irregularly and remain hard to predict.

The lake Gornersee is a marginal glacier-dammed lake that forms at the confluence of the main tributaries of Gornergletscher in the Valais region of Switzerland (Figure 2.1). It forms every spring with the advent of the melt season and drains in the following summer, often within days (Wilhelm, 1967; Bezinge et al., 1973; Aschwanden and Leibundgut, 1982; Huss et al., 2007). At its highest water level, the basin of Gornersee can contain up to $4 \times 10^6 \text{ m}^3$ and maximum discharges during the drainage event can be as high as $25 \text{ m}^3/\text{s}$. The discharge of Gornergletscher's proglacial stream can increase suddenly in response to the lake drainage. In the past this has caused damages to the downstream town of Zermatt (Raymond et al., 2003).

Gornersee is particularly suitable for a jökulhlaup study: there exists a wealth of available data on the glacier and lake, it is easily accessible and the drainage events occur on a regular, yearly basis. The ETH Zurich has conducted detailed observational and theoretical investigations during four drainage events. The focus is directed towards understanding the triggering mechanism of the lake drainage. To this end changes of glacier dynamics,

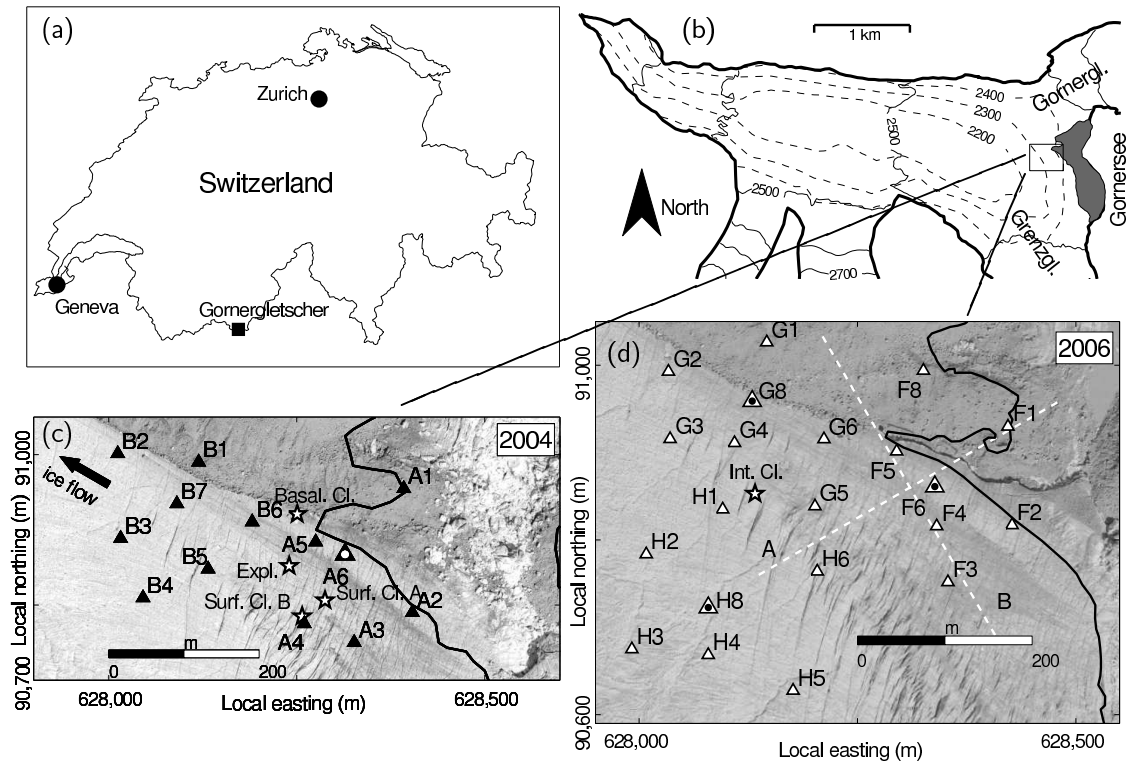


Figure 2.1: Location of Gornergletscher (a) and map of tongue of Gornergletscher (b). The latter also shows Gornersee, the locations of the seismic networks (box near the lake) and contour lines (in meters above sea level) that approximate the glacier's surface (solid) and bed (dashed). Ortho-photographs with seismic networks from 2004 and 2006 are shown in c and d, respectively. Seismometers are indicated by triangles and epicenters of event clusters studied in this work by stars (surface cluster A, surface cluster B as well as basal and intermediate clusters and explosions). Triangles with dots indicate sites where a surface and a deep borehole seismometer were installed. The solid line represents the outlines of Gornersee at the maximum water level reached in the corresponding year. Coordinates are given in the Swiss Grid. Upper portions of both ortho-photographs are darker reflecting moraine debris on the glacier surface. In panel d the cross-sections shown in Figure 2.3 are indicated by the white dashed lines.

hydraulics and seismicity in advance of and response to the drainage are monitored. In particular, the seismic investigation is aimed at clarifying the role of brittle deformation of ice within the glacier and near its bed as the englacial water pressure rises drastically during the drainage event.

For a detailed description of the instrumentation and seismic data as well as detection and location algorithms, the reader is referred to Walter et al. (2008). The present work focuses on data obtained with seismic arrays in 2004 and 2006, both situated near the ice dam (Figure 2.1), where the lake drainage has a severe impact on the ice dynamics (Sugiyama et al., 2007). In 2004, the operational period was between June 14 and July 8, in 2006 it was between May 28 and July 23. These time windows were selected to collect data in advance of and during the lake drainage. In addition to the surface seismometers, each array contained one or more seismometers at depths between 50 m and 250 m to better constrain hypocenter locations. The high pass corner frequencies of the sensors were between 1 Hz and 28 Hz and the instruments were operated at high sampling frequencies (1000 Hz - 4000 Hz) in trigger mode.

2.3 Icequake Waveform Discrimination and Locations

Over 35,000 and 50,000 icequakes were recorded during the field seasons of 2004 and 2006, respectively. In agreement with seismicity observed in previous studies on alpine glaciers (Deichmann et al., 2000; Neave and Savage, 1970), we associate the vast majority (over 99 %) of these signals with crevasses opening near the surface. For an alpine glacier, surface crevassing is confined to the top 20 m of the glacier ice (Paterson, 1994). Water-filled fractures which can potentially penetrate the glacier to larger depths have not been observed at the study site. As the main goal of the seismic investigation on Gornergletscher was to investigate brittle fracture of glacier ice due to englacial and subglacial water flow, events that occur well below this depth are of particular interest. An automated waveform discriminator and cross-correlation search were used to efficiently identify about 1,000 events each year whose waveforms are substantially different from those of the typical surface crevasse events (Walter et al., 2008). Arrival times of these events were picked by hand. The hypocenters were determined via an inversion algorithm identifying a location in space that minimizes the differences between calculated and hand-picked arrival times (Lee and Steward, 1981). Overall, only a very small portion of icequakes (without reliable statistics, we estimate significantly less than 1% of the complete data set) has been located at depths well below the reach of surface crevasses.

In the remainder of this paper we discuss specific groups of icequakes recorded on Gornergletscher. We present source mechanisms of typical examples of shallow as well as deep icequakes. In addition, we analyzed a group of shallow icequakes with double-couple sources and fundamentally different signal characteristics from a typical shallow event associated with crevasse opening. Even though interesting, we have found only very few such exceptional icequakes and their number may be statistically insignificant in comparison to the large number of crevasse opening events. Yet their occurrence raises some fundamental questions concerning the nature of brittle deformation of ice.

2.3.1 Characteristics of near-surface events

Icequakes from a number of surface crevasse fields were recorded in both summers. The seismic arrays had an aperture of ≈ 200 m and were placed near a rather active surface crevassing zone (Figure 2.1) and thus a large number of near-surface events were recorded with a good azimuthal coverage.

The waveform of a typical near-surface event is shown in Figure 2.2a. This event is part of a cluster of 5 events (henceforth 'surface cluster A'), which occurred between June 21 and June 22, 2004 near station A4 (epicentral location shown in Figure 2.1). The relatively short period of activity (24 hours) of this cluster likely reflects a crevasse opening leading to stress relaxation. All events occurred within meters of the glacier surface (Figure 2.3). As is typical for most icequakes, the signals of this cluster are characterized by compressive first motion at all azimuths. This is evidence for a significant isotropic moment tensor component. A further typical characteristic is the dominant Rayleigh wave at more distant stations such as B3, for which the waveform is shown in Figure 2.2a.

Figure 2.2b shows a waveform of a surface event that belongs to another cluster inside the crevassing zone (henceforth 'surface cluster B'). This cluster also consists of 5 events and it was active for only a few hours on July 5, 2004 (see Figure 2.1 for epicentral location). The waveforms show substantial differences to those of surface cluster A. For equal source-receiver distances and azimuths, the Rayleigh wave of the surface cluster B events is less developed than that of the surface cluster A events. Specifically, at station B3 the S-wave is stronger than the Rayleigh wave, whereas for the surface cluster A events it is the other way around (compare panels a and b of Figure 2.2). These differences are most likely caused by source effects rather than path effects, because the epicenters of both surface clusters lie within 40 m of each other and their depths are also comparable (Figure 2.3). The first arrivals of surface cluster B events suggest a quadrantal distribution of compressive and dilatational motion (Figure 2.4), which is typical for double-couple sources. This characteristic has only been noted in about a dozen icequakes. The usual case is compressive first motion at all azimuths like the events of surface cluster A.

2.3.2 Characteristics of Deep Icequakes

About 80 and 200 icequakes were located at depths well below the surface crevassing zone in 2004 and 2006, respectively. In 2004, all of these events were located near the glacier bed, whereas in 2006 about 20 were located at intermediate depths. Most basal icequakes cluster in distinct regions. A waveform from an event belonging to a basal cluster is given in Figure 2.2d. This cluster lies at a depth of 160 m, in the immediate vicinity of the glacier bed (epicentral location shown in Figure 2.1) and consists of 29 events that occurred over a period of more than two weeks. The waveform shown has a higher frequency content compared to the signals of near-surface events. The lower frequency content of the latter is explained by the high density of vertical crevasses in the shallow ice layers, which tend to filter out high frequencies for waves from shallow events which must cross the crevasses. Typical features of deep icequakes are the impulsive P wave and the lack of a notable Rayleigh wave.

Three events located at 100 m depth constitute another event type investigated in this study (Figure 2.2c). They form a cluster (henceforth 'intermediate cluster') which was active

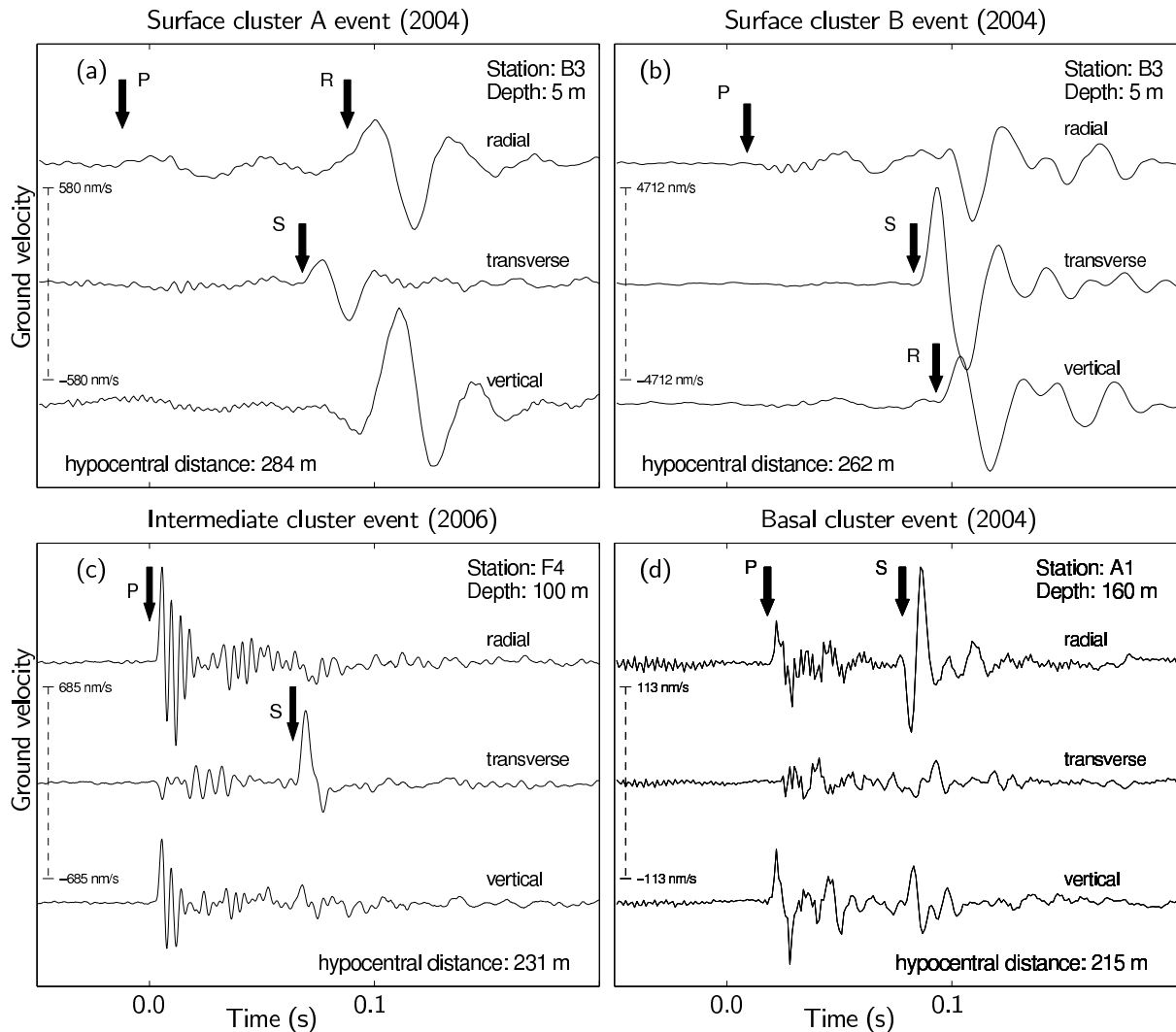


Figure 2.2: Velocity seismograms of four types of icequakes recorded by surface seismometers. The seismograms of the two shallow events (panels a and b) were recorded at the same station (B3). Since the sources occurred close to each other, the different relative strengths of the S- and Rayleigh phases are likely due to source effects rather than path effects. The seismograms of the intermediate and basal events (panels c and d) show higher frequencies and are dominated by impulsive P- and S-waves. They do not have a notable Rayleigh phase. The P-waves of the shallow events, on the other hand, are hardly visible. Theoretical P, S, and Rayleigh-arrival times are indicated by arrows.

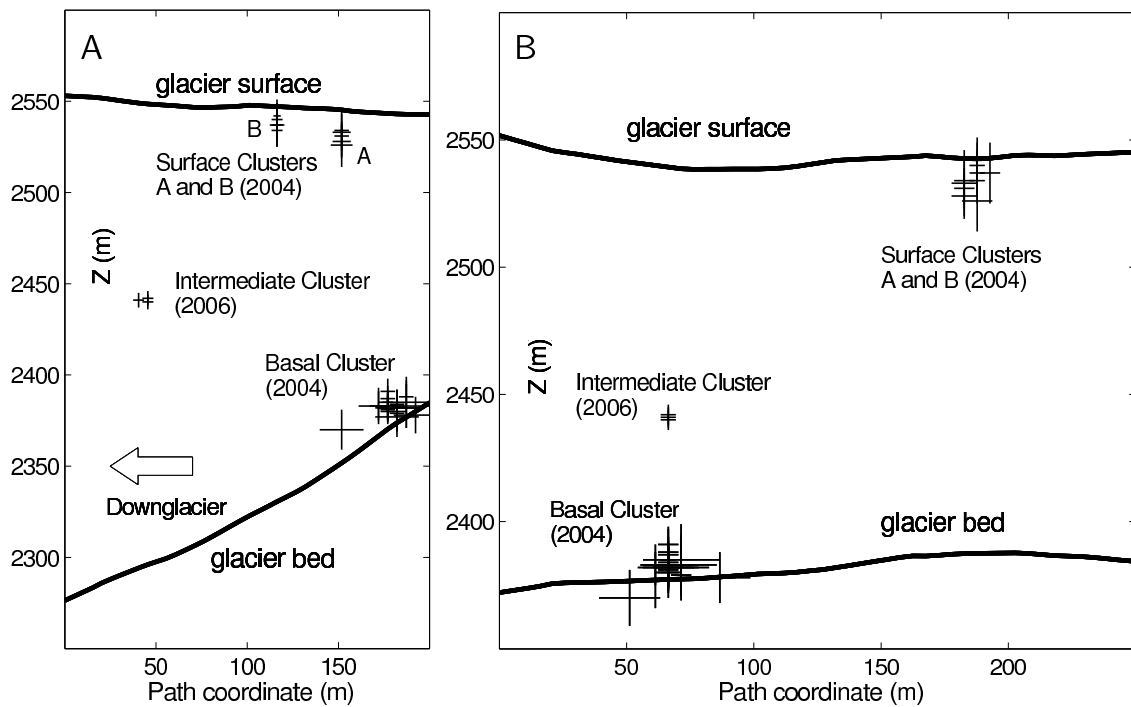


Figure 2.3: Hypocentral locations of the icequakes presented in this paper. The plots are taken along two cross-sections (Figure 2.1d). A (left) is along the steepest gradient of the glacier bed, corresponding roughly to the direction of glacier flow, and B (right) is perpendicular to this steepest topography (see Figure 2.1 for bed topography). The sizes of hypocentral markings indicate location uncertainties in horizontal and vertical directions.

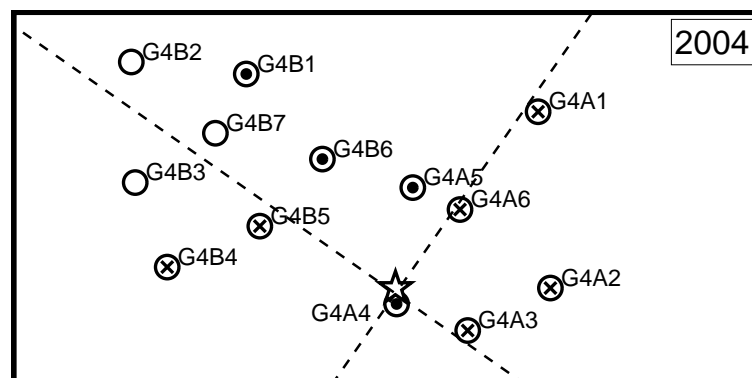


Figure 2.4: Distribution of compressive and dilatational arrivals around a surface cluster B event recorded on the 2004 seismic network (Figure 2.1). The event epicenter is indicated by the star. Dots and crosses mark seismometers with upward compressive and downward dilatational first motions, respectively. Empty circles are stations at which the first arrivals were not impulsive enough to determine their polarity. The observed polarities suggest a quadrantal radiation pattern consistent with a double-couple source. The dashed lines separate the quadrants.

for a few hours on June 16, 2006 (see Figure 2.1 for epicentral location). At this depth, they are occurring significantly below the surface crevassing zone, and they cannot be associated with fracture near the glacier bed. For modelling purposes, reflection effects from the surface and the glacier bed can thus be neglected at this depth. Like the basal events, the signals of the intermediate events contain more energy at high frequencies than surface events, and also show impulsive P waves. S-phases of the intermediate icequakes are strongest on the transverse components whereas for basal cluster events the S-energy is dominant on the radial component. This does not seem to be an effect of different source-receiver azimuths and is thus due to different source mechanisms or reflections off the glacier bed in the case of the basal events.

In the present study we focus on source modeling of near-surface and intermediate events. Whereas we present some basal events for the sake of completeness, we do not show any waveform modelling results of their signals. For sources near the glacier base, the 2D or even 3D topography of the glacier bed produces complicated reflections that cannot be accurately modelled using a 1D velocity profile. Synthetic seismograms show that these sources are close enough to the ice-bedrock interface that the reflections interfere with the direct waves. Thus, the amplitudes of the first arrivals are substantially altered. If Green's Functions are calculated for an incorrect velocity model, these changes in amplitude may be mapped into source properties rather than path properties. For the intermediate and near-surface events this effect is less severe as the reflections are weaker and are part of the coda and not part of the direct waves.

Furthermore, the waves of intermediate events traverse only few surface crevasses on their way to the surface seismometers, compared to the waves of near-surface events. For these reasons source modelling of intermediate events is found to be particularly straight forward.

2.4 Moment Tensor Inversions

2.4.1 Motivation for Study of Various Source Types

A large variety of seismic sources such as explosions, shear faults, tensile crack openings, as well as combinations thereof can be represented by a linear combination of elastic responses to force couples. The relative strengths of the individual force couples are given by a 2nd rank symmetric moment tensor (e. g. Aki and Richards, 2002). Thus, moment tensors contain information about underlying seismic source mechanisms and pose a rigorous characterization of seismic sources.

The inversion of broadband waveform data from seismograms to produce moment tensor source mechanisms is common to study seismic sources (see Jost and Hermann, 1989 for a review). An unconstrained full moment tensor inversion may suffer from numerical instabilities (Dufumier and Rivera, 1997). This problem is usually tackled by imposing mathematical constraints in the inversion scheme. A common example is the inversion of tectonic earthquakes, where the isotropic component of the moment tensor is forced to vanish, as the sources are usually expected to be double-couple. In this case, a large compensated linear vector dipole (CLVD) component usually indicates errors with the Green's Functions.

A nonzero isotropic component indicates that the source region undergoes a volumetric change during the seismic event. In order to interpret the volumetric change calculated from the isotropic moment correctly, the source geometry must be taken into account (Müller, 2001).

An explosion possesses a purely isotropic moment tensor. A shear fault, associated with tectonic earthquakes, gives rise to a purely deviatoric double-couple moment tensor. The CLVD can also be completely described by a deviatoric moment tensor.

The CLVD source mechanism does not correspond to a specific observed physical process, but can be explained by more complicated mechanisms. Examples are shear faulting near discontinuities of elastic moduli, rapid polymorphic phase changes (Julian, et al., 1998) and tensile cracks accompanied by compensating implosions (Julian and Sipkin, 1985). The CLVD source has been used to describe volcanic events (e. g. Julian and Sipkin, 1985) and deep earthquakes (Knopoff and Randall, 1970).

An important example of a source represented by a combination of an isotropic and a deviatoric moment tensor is the tensile fracture, also referred to as the 'tensile crack' model. The deviatoric part is a pure CLVD and its strength relative to the isotropic component is dependent on the Poisson's ratio of the material constituting the source (see Appendix A). In the present work we assume a Poisson's ratio of 0.36 which was found to yield good waveform fits and lies in the ranges of Poisson's ratios for ice as given in Turcotte and Larson (2002). For comparison, Minson et al. (2007) assume a Poisson solid with a Poisson's ratio of 0.25 for the source region of volcanic events. With the Poisson's ratio used in the present icequake study, the isotropic component of the tensile crack moment tensor is almost five times larger than the CLVD.

A linear combination of the double-couple and the tensile crack moment tensors (henceforth 'crack+DC') constitutes a model that is highly relevant to the present work. Recently, Minson et al. (2007) applied the crack+DC model to seismic and geodetic data of the 2000 Miyakejima volcanic earthquake swarm. The authors argue that this model is particularly applicable to seismic events induced by magma propagation. In the case of glacial seismicity we expect tensile fracturing, which represents a special case of the crack+DC model, to be a likely failure model. Under normal flow conditions the opening direction of pervasive crevasses is parallel to that of maximum tension, even in regions of simple shear such as near the glacier margin (Paterson, 1994). Representing a tensile fracture, a tensile crack model thus provides a plausible mechanism for crevasses opening. On the other hand, Roberts et al. (2000) observed fracturing on the surface of Icelandic glaciers that developed during glacial lake drainages and showed some indication of shear failure. This suggests that during rapidly changing dynamic or hydrological conditions, glacier ice may undergo shear failure. The crack+DC moment tensor poses a plausible model for both, crevasses opening and shear faulting caused by abnormal ice flow, as well as any superposition of the two processes.

Deviatoric and crack+DC moment tensors are used in constrained moment tensor inversions. Besides yielding numerical stability, constrained moment tensor inversions are a means of testing the applicability of a certain source mechanism. For instance, in the present work we will repeatedly test the hypothesis of a tensile crack source solution for icequakes by comparing the fit quality of the crack+DC inversion to that of the full moment tensor inversion. If the latter results in much higher fit qualities, the tensile crack

moment tensor does not explain the observed seismograms, but if both equally well solve the problem, the simple, constrained mechanism is proposed.

2.4.2 Numerical Tools

In our approach, we use 1D Green's functions representing a homogeneous half space with P- and S-velocities of 3.63 km/s and 1.76 km/s, respectively. The corresponding seismic attenuation quality factors are 600 and 300, respectively. As discussed in the following section, this is a good approximation to the velocity model of the glacier. The Green's Functions were computed using the FKRPROG software developed by Chandan Saikia of URS (Saikia, 1994). The deviatoric and full moment tensor solutions were calculated by applying a corrected form (Minson and Dreger, 2008) of the linear time domain moment tensor inversion scheme used by Dreger et al. (2000) and Dreger and Woods (2002). Moment tensors of the crack+DC model were determined with a grid search algorithm developed and applied by Minson et al. (2007). Whereas the full inversion scheme has 6 degrees of freedom corresponding to the unique elements of the moment tensor, the deviatoric and crack+DC inversion schemes only have 5 degrees of freedom. As a measure of fit quality, the *variance reduction*, VR, given by

$$VR = \left(1.0 - \frac{\int (data - synthetic)^2 dt}{\int (data)^2 dt}\right) \times 100\% \quad (2.1)$$

was calculated for each fit. A perfect fit gives a *variance reduction* of 100%. Following Templeton and Dreger (2006), the variance reduction is also used to perform *F*-test statistics (Menke, 1989). This is necessary as the fit quality is expected to increase with the complexity of the model. Specifically, we evaluate if differences in variance reduction calculated with the different inversion schemes reflect physical source properties or if they are consequences of the different numbers of degrees of freedom included in the source model. The time offset used to align data and synthetics to maximize the variance reduction is called the *zcor* value. In all cases the *zcor* value is adjusted manually through trial and error to increase the variance reduction of the waveform fit. It should be mentioned that although the same Green's Functions and the same *zcor* values are used in the three different inversions for a given event, the variance reduction of the crack+DC grid search sometimes exceeds the variance reduction of the full moment tensor inversion. This is not expected as a full moment tensor contains more degrees of freedom than a crack+DC moment tensor (6 and 5, respectively). The crack+DC grid search can find fits with higher variance reductions because it maximizes the variance reduction itself. The full and deviatoric moment tensor inversions, on the other hand, determine a least square solution. Both techniques minimize a measure of misfit, but the respective maxima and minima do not necessarily coincide. Using *F*-test statistics we found that whenever the crack+DC inversion calculates a slightly higher variance reduction than the full moment tensor scheme, it is not statistically significant.

2.4.3 Moment Tensor Inversion for Icequakes

The moment tensor related numerical tools described in the previous section typically are used to model signals from moderate seismic events ($M_w > 4$) recorded at regional dis-

tances ($\approx 50 - 700$ km). Relevant periods of these signals are between 10 and 100 s. The Green's Functions are generated for 1D velocity models appropriate for these dimensions and frequencies. In order to apply these available software packages to our glacial environment, we scaled the dimensions of the seismic network and consequently of the whole glacier as well as the sampling rate of our data by a factor of 1000. Seismic velocities and material properties are not affected by this scaling, so the ratio of wavelengths to spatial dimensions is preserved. A reflectivity code (Müller, 1985; Ungerer, 1990) served as a means to verify the results given by this scaled inversion, because it allows for the generation of synthetic seismograms at glacier dimensions.

Using active seismic techniques, Deichmann et al. (2000) found no significant depth dependence of seismic velocities inside Unteraargletscher, Switzerland. Their study site, like the one of the present investigation, was located in the ablation area and no firn or snow was present. In order to determine the seismic velocity structure of the study site of the present work, active seismic measurements were also conducted on Gornergletscher (Gischig, 2007) producing a velocity tomography based on arrival time inversions and waveform modelling. The results show that below the crevassing zone, the seismic velocities do not vary significantly with depth. The seismic velocities of the top 20 m, however, can be significantly lower due to crevasses and fissures. Since the thickness of this slow layer is still smaller than the wavelengths at which the moment tensor inversions are performed, Green's functions are calculated for a half space with P- and S-velocities of 3.63 km/s and 1.76 km/s, respectively.

The influence of crevasses, fissures and other inhomogeneities near the glacier surface also manifests itself in scattering and reflecting of seismic waves. The resulting complexity in the waveforms was reduced by using an acausal two-pole, two-pass Butterworth bandpass filter. As crevassing causes scattering and attenuation mainly near the surface, the seismograms of near-surface events were filtered between 5 Hz and 30 Hz whereas those of intermediate events were filtered between 20 Hz and 60 Hz.

Moment Magnitude Scaling

Scalar moments were calculated in two different ways. In the case of the deviatoric moment tensor inversion the equation

$$M_0 = \frac{|m'_1| + |m'_3|}{2} \quad (2.2)$$

was employed, where M_0 is the scalar moment and m'_1 and m'_3 are the largest and the smallest deviatoric eigenvalues (in absolute value) of the moment tensor, respectively. For the moment tensors calculated via the full and the crack+DC moment tensor inversion schemes, the scalar moment was determined by

$$M_0 = \frac{\text{trace}(\mathbf{M})}{3} + m'_1, \quad (2.3)$$

where \mathbf{M} is the full moment tensor (Bowers and Hudson, 1999). Note that for a double-couple source both equations yield the same scalar moment.

The artificial scaling of the sampling frequency and the source-receiver distances affect the calculation of the scalar moment. To determine the scaling factor of the scalar moment

corresponding to a scaling of distance and frequency by a factor of 1000, consider the following analytical expression for the scalar moment of a double-couple source (e. g. Boatwright, 1980):

$$M_0 = \frac{4\pi \rho_x^{1/2} \rho_\xi^{1/2} \beta_x^{1/2} \beta_\xi^{5/2}}{F_{\theta\phi}^{SH} S^{SH}} R \int_0^T u^{SH}(\tau) d\tau \quad (2.4)$$

Here, ρ_x and ρ_ξ are the densities at the station and source, respectively. β_x and β_ξ are the respective S-velocities. $F_{\theta\phi}^{SH}$ is the radiation coefficient and S^{SH} is the free-surface amplification; R is the hypocentral distance and $u^{SH}(t)$ is the ground displacement due to the SH-wave. The integration is performed over the duration of the S-wave T. The calculation in Equation 2.4 can also be applied to P or SV-waves. However, in these cases the free-surface amplification is affected by mode conversions, whereas in the case of SH-waves it is simply a factor of two. Scaling the sampling interval increases the value of the integral by a factor of 1000. Another factor of 1000 enters the expression via scaling of the source-receiver distance R. Therefore, the scalar moment is overestimated by a factor of 10^6 . This was verified for each event with forward modelling of the waveforms using the reflectivity code. For a double-couple event, Equation 2.4 constitutes a second possibility for calculating the scalar moment using the unscaled signals. Although the result of the moment tensor inversion overestimates the scalar moment by 10^6 , the fault plane geometry and the corresponding radiation coefficient $F_{\theta\phi}^{SH}$ are unchanged as geometry is unaffected by the scaling. This can then be used together with SH displacement of the unscaled seismograms integrated in the time domain to obtain the scalar moment.

Once the corrected scalar moment has been determined using Equations 2.2, 2.3 or 2.4, we calculate the moment magnitude, M_w , via (Hanks and Kanamori, 1979)

$$M_w = (2/3) \log M_0 - 6. \quad (2.5)$$

Note that in this equation M_0 is given in units of N m.

Station Selection

As the instruments were placed directly on the glacier ice, surface melt required daily aligning and leveling of the seismometers. Even this did not guarantee correct alignment at all times. Therefore, the seismograms were scrutinized for quality before the inversion schemes were applied. One means to check for correct alignment was to ensure that the P-wave is primarily present on the radial component. Since a misalignment was usually a combination of rotation and tilt, it was not possible to 'reorient' the sensor via a coordinate axes rotation about the vertical axis at the data processing stage. Furthermore, 2D or 3D scattering effects, that the 1D Green's Function cannot account for, could result in P-energy on the transverse component. Therefore, the presence of significant P-signal on the transverse component was a criterion to exclude the seismogram from the inversion.

The $zcor$ value determined in the inversion schemes is a further selection criterion. Clinton et al. (2006) have shown that the $zcor$ value increases linearly with epicentral distance. Deviations of the $zcor$ value from this linear relationship thus provide a good selection criterion for the set of stations to be used in a moment tensor inversion.

As a last check, the fit quality of each station was evaluated. If the fit of a seismogram was of extremely low quality compared to the other stations in the same inversion, it was removed. However, this was rarely the case. A possible bias may be introduced by differences in azimuthal coverage resulting from different sets of seismograms used in the inversions. This was important for the case of the intermediate cluster where the number of suitable stations was between 10 and 14. Therefore, only the set of suitable stations common to all events was used in the individual inversions.

2.5 Discussion of Inversion Results

2.5.1 Inversion of Explosion Signals

In order to investigate the performance of the moment tensor inversion using a human source, we first present the results of the full inversion scheme applied to two explosive charges set off at depths of 0.5 m and 50 m in the summer of 2004. The former was placed into a small borehole, 0.5 m deep and about 5 cm in diameter. Subsequently, the borehole was filled with ice to the glacier surface. For the 50 m deep explosion, the charge was suspended in a water-filled borehole that had a diameter of about 30 cm. The epicentral locations of both explosions are close to station G4A5 as shown in Figure 2.1. Figure 2.5 shows the resulting waveform fits for the unconstrained inversion. The signals of the 0.5 m and 50 m deep explosions were band-pass filtered like the icequakes at shallow and intermediate depths, respectively. The overall variance reduction of the inversion of the shallow shot (Figure 2.5, upper) is 80 %. At most stations the frequencies and amplitudes of the dominant phases are modeled well. The focal mechanism shows compressive first motions at all azimuths, which is expected for an isotropic source. This is also in agreement with the observed P-polarities. There is some signal on the tangential component that is not expected for a perfectly isotropic source. Some of it may be due to shear energy released in response to the explosion. However, since at some stations, such as G4B2, this wave phase is not modelled, it may be due to source effects that cannot be described by a first order moment tensor or to complicated path effects.

The signals of the deep shot (Figure 2.5, lower) contain higher frequencies than the shallow shot as discussed in Section 2.3.2. Although the dominant phases are again matched well there is significant signal-generated noise on all components that cannot be reproduced by the synthetics. This causes a lower overall variance reduction of 57 %. The signal-generated noise may be due to waves traveling along the walls of the borehole. Furthermore, the presence of a strong phase on the tangential component of some stations, such as G4B4, hints towards the release of shear energy during the explosion, similar to the shallow explosion. The plot of focal mechanism again indicates a dominant isotropic moment tensor component.

It should be stressed that despite an approximately equal amount of explosive charge the moment magnitude of the shallow explosion is more than a magnitude larger than the deep explosion. Comparison with two other near-surface shots and two shots made at 100 m and 150 m gave similar magnitude discrepancies. The magnitude difference therefore does not change with depth, but exists between shallow shots and deep borehole shots in general. We suggest two explanations for this observation: The first one we refer

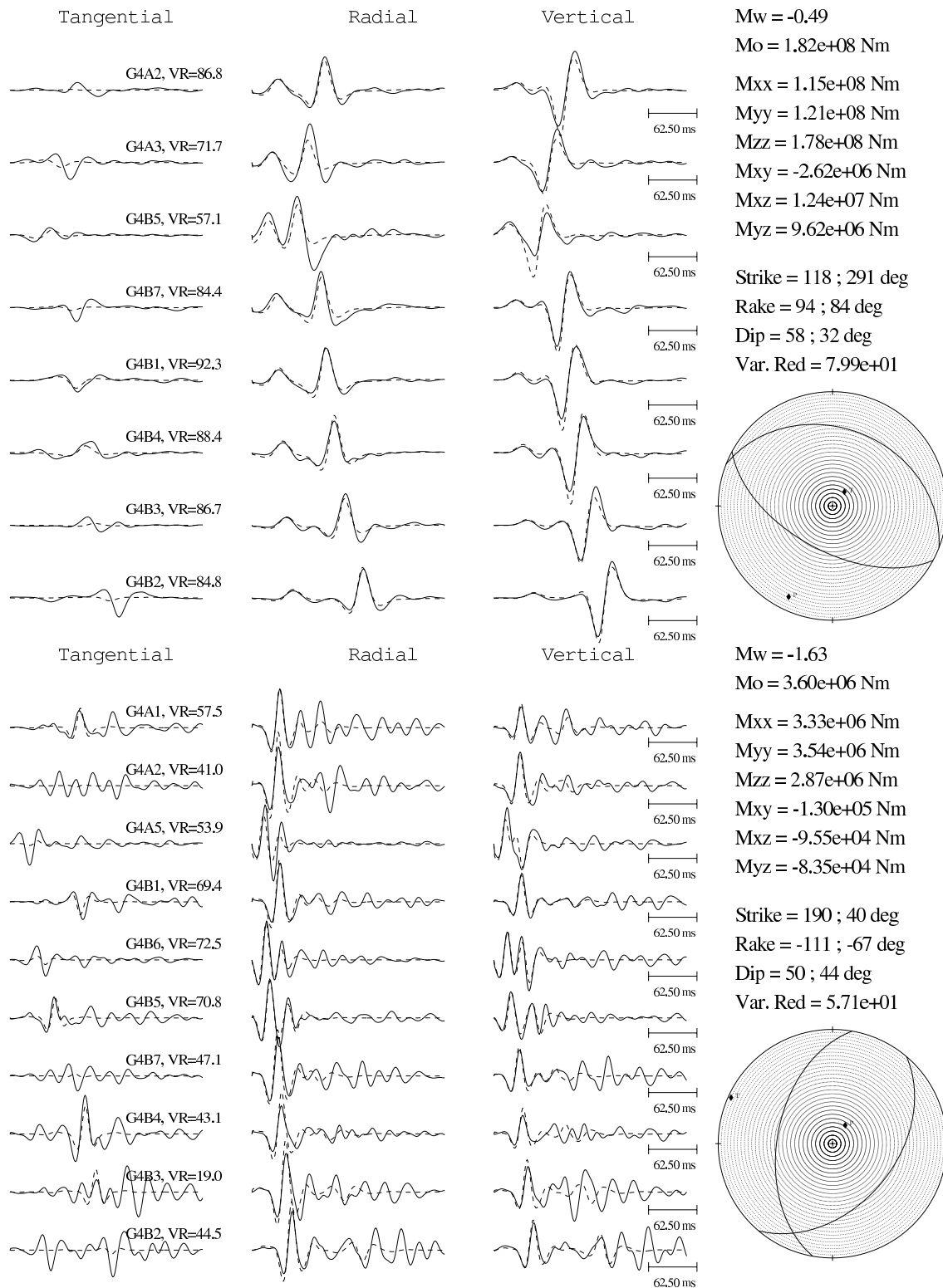


Figure 2.5: Waveform fits of explosions set off at depths of 0.5 m (upper) and 50 m (lower). Solid lines are data and dashed lines are synthetics. Epicentral locations are shown in Figure 2.1. Both fits were obtained using the full moment tensor inversion scheme. As with icequakes, the signals of the shallow explosion lack the high frequencies found in the coda of the deeper explosion. Despite some signal on the tangential component, amplitudes and phases as well as frequencies are well modelled with a variance reduction of 80 %. The variance reduction of the deeper shot is substantially lower at 57 %. This reflects the considerable quantity of signal-generated noise observed on all components. In both cases, the plot of focal mechanism indicates a highly isotropic source as expected for explosions.

to as the 'free surface effect', which arises when a seismic source is located at shallow depths compared to the wavelength used in the moment tensor inversion (Julian et al., 1998). In such cases, the normal tractions and their associated excitation coefficients vanish and consequently only three moment tensor components can be determined. The isotropic part of the moment tensor as well as M_{xz} and M_{yz} cannot be resolved. Therefore, in the approximation of a symmetric first order moment tensor, a horizontal tensile fault, for instance, located at such shallow depths does not radiate seismic waves. Ford et al. (Identifying isotropic events using a regional moment tensor inversion, submitted to the *Journal of Geophysical Research*, 2008) investigated this effect for regional moment tensor inversions of nuclear explosions using synthetic seismograms. Their results suggest that the free surface can contribute to the magnitude discrepancy between shallow and deep explosions, however it is unlikely to explain the difference of more than a magnitude. As a second reason for this magnitude difference we suggest differences in coupling of the explosion to the surrounding ice. The surface charges were placed into a much smaller hole (5 cm diameter) than the deep borehole charges (30 cm diameter). Whereas the surface charges were covered with tightly packed ice debris, the borehole charges were hanging freely in the water-filled borehole. The coupling for the borehole explosions is likely much poorer, especially in the z-direction. The low value for M_{zz} shown in Figure 2.5 (lower) reflects this.

We stress that the magnitude differences observed for the shallow and deep borehole explosions may be partially due to free-surface effects. This has to be kept in mind when comparing inversion results of shallow and deep icequakes.

2.5.2 Source Discrimination

Source-Type Plots

In order to evaluate the inversion results, we need to compare variance reductions and moment tensors determined by the three inversion schemes (full, deviatoric and crack+DC). The variance reductions are given in Table 2.1. Following Hudson et al. (1989) we use source-type plots as a means to characterize the calculated moment tensors (Figure 2.6). Source-type plots are a means to illustrate the source mechanism represented by a moment tensor using the two parameters k (near-horizontal lines) and T (near-vertical lines), which are calculated from the deviatoric eigenvalues (Equation 2.2) and the isotropic moment M_{iso} as follows:

$$T = \frac{2m'_3}{|m'_1|} \quad (2.6)$$

$$k = \frac{M_{\text{iso}}}{|M_{\text{iso}}| + |m'_1|} \quad (2.7)$$

The representation of a moment tensor using these parameters is independent of the geometry of the source, such as fault plane orientations. The parameter k characterizes the degree of isotropic component, with $k = 0$ yielding a purely deviatoric and $k = 1$ ($k = -1$) an explosion (implosion) moment tensor. Thus, any purely deviatoric source

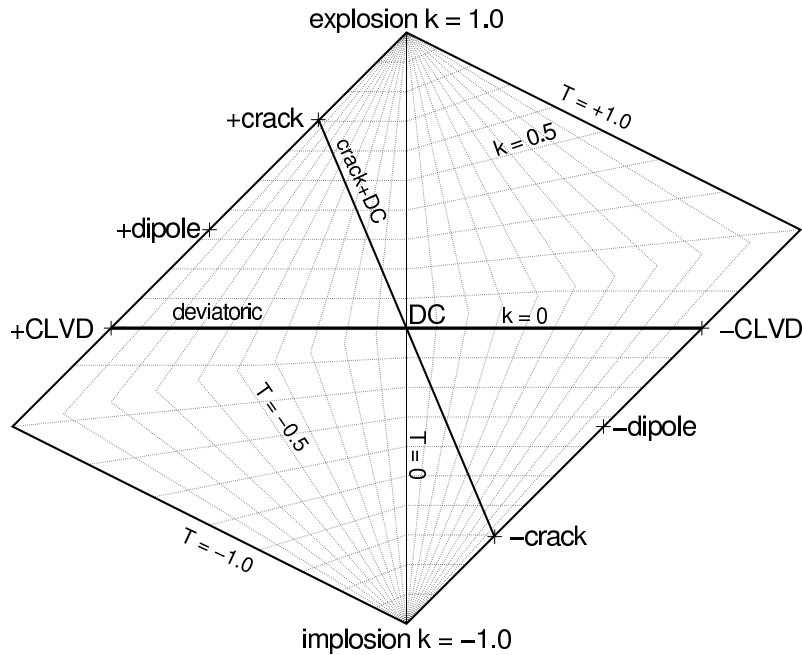


Figure 2.6: Grid for source-type plot after Hudson et al. (1989). The value T (near vertical grid lines) characterizes the deviation of the deviatoric part of the moment tensor from a pure double-couple, whereas k (near horizontal grid lines) is a measure of the strength of the isotropic component. Any given area on the plot is proportional to the probability that the (T,k) values of a completely random moment tensor lie within this area (hence the distorted shape of the source-type plot). The locations of basic source mechanisms such as double-couple, explosion, crack, dipole and CLVD are marked. Whereas (T,k) values of an unconstrained moment tensor can lie anywhere within the plot area, the solutions of deviatoric and crack+DC moment tensors lie on the indicated lines.

Table 2.1: Variance reductions (in %) of moment tensor inversion fits for the events discussed in this paper. Having the most degrees of freedom, the full moment tensor inversion scheme usually exhibits the highest fit quality. For all intermediate events, the results of the deviatoric inversion scheme show significantly lower variance reductions than those of the full and the crack+DC schemes. Small differences in station selection exist, but the band-pass filter of the events within a cluster is the same.

Event	Full	Deviatoric	Crack+DC
SURF_A 1	74	71	75
SURF_A 2	63	58	62
SURF_A 3	71	66	72
SURF_A 4	65	57	65
SURF_A 5	74	68	73
SURF_B 1	74	74	73
SURF_B 2	73	73	74
SURF_B 3	72	71	67
SURF_B 4	77	77	75
SURF_B 5	74	74	72
INT 1	64	36	62
INT 2	69	44	68
INT 3	65	50	67

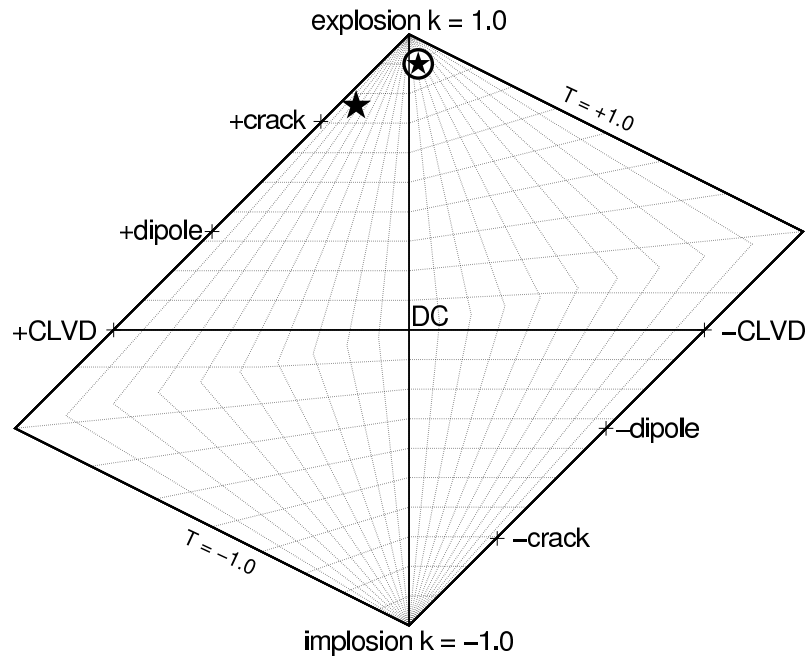


Figure 2.7: Source-type plot for moment tensors of the shallow explosion (star) and 50 m deep shot (circled star) as determined by the full inversion scheme (Figure 2.5). Both moment tensors show a large isotropic component (high k value) as expected for an explosion.

is plotted on the horizontal line $k = 0$. The parameter T indicates how much the deviatoric moment tensor component differs from a pure double-couple source. $(T, k) = (0, 0)$ represents a pure double-couple, whereas $(T, k) = (1, 0)$ and $(T, k) = (-1, 0)$ are the parameters of a pure positive and negative CLVD, respectively. The moment tensors of a tensile crack source added to a double-couple source lie on a line connecting the positive and negative crack via the double-couple location, assuming that the tensile crack and double-couple fault planes coincide (Julian et al., 1998). The special feature of source-type plots is that a given area on the (T, k) grid is proportional to the probability that the T and k values of a moment tensor lie within this area, assuming no a priori constraints on any moment tensor element.

Source-Type Plots for Explosions

Figure 2.7 shows the source-type plot of the full moment tensor inversions of the explosions. Both moment tensors have high k values meaning that they are dominated by the isotropic component. However, both solutions show some deviatoric component meaning that they are not pure explosions. This is likely an effect of shear stress released during the explosion, that can also explain some of the signal observed on the tangential components of the explosion seismograms (Figure 2.5). At the same time this may also reflect some numerical instability that a full, unconstrained moment tensor inversion is subject to. Keeping these observations in mind we will use source-type plots as approximate indicators of underlying source mechanisms.

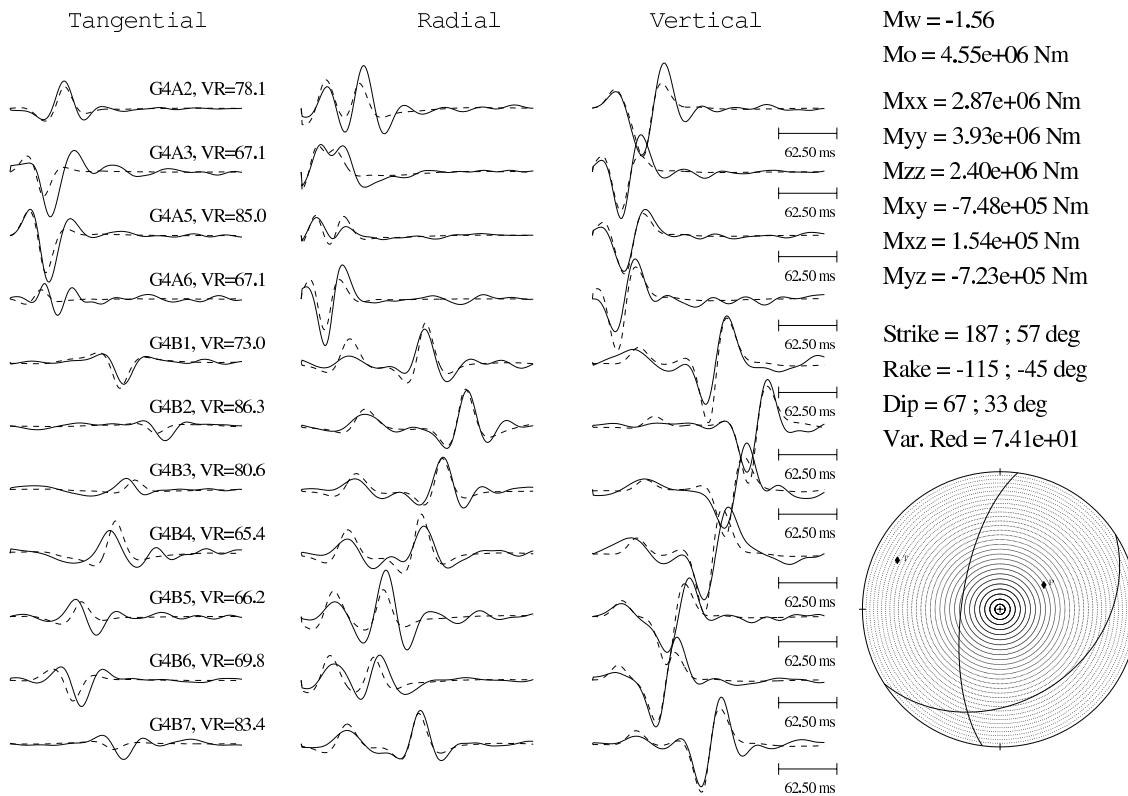


Figure 2.8: Waveform fits obtained with the full moment tensor inversion of an event belonging to surface cluster A. The fitted time series (dashed) shows good agreement with the measured data (solid) giving an overall variance reduction of 74 %. The observed isotropic first arrival pattern is consistent with the highly isotropic moment tensor (plot of focal mechanism).

Near-Surface Tensile Crack-Type Events

Table 2.1 gives a summary of the moment tensor inversion fit quality for all events considered. The corresponding moment tensors are given in Appendix B. The full moment tensor inversion usually exhibits the highest variance reduction, because it allows the maximum number of degrees of freedom.

Figure 2.8 shows the waveform fits from the full moment tensor inversion of a shallow icequake belonging to surface cluster A. With an average variance reduction of 74 %, amplitudes and frequencies of the measured seismograms are well reproduced by the synthetics. The plot of focal mechanism indicates compressive first P-motions as observed on all stations.

Panels a,d and g of Figure 2.9 show the inversion results for surface cluster A. The full moment tensor inversions indicate a dominating isotropic component (panel a). In this regime the parameter T has little significance. Given the scatter of the results, no conclusion about the nature of the deviatoric moment tensor component can be drawn. The deviatoric solutions (panel d) represent sources with mostly double-couple and some negative CLVD component. In the case of the crack+DC inversion (panel g), all solutions are dominated by the positive tensile crack opening.

Table 2.1 shows the variance reductions of the waveform fits for surface cluster A. The fit quality of the full moment tensor inversion is satisfactory at a variance reduction be-

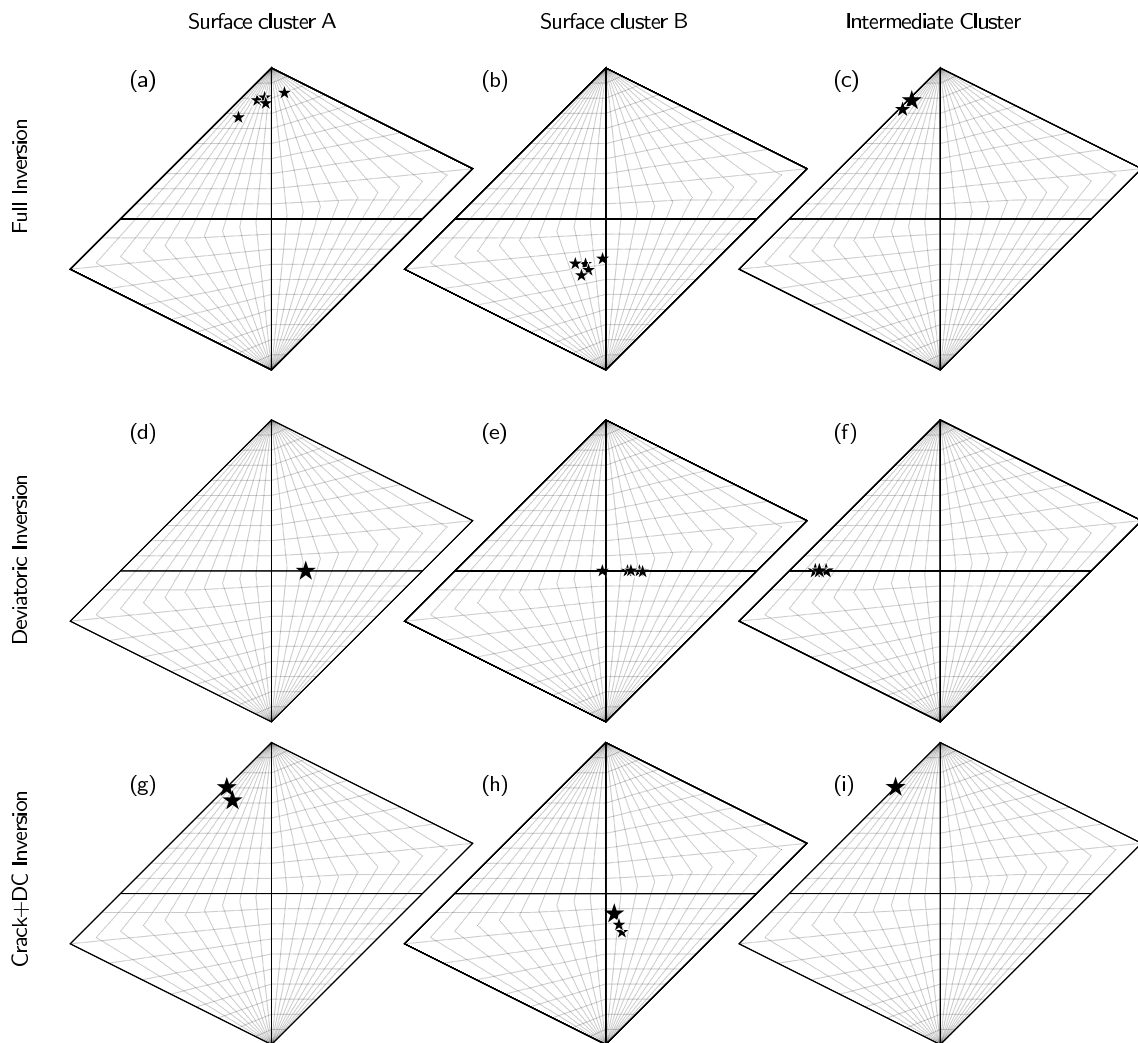


Figure 2.9: Source-type plots after Hudson et al. (1989) for the three types of icequakes investigated. Stars indicate the location of the moment tensor solutions in (k, T) parameter space. For illustration purposes, only one large star is plotted in cases where several solutions are very close together. Rows of the panels correspond to the different inversion schemes. Columns correspond to the different icequake clusters (surface cluster A, surface cluster B and the intermediate cluster; see Figures 2.1 and 2.3 for their locations). Note the large isotropic components determined by the full moment tensor inversion of the icequakes of surface cluster A and the intermediate cluster (panels a and c). In these cases the crack+DC inversion gave nearly a pure crack moment tensor (panels g and i). In case of surface cluster B, the isotropic component given by the full moment tensor inversion is much smaller and of opposite polarity compared to the other events (panel b). The deviatoric and crack+DC solutions are mostly double-couple (panels e and h).

tween about 65% and 75%. The aforementioned plot of focal mechanism in Figure 2.8 indicates a highly isotropic moment tensor, which is consistent with the compressive P-motion observed at all seismometers. The deviatoric fit is slightly worse, with variance reductions decreasing by up to 8%. The individual waveform fits show that the deviatoric fit does not reproduce the amplitude ratios of the P- to Rayleigh phase as well as does the full inversion. The variance reduction of the crack+DC inversion is closer to that of the full moment tensor inversion than the deviatoric inversion. Using F -test statistics we evaluate the significance of the lower variance reductions calculated by the deviatoric inversion considering that it has 5 free parameters as opposed to the full inversion scheme, which has 6. The number of uncorrelated data points needed in the calculation of the F -test statistics is given by the low-pass filter corner (Templeton and Dreger, 2006). An improvement of fit quality for the more complex full moment tensor model over the deviatoric model is significant if the F -test statistics indicate at least a 95% confidence level. The results show that for all but one event the fit improvement of the full moment tensor inversion over the deviatoric inversion is not significant.

Summarizing these findings, it can be stated that the crack+DC model with a dominating tensile crack component is the most likely model for the sources of surface cluster A. This is in agreement with the compressive P-arrivals observed at all recording stations. The F -test statistics nevertheless show that for all but one event a deviatoric moment tensor can model the data appropriately, too. This point will be commented further in section 2.5.2.

Near-Surface Double-Couple Events

Figure 2.10 shows an example of a waveform fit of a surface cluster B event obtained with the deviatoric inversion scheme. The overall variance reduction is 77%. The observed pattern of P-arrival polarity (Figure 2.4) is consistent with the plot of focal mechanism.

The mechanisms given by the inversions of the events belonging to surface cluster B are shown in panels b, e and h in Figure 2.9. The full moment tensor solution again contains a considerable isotropic component. However, compared to the cluster A events, it is weaker and of opposite sign. With a less dominant isotropic component, the full moment tensor inversion results indicate that the deviatoric source is more double-couple than CLVD (panel b). Accordingly, the deviatoric solution places the source mechanisms close to the double-couple region with all but one event containing a small amount of -CLVD (panel e). The crack+DC inversion recovers a moment tensor which is dominated by a double-couple source for all events (panel h) and possesses a small negative (closing) crack component. However, allowing such a negative isotropic component in the crack+DC inversion offers only an improvement in variance reduction of 1% or less compared to a pure double-couple.

Table 2.1 shows that for this cluster the highest fit quality is for the full moment tensor inversion. This time, however, the deviatoric inversion shows comparable results as does the crack+DC model for all but one event. The F -test statistics show that no single model fits the data significantly better than the other two.

In the case of surface cluster B we observe that all inversion schemes achieve comparable fit quality. The differences in variance reduction are no more than 2% for all but one event. Both the full and the deviatoric moment tensor inversion schemes indicate a dominant double-couple component. The inverted crack+DC moment tensor is dominated by

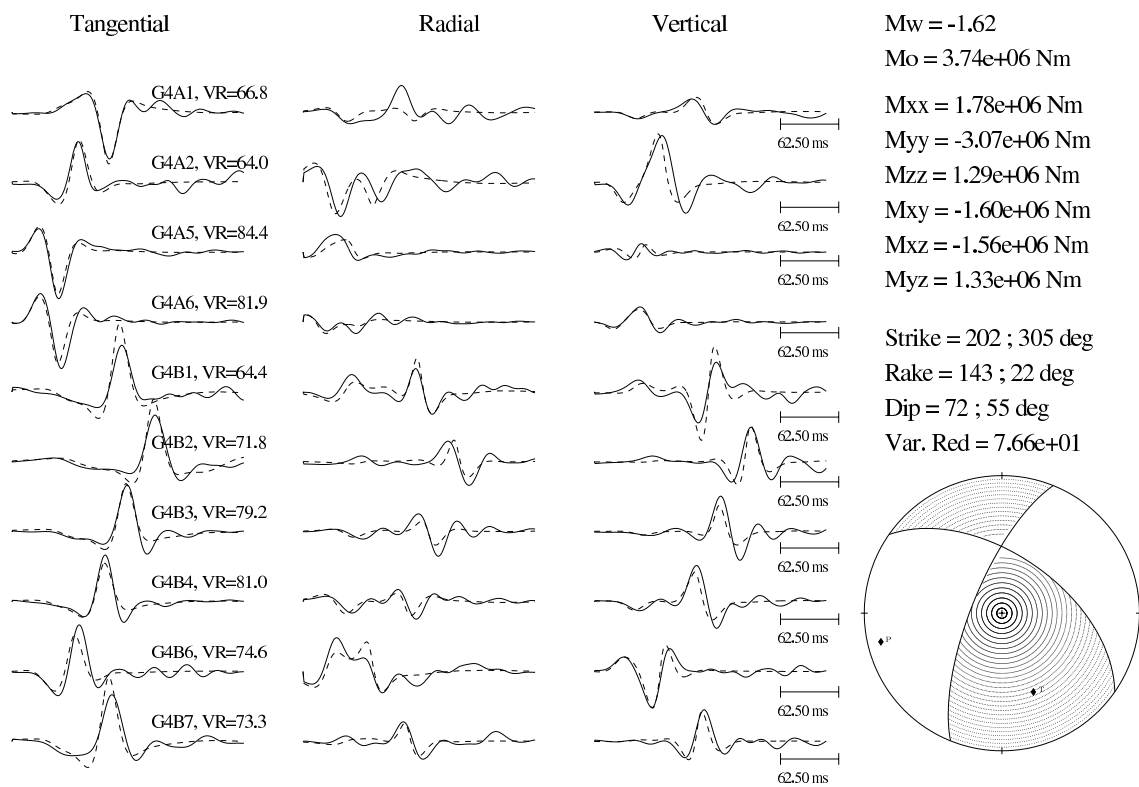


Figure 2.10: Waveform fits obtained with the deviatoric moment tensor inversion of an event belonging to surface cluster B (solid lines for data and dashed lines for synthetics). The overall variance reduction is 77%. The fault plane solution indicated by the plot of focal mechanism is consistent with the radiation pattern of first P-motions.

the double-couple component (Figure 2.9h) and improves the variance reduction by only 1 % or less compared to a pure double-couple. We therefore conclude that the events of surface cluster B have double-couple sources. This is consistent with the distribution of the positive and negative polarities of first P-arrivals observed for these events (Figure 2.4).

Intermediate Events

The source-types determined by the different inversion schemes applied to the events of the intermediate cluster are illustrated in panels c, f and i of Figure 2.9. Similarly to the near-surface tensile crack-type events, the full moment tensor inversions indicate a very large isotropic component (panel c). Unlike the other investigated clusters, the deviatoric solutions are mostly CLVD (panel f). The moment tensors calculated by the crack+DC inversion are all purely tensile crack (panel i).

As for the other clusters, the variance reductions of the full moment tensor inversion are higher than those of the other schemes (Table 2.1). The variance reduction of the deviatoric inversion lies well below that of the full inversion, in one case by nearly 40%. The fit quality of the crack+DC model is very close to that of the full moment tensor inversion. In two cases the crack+DC model performs slightly worse, which compared to the results of the deviatoric inversion appears only marginal. The F -test statistics show that for all events the deviatoric inversion fits the data significantly worse. The differences in variance reductions between the full and the crack+DC inversions, on the other hand, are not significant. Analysis of the waveform fits reveals the origin of the differences in variance reduction (Figure 2.11). Unlike the crack+DC inversion, the deviatoric constrained solution cannot model the impulsive P-phase on the radial and vertical components.

Summarizing these observations we conclude that the source-type of the intermediate events is a tensile crack opening. Being dominated by an isotropic component, such a source cannot be modelled well by a deviatoric moment tensor. This is the reason why the deviatoric inversion scheme yields significantly lower variance reductions compared to the full and the crack+DC solutions. The compressive first P-arrivals observed at all seismometers are a further indication for a strong isotropic component and are thus in accordance with the proposed tensile crack model.

Verification of Source discrimination

For the near-surface double-couple events (surface cluster B), the behaviour of the variance reduction is in accordance with a double-couple, which is the type of source suggested by information from source-type plots and waveform characteristics. All inversion schemes perform equally well. The reason is that a full, a deviatoric and a crack+DC moment tensor all include a double-couple component. Thus it is not surprising that all inversion schemes are able to produce similarly high fit qualities for the case of a double-couple source.

For the cluster at an intermediate depth the variance reduction can be used as a good discriminator for the source model, which we suggest is a tensile crack opening. Compared to the deviatoric inversion, the crack+DC model had a fit quality nearly as good as the full

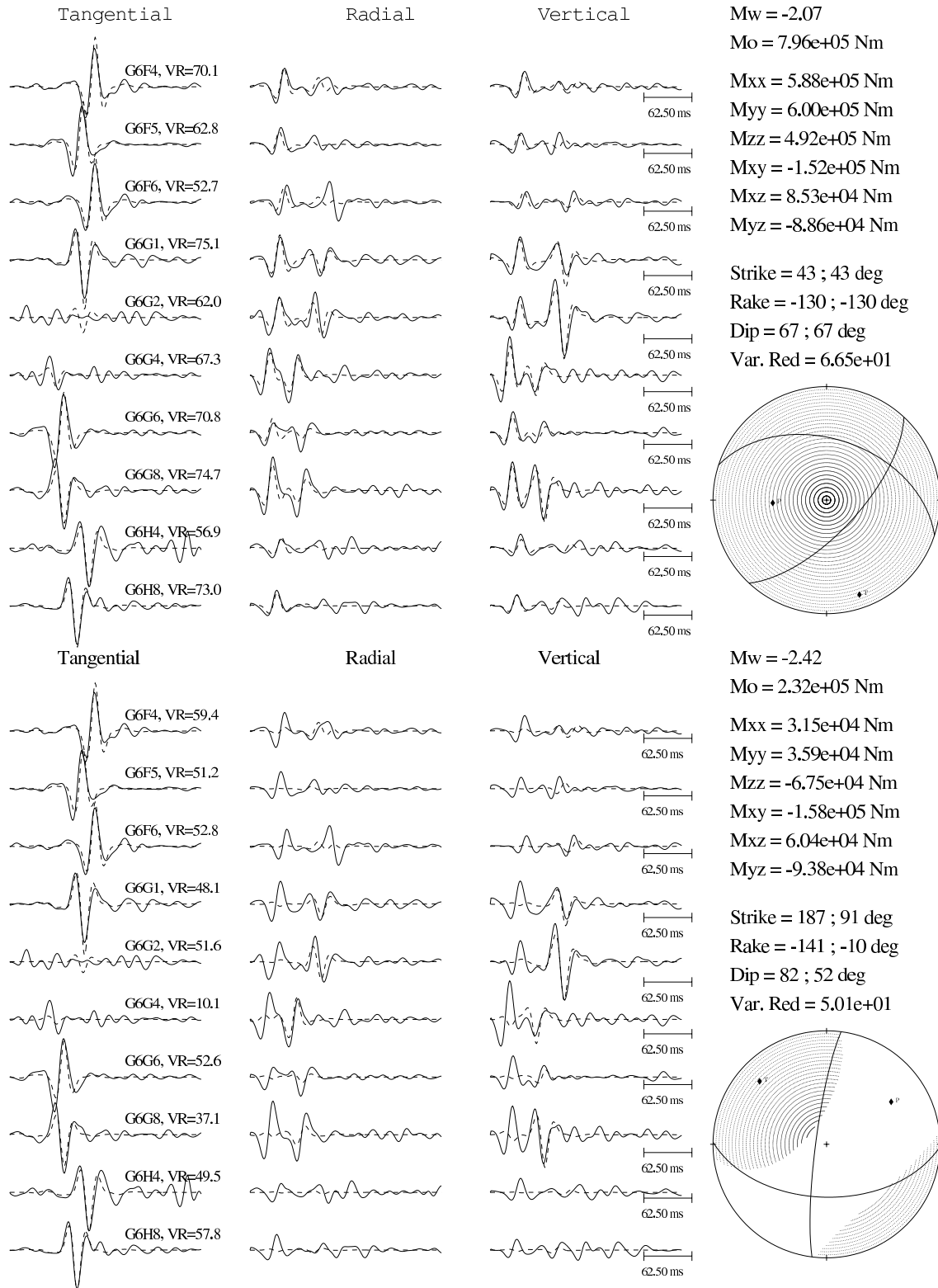


Figure 2.11: Waveform fits of an event belonging to the cluster at intermediate depth (solid lines for data and dashed lines for synthetics). The upper panel shows the fit using the crack+DC inversion scheme, the bottom panel using the deviatoric inversion. The fit quality of the latter is significantly lower (from 63 % to 47 %), because the impulsive P-waves cannot be modelled by this inversion scheme. Note that the bandpass filter introduces acausal precursors to the P-arrival.

moment tensor inversion. Dominated by the CLVD component, the deviatoric inversion, however, gave variance reductions up to almost 40% lower than the full moment tensor inversion. For tensile crack-type sources, this can be understood considering that the dominating isotropic source cannot be accounted for satisfactorily by a deviatoric model. This manifests itself in failure of the deviatoric fit to reproduce the dominant P-phase at all stations.

Despite these two cases, the solutions for the near-surface crack-type events (surface cluster A) gave variance reductions that seemed somewhat inconsistent with the evidence provided by the source-type plots and the waveform characteristics: Although we expect a tensile crack source we did not obtain a significant decrease in variance reduction when constraining the isotropic part of the moment tensor to be zero.

In order to further understand this issue we calculated synthetic seismograms for a pure tensile crack opening at 5 m and 100 m depth using an implementation of the reflectivity method (Müller, 1985, and Ungerer, 1990). Since this numerical implementation differs from the FKRPROG software (Saikia, 1994) used to generate Green's Functions, variance reductions of waveform fits of synthetic data generated with the reflectivity method may not reach 100%. The synthetic seismograms were filtered with the same band-pass filters applied to the data. The stations were placed as if the source occurred near station A4, similar to the geometry of the two surface clusters (Figure 2.1). We then inverted the seismograms using all three inversion schemes.

The inversions determined source-types that are similar to those presented in Figure 2.9. The variance reductions for the shallow tensile crack were 89% (full inversion), 86% (deviatoric inversion) and 89% (crack+DC inversion). The respective values for the tensile crack synthetics at 100 m depth were 91%, 66% and 91%. This is the same behaviour that was observed for the real data: For the deviatoric fit of the tensile crack at 100 m the fit quality is much lower than that of the full and the crack+DC one. The deviatoric fit of the tensile crack source near the surface, on the other hand, produces variance reductions that are smaller by only a few percent. As in the case for the real data, the decrease in variance reduction for the deviatoric fit of the intermediate events is mainly due to the failure to fit the P-phase.

Thus we conclude that the difference in behaviour of the variance reductions for surface cluster A and the intermediate cluster is not caused by differences in source mechanisms. At least for the frequency window used in the present work, it appears to be inherent to the source depth in general: For deeper tensile cracks, no deviatoric moment tensor can be found to satisfactorily model seismograms of a tensile crack opening, whereas for shallow events it is possible to some degree. This problem may not occur at other frequencies. However, the frequency content of signal and noise did not allow for moment tensor inversions at other frequency windows. It should be emphasized that for both the 5 m as well as the 100 m deep synthetic tensile crack the stations were placed in the same geometry around the epicenters. Therefore, the inversion results of the synthetic seismograms show that the equal ability of multiple models to fit the data is not an artifact of azimuthal coverage of recording stations.

Minson et al. (2007) were faced with a similar challenge discriminating source mechanisms for the 2000 Miyakejima volcanic earthquake swarm. Most of the sources were around 5 km deep. Considering the scaling relation applied in the present work, this depth corresponds to that of the surface clusters. Similar to the solutions of the surface cluster A

events, the variance reductions of various models used to fit most Miyakejima waveforms showed only small differences for most events. Yet the authors argued for the crack+DC model because it constitutes a likely physical model for volcanic events and it allowed forward modelling seismograms using inversion results of geodetic data. The first argument has considerable validity in the present work, as well: As a mechanism likely responsible for crevasse openings the tensile crack model represents the most plausible source for seismic signals in glacier ice.

We furthermore used synthetic seismograms to evaluate the significance of the negative isotropic moment obtained for full and crack+DC inversions of the surface cluster B events (Figure 2.9b and 2.9h). A double-couple source was placed at 5 m depth with the same station distribution that had been used for the previous calculations of synthetic seismograms. The fault plane orientation of the synthetic source was equal to the result of the crack+DC inversion of a surface cluster B event.

The full as well as the crack+DC inversion of the shallow double-couple synthetics both give a negative isotropic moment. The crack+DC inversion produces source type parameters similar to those shown in Figure 2.9h. The full inversion determines a slightly positive T value and a negative k value whose magnitude is about one third of the values given by the full inversions of the surface cluster B events (Figure 2.9b). We conclude that the negative isotropic moment calculated by the full and crack+DC inversions of the surface cluster B events is not significant because the inversions of synthetic seismograms of a pure double-couple source show this negative isotropic component, too. Furthermore, the crack+DC model with a negative isotropic moment provides an improvement in variance reduction of only 1 % or less compared to a pure double-couple. The negative isotropic moment is likely another manifestation of the effect that the free surface has on the resolution of the isotropic component.

Interpretation of Mechanisms

Table 2.2 gives a summary of source parameters given by the moment tensors of the crack+DC inversion. Moment magnitudes were calculated using equations 2.2, 2.3 and 2.4. Recall that for the events of surface cluster A and the intermediate cluster the tensile crack component strongly dominates the solution, whereas for those of surface cluster B the double-couple component is dominant. The rake values of the tensile crack-type events therefore carry little physical significance. Those of surface cluster B are around 150° . The strike values reflect orientations from South-West to North-East for all types of events. This is consistent with the local pattern of surface crevasses (see Figure 2.1). The dip values range from near-vertical to as low as 50° . Volumetric changes only occur for the tensile crack-type sources. According to Müller (2001) the volume of a tensile crack can be calculated from the isotropic moment M_{iso} of a moment tensor via

$$\Delta V = M_{\text{iso}}(\lambda + 2\mu/3), \quad (2.8)$$

where λ and μ are the Lamé parameters. The changes of the tensile crack volume calculated via Equation 2.8 are on the order of 100 cm^3 (Table 2.2). The sources of surface cluster A tend to undergo a larger volumetric change than the intermediate events. However, these differences in source parameters between shallow and deep events may at least partially be caused by effects of the free surface as discussed for the explosion inversions.

Table 2.2: Fault plane orientations, moment magnitudes and volumetric changes (in cm^3) calculated from the moment tensors given by the crack+DC inversion. Values for strike (measured clockwise from north), dip and rake are given in degrees. Note that surface cluster A and the intermediate cluster represent almost entirely tensile crack events, whereas surface cluster B is double-couple. Hence, the rake is of significance only for the surface cluster B sources. Volumetric changes were calculated via equation 2.8. Equation 2.2 was used to determine the moment magnitude of the surface cluster B events. They are in good agreement with the moment magnitudes determined with Equation 2.4 (numbers in parenthesis). The M_w for the remaining events was estimated using Equation 2.3.

Event	Mechanism	Strike	Dip	Rake	ΔV	M_w
SURF_A 1	crack	40	50	-60	320	-1.6
SURF_A 2	crack	198	80	108	110	-1.9
SURF_A 3	crack	202	78	105	400	-1.6
SURF_A 4	crack	215	85	50	140	-1.8
SURF_A 5	crack	36	86	-28	290	-1.6
SURF_B 1	DC	208	68	156	-77	-1.7 (-1.6)
SURF_B 2	DC	208	73	152	-100	-1.8 (-1.6)
SURF_B 3	DC	200	70	156	-26	-2.3 (-2.1)
SURF_B 4	DC	202	72	144	-77	-1.7 (-1.6)
SURF_B 5	DC	202	67	150	-90	-1.8 (-1.7)
INT 1	crack	31	71	-60	90	-2.1
INT 2	crack	35	69	-95	110	-2.1
INT 3	crack	43	67	-130	100	-2.1

The shear faulting of surface cluster B sources produces a negative volumetric change. Their absolute values are smaller than in the case of the surface cluster A events. As discussed in Section 2.5.2 these volumetric changes are likely numerical artifacts of the inversion and do not have a physical meaning. The calculated moment magnitudes of all events lie within the range from -2.3 to -1.5. For the events of surface cluster B the moment magnitudes are verified by Equation 2.4.

2.6 Discussion

Icequakes originating from near the glacier surface have been associated with crevasse openings since the work by Neave and Savage (1970) on the Athabasca Glacier in Alaska. We inverted a set of events with tensile crack-type mechanisms, which is consistent with the findings of the Athabasca study. Although we have only located less than a percent of the icequakes recorded in 2004 and 2006, the results of the waveform discriminator and our experience from looking at thousands of seismograms show that the tensile crack-type surface events (surface cluster A) are representative for well over 99 % of the data set.

We also determined the source mechanisms of two different icequake types, which, according to their frequency of occurrence, can be considered somewhat atypical. The first set is also composed of surface events, but it differs from the typical crevassing events in that the sources are double-couple rather than tensile crack-like. Aside from the implication that they are due to shear failure rather than tensile failure, the events are not associated with volumetric change. Table 2.2 shows that the shear fault planes of the surface double-couple events (surface cluster B) are very similar to the tensile fault planes of

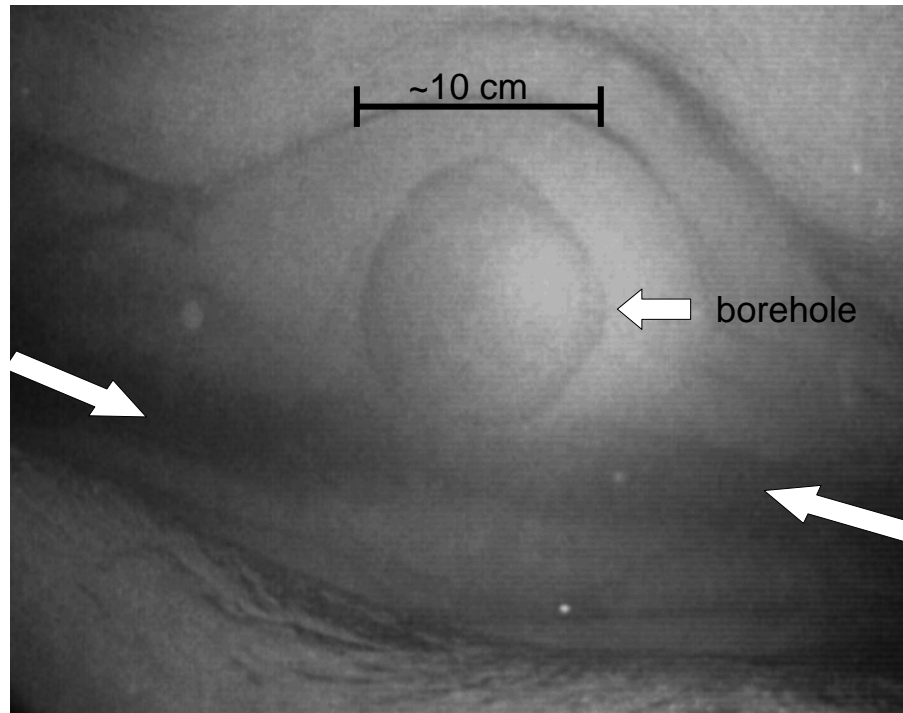


Figure 2.12: Picture taken inside a borehole at a depth of 270 m about 1200 m down-glacier from the center of the seismic networks in 2004 and 2006. The glacier is over 300 meters deep at this location. The picture shows clearly the intersection of the borehole with a crack (the two arrows at the side of the picture are along the strike of the crack), whose walls are on the order of a few centimeters apart. Openings of such cracks may be accompanied by the kind of intermediate depth icequakes studied in the present work.

surface tensile crack-type events (surface cluster A). It has to be stressed that in this study we only concentrated on a few events out of the many thousands that have been detected each day. However, it is interesting to note that the shear-type events occur at the onset of the drainage of Gornensee. This observation suggests that shear failure is a response to the lake drainage, which is known to have the potential to significantly alter the glacier's flow direction (Sugiyama et al., 2007; Riesen, 2007). In order to support this conjecture, a procedure to search the entire data set has to be developed.

The members of the intermediate cluster form another example of icequakes that cannot be attributed to the opening of surface crevasses. At these depths, it is reasonable to assume that in the absence of water that reduces the effective stress, the ice-overburden pressure inhibits tensile fracturing (Van der Veen, 1998b). The tensile crack-type source mechanisms of the intermediate events therefore suggest that icequakes at these depths are related to hydrofracturing. This is consistent with observations of englacial fracturing made inside boreholes. Figure 2.12 shows an example of an englacial fracture intersecting a borehole drilled about 1200 m down-glacier of the seismic networks in 2005. Such fractures have also been observed in other studies (Harper and Humphrey, 1995; Meierbachtol et al., 2006; and Fountain et al., 2005) and may have a significant influence on water flow inside temperate glaciers.

Limitations of Inversion Schemes

The most serious limitation of applying the Dreger (2003) approach is probably the one-dimensional velocity model. This does not allow us to account for topographic details of the glacier. Although these are only on the order a few percent of most of the source-receiver distances, the fit quality of the inversion is expected to suffer. The modelled travel times, for example, introduce small uncertainties, since the seismic stations do not lie exactly in a horizontal plane, as assumed by the applied velocity model. Of even greater concern is the topography of the glacier bed, which beneath the seismic arrays of 2004 and 2006 has an inclination of 30° or more (Figure 2.3). Therefore, the ice-bedrock interface cannot be described in a one-dimensional velocity model. For this reason, the present study focuses only on the icequakes that occur at a distance from the glacier bed where bed reflections can be neglected.

Lateral inhomogeneities, such as crevasses, may have some effect on the waveforms that the bandpass filter cannot eliminate. Crevasses furthermore increase the waveform attenuation of the glacier ice near the surface. Since the surface fractures inside the study site tend to align (Figure 2.1), this can constitute an effective anisotropy of waveform attenuation as well as seismic velocities (Gischig 2007). As a consequence, seismic waves travelling perpendicular to the surface crevasses are slower and decay faster than those propagating parallel to the surface crevasses.

Moment tensor inversions of seismic sources near free surfaces are subject to numerical limitations independent of the numerical scheme used. If the sources are located at shallow depths with respect to the wavelength used in the inversion, the isotropic part of the moment tensor cannot be fully recovered (Dufumier and Rivera, 1997; Julian et al., 1998). In the present study this likely introduced errors in isotropic moments such as artificial negative volumetric changes for the double-couple sources of surface cluster B.

2.7 Conclusion

Using a simple scaling relationship and 1D Green's Functions for a homogeneous half space, we have successfully applied full as well as constrained moment tensor inversions schemes to seismograms from glacial icequakes recorded in dense campaign seismic networks on Gornergletscher, an alpine glacier in Switzerland. By interpreting the resultant moment tensors in terms of plausible physical models and scrutinizing the fit qualities of the inversions we arrived at the following central results: The sources for the vast majority of the several thousand icequakes measured each day are tensile crack openings near the glacier surface. Fault plane orientations indicate that these seismic events are associated with surface crevasses opening. The volumetric changes associated with these sources were calculated to be between 100 cm^3 and 400 cm^3 . Shear-type events near the glacier surface do occur, although they occur much less frequently than tensile crack openings. The moment magnitudes of these events are between -2.0 and -1.5. The existence of shear-type events indicates that icequakes near the glacier surface are not only produced by crevasse openings, as suggested by previous studies (Neave and Savage, 1970; Deichmann et al., 2000). Tensile crack-type seismic events also occur at intermediate depths within the glacier. Volumetric changes of these sources are about 70 cm^3 . At intermediate depths, the hydrostatic pressure inside the ice induced by the ice-overburden pressure is

expected to be high enough to inhibit tensile fracturing. We therefore suggest that the intermediate events are related to the presence of water that reduces the effective stress to allow for tensile faulting.

In order to identify these distinct source-types it is necessary to evaluate information from fit qualities, source-type plots and waveform characteristics. Especially for the near-surface events it is insufficient to consider solely the variance reduction of the waveform fits, since at the employed frequency range all three inversion schemes (full unconstrained, deviatoric only and crack+DC) can be expected to, and do achieve a satisfactory waveform fit of a tensile crack source. This underlines the difficulties inherent to source discrimination and the need to carefully consider which solution is physically most plausible. In the context of source discrimination it should be noted that source-type plots of full moment tensor inversion results clearly separate double-couple events from tensile crack-type events, because the latter have a large isotropic component (Figure 2.9a-c). This is in good agreement with the findings of Ford et al. (Identifying isotropic events using a regional moment tensor inversion, submitted to the *Journal of Geophysical Research*, 2008).

In general, it can be stated that the available data set was highly suitable for moment tensor inversions. The dense seismometer arrays provided a wealth of high-quality data. Furthermore, the high homogeneity of alpine glacier ice allows for the application of a simple velocity model to generate Green's Functions. The procedure applied in this study can be very helpful in other studies of superficial or englacial fracturing provided the recording array is of sufficient quality and density to record 'broadband' icequakes and accurately locate events. O'Neel and Pfeffer (2007) find that fracture processes inside tidewater glaciers may significantly weaken ice prior to glacier calving. Calculations of tensile crack opening volumes such as presented here will help understand the conditions under which a calving event will eventually occur. In Greenland, melt-water lakes can drain catastrophically through fractures, thus increasing the englacial seismic activity (Das et al., 2007). Accurate locations and source parameters may elucidate how the seismic activity is related to the water passage.

As previously mentioned, we have observed a small but significant number of basal icequakes with high confidence. In this paper, we have not presented any moment tensors for these events. In the case of Gornergletscher, the geometry of the glacier bed (Huss et al., 2007; Figure 2.1) requires that Green's Functions for a two or three dimensional seismic velocity model have to be calculated. Despite this complication, the study of basal icequakes is highly valuable to a variety of glaciological aspects. These seismic signals can be related to stick-slip motion (Roux et al., 2008; Weaver and Malone, 1979; Wiens et al., 2008), the failure across basal ice layers during the breaking off of hanging glaciers (Faillettaz et al., 2008) or changes in basal sliding due to changes in basal water pressures (Walter et al., 2008). Thus icequakes occurring near the glacier bed should be a focus of future efforts of source parameter calculations.

Chapter 3

Evidence for Near-Horizontal Tensile Faulting at the Base of Gornergletscher, Switzerland

FABIAN WALTER¹, DOUGLAS S. DREGER², JOHN F. CLINTON³,
NICHOLAS DEICHMANN³, MARTIN FUNK¹

¹Versuchsanstalt für Wasserbau, Hydrologie und Glaziologie (VAW), ETH Zürich, 8092 Zürich, Switzerland

³Berkeley Seismological Laboratory, Berkeley, California-94720, U.S.A.

²Institut für Geophysik, ETH Hönggerberg, CH-8092 Zürich, Switzerland

Submitted to the Bulletin of the Seismological Society of America
on February 25, 2009, but not accepted
for publication as of March 11, 2009.

ABSTRACT: Using 3D Green's Functions we determine full and constrained moment tensor solutions of icequakes near the base of Gornergletscher, Switzerland. The seismic events were recorded in the summer 2004 using a high-density seismometer array. The seismic velocity model used in the generation of Green's Functions is based on radio-echo soundings to approximate the basal topography, which beneath the study site exhibits a strong inclination. As the basal conditions are not well known, we try moment tensor inversions with seismic velocity profiles consisting of two and three media. The former case consists of homogeneous ice resting on bedrock, whereas the latter case includes a thin basal layer with slow seismic velocities representing eroded material or highly fractured ice. Effects of errors in Green's Functions are estimated by sensitivity studies in which we invert 1D and 3D synthetics using Green's Functions of wrong velocity models. The results show that calculations of source types and fault plane orientations of tensile cracks are rather robust with respect to errors in Green's Functions. However, the quality of the waveform fits depends on strike and dip of the synthetic source. When inverting seismograms, Green's Functions of the seismic model that includes the basal slow velocity layer are found to give the most realistic source types as well as the best waveform fits. The fault mechanisms derived from constrained moment tensor inversions are near-horizontal tensile cracks, which suggests a complex time-dependent basal stress field.

3.1 Introduction

Seismic radiation from large bodies of ice has recently been the focus of various glaciological and seismological investigations. The seismic signals range from 'glacial earthquakes' (Ekström et al. 2003; Wiens et al. 2008), which can be detected on global seismic networks, to 'icequakes', which are only detectable with instruments on or in the immediate vicinity of the glacial body. Icequakes have been shown to accompany crevasse openings (e. g. Neave and Savage, 1970; Walter et al., 2009) and can be precursors to glacier calving (O'Neel et al., 2007; O'Neel and Pfeffer, 2007) and the breaking-off of hanging glaciers (Faillettaz et al., 2008).

Icequakes occurring near the glacier bed have been studied in the context of stick-slip motion (Roux et al., 2008; Weaver and Malone, 1979; Anandakrishnan and Alley, 1994) or subglacial hydrology (Walter et al., 2008). Such basal events are of particular interest, because they can provide information about a glacier's basal dynamics and hydrology as well as the nature of the ice-bedrock interface. As the glacier bed is difficult to access with many other glaciological and geophysical methods, seismic measurements are a valuable alternative.

Hydrological processes are particularly important for temperate alpine glaciers, as large amounts of meltwater flow through and under the glacier and can significantly influence ice dynamics. Metaxian et al. (2003) showed that englacial water flow causes seismicity on Cotopaxi, a glaciated volcano in South America. The authors considered frequency contents of seismic signals to show that their sources are likely due to resonances of water-filled ice cavities. Walter et al. (2008) compared the activity of basal icequakes to subglacial water pressures and glacier surface motion and concluded that during low-pressure episodes basal ice layers deform so rapidly that fracturing is induced.

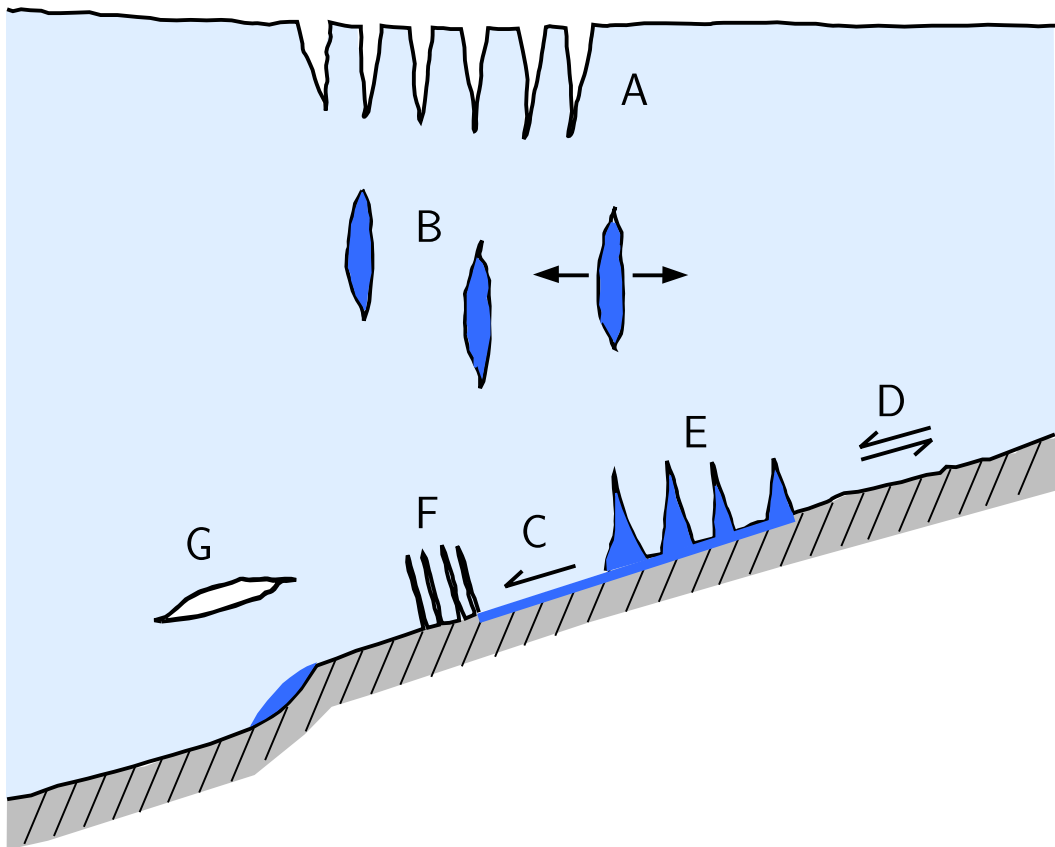


Figure 3.1: Schematic overview of possible fracture processes in glacier ice. Light blue indicates glacier ice and dark blue liquid water. At the bed, water enhances glacier sliding. (A) Near the glacier surface both tensile as well as shear fracturing is possible (Walter et al., 2009). (B) Englacial tensile fracturing is related to the presence of water lenses. Near the glacier bed, stick-slip motion may cause tensile failure either at the ice-bedrock interface (C) or within the basal ice layer (D). Tensile failure near the glacier base may result from spatial variations in sliding (E) or it may occur above rapidly closing water-filled cavities (G). Furthermore, tensile collapses (F) may occur in zones of compression.

Figure 3.1 gives a schematic overview of possible fracture sources at different depths of a glacial body. A central yet open question concerns the mechanisms of basal icequakes. Are these seismic events a consequence of tensile or shear failure? Using full waveform inversions Walter et al. (2009) calculated moment tensors of icequakes near the surface and at intermediate depths. The results show that near the surface, tensile failure is predominant, however shear failure is also possible. At intermediate depths, icequakes are due to tensile failure suggesting the presence of water lenses, which reduce the effective pressure within glacier ice. Near the glacier base, several possibilities for fractures that emit seismic energy exist. For example, stick-slip motion may cause shear failure across the glacier bed or within the basal ice layer. Furthermore, unevenly distributed basal water may cause spatial variations in basal sliding. As a consequence, zones of longitudinal stretching or compression can undergo tensile fracturing or collapsing, respectively. Another possibility is the temporal evolution of water-filled cavities near the glacier bed. Iken (1981) showed that when the water pressure inside such a cavity drops, basal ice quickly flows into the cavities to close them. The ice above such a cavity may then deform rapidly enough to fracture.

In this study we perform full waveform inversions to determine full and constrained moment tensors of icequakes that occur near the glacier base. We focus on a cluster whose events have particularly clean signals. The proximity of the seismic sources to the glacier bed makes the generation of 3D Green's Functions necessary. In order to estimate the effect of errors in the glacier bed topography on the moment tensor inversion, we also performed sensitivity studies.

3.2 Study Site

Located in Canton Valais near the Italian border, Gornergletscher is Switzerland's second largest glacier (Figure 3.2a). Although parts of Gornergletscher consist of cold ice, which is advected from high-altitude accumulation areas to the glacier tongue (Eisen et al., 2008), most of the glacier is temperate. Gornergletscher has been in the focus of recent monitoring and numerical ice-flow modelling efforts mainly because of the drainage of an ice-marginal lake, Gornersee, located at the confluence area of the two main tributary glaciers (Figure 3.2b). With the advent of the melt season, this glacier-dammed lake fills every spring over the course of several months and drains catastrophically in the subsequent summer, often within days (e. g. Huss et al., 2007).

The lake drainage has a severe impact on the ice dynamics of the glacier tongue (Sugiyama et al., 2007). As a consequence, the glacier's seismic activity also reacts to the lake drainage (Walter et al., 2008; Aschwanden, 1992). We have deployed campaign seismic arrays consisting of up to 24 seismometers during four lake drainages. Figure 3.2b shows the 2004 seismic network consisting of 13 surface seismometers and one borehole seismometer installed in a borehole at a depth of 100 m. For a detailed description of instrumentation and data processing the reader is referred to Walter et al. (2008).

Whereas the surface of the tongue of Gornergletscher is nearly horizontal, the bed is strongly inclined, particularly beneath the study site (Figure 3.2b and d). The basal topography was derived from radio-echo soundings as described in Sugiyama et al. (2008).

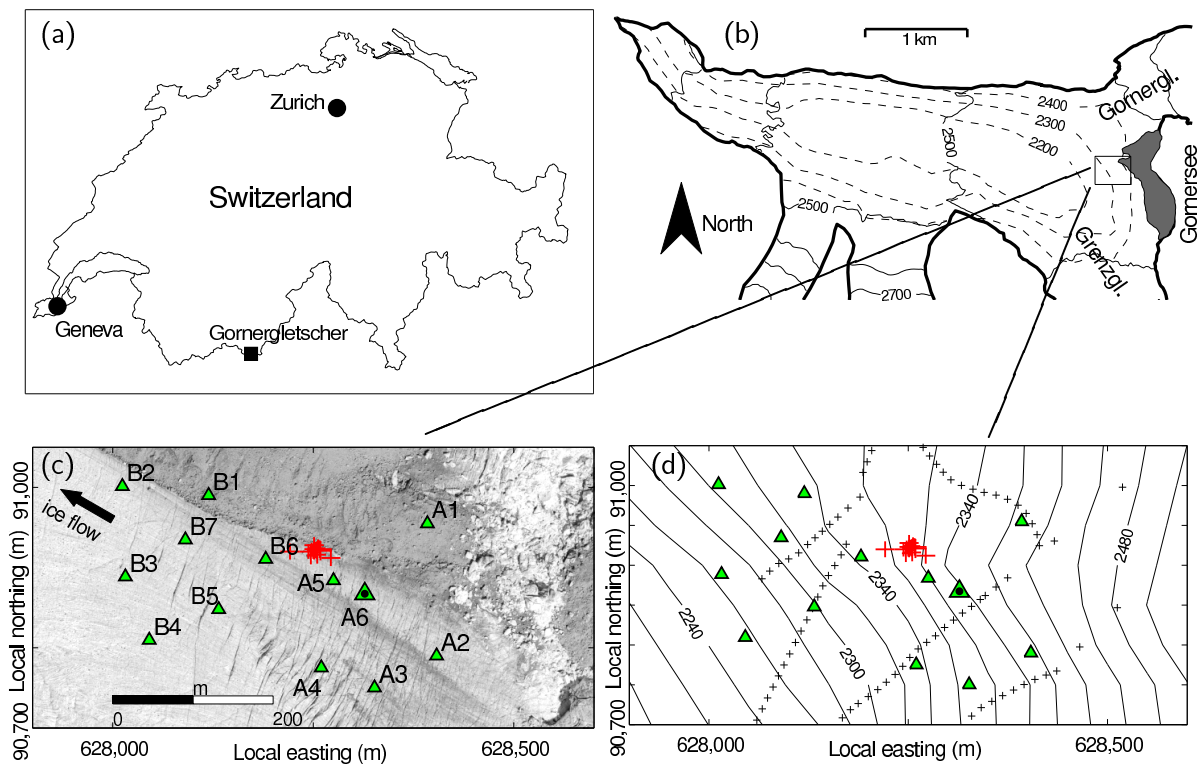


Figure 3.2: Overview of the study site. Location of Gornergletscher in Switzerland's Canton Valais (panel a). The tongue of Gornergletscher is shown in panel b. The dashed and solid contour lines approximate the glacier bed and surface topography, respectively. The 2004 seismic network was installed in the boxed region near Gornerssee. Panel c shows an orthographic photo of this part of the glacier, taken after the lake drainage in 2007. Green triangles indicate seismometer locations. A 100 m deep borehole seismometer was installed beneath station A6 (dotted triangle). Epicentral locations and their uncertainties are indicated by the red crossbars. Panel d shows the locations of radio-echo soundings (small crosses) used to derive the basal topography at the study site (solid lines show the contour lines of the bed topography).

Uncertainties were estimated to be 10 % of the ice thickness. Although a wealth of radio-echo soundings exists in the region of the seismic array, the epicentral area of the basal icequake cluster of the present study was not covered by measurements (Figure 3.2d). To estimate the bed topography in areas where no radio-echo soundings are available, Sugiyama et al. (2008) interpolated measurements using the method of Akima (1978). In order to introduce some smoothing and to avoid unrealistic topographical details of the glacier bed near the basal cluster, three fix points were manually added.

As the glacier bed is difficult to access, the material properties of the ice-bedrock interface are often subject to large uncertainties. It is therefore often unclear if the glacier rests directly on bedrock or if ice and bedrock are separated by a sediment layer. For instance, seismic and geoelectric measurements have shown the presence of a till layer beneath parts of Unteraargletscher, which is located in the Bernese Alps (Knecht und Süssstrunk, 1952; Funk and Röthlisberger, 1989). Near the study site of the present work, however, many rock surfaces that have been exposed in the course of glacial retreat show no presence of large till layers. Furthermore, the high inclination of the bed beneath the study area suggests that basal sediments are likely to be washed away by subglacial water flow. Yet we cannot exclude the possibility that some eroded material is present - at least locally - near the glacier base. In the present work we will therefore take into consideration the presence of unconsolidated material near the glacier bed by including in our model a basal layer with a slow seismic velocity.

3.3 Basal Icequakes

We have identified and located about 500 basal icequakes from the summer field campaigns of 2004, 2006 and 2007. In all years it was found that basal icequakes usually occur in clusters, which are active during low or decreasing water pressures, a condition that is usually met at night or during the early morning hours. This corresponds to periods of glacier surface lowering. These observations suggest that after enhanced sliding episodes, coupling of the glacier to its bed deforms the basal ice layer enough to fracture it. Details of these findings as well as information about location and waveform discrimination algorithms can be found in Walter et al. (2008).

Basal icequakes appear to be more abundant than icequakes occurring at intermediate depths (Deichmann et al. 2000; Walter et al., 2009). This also suggests a relation to motion and deformation of basal ice layers. In the present work we assume that basal icequakes occur within the ice and not within the underlying glacier bed. Good location results based on a seismic velocity model which ignores the bed, and similar signal strength of intermediate and basal icequakes support this hypothesis.

We have observed substantial differences in the waveforms of basal icequakes, which suggests a variety of possible source mechanisms. A common feature is their high frequency content, contrary to surface icequakes, which are usually dominated by low-frequency Rayleigh waves (Walter et al., 2009). Waveform modelling of basal icequakes thus depends on the success to simulate the direct P- and S-waves as well as their basal reflections. The majority of basal icequakes shows compressive first motions at all recording azimuths, indicating a highly isotropic tensile crack mechanism.

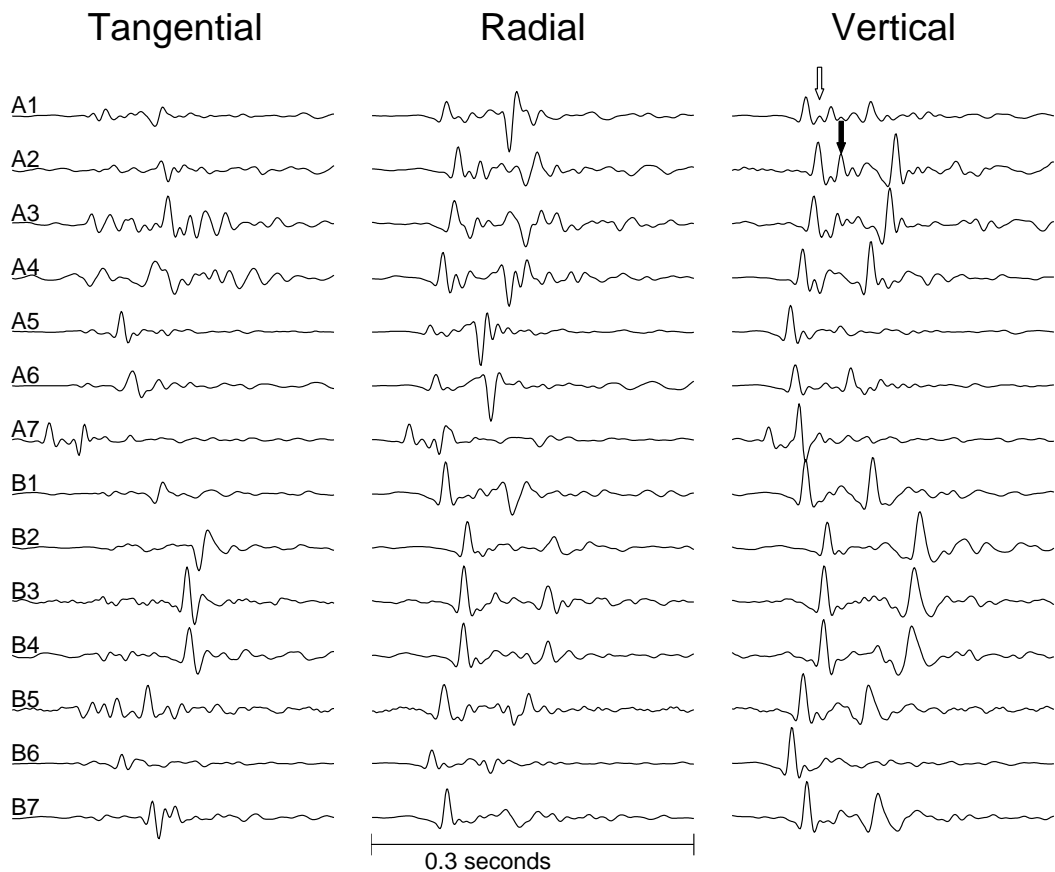


Figure 3.3: Ground displacement seismograms of a basal event that occurred on June 16, 2004, at 05:58:12. For clarity, the signals were filtered between 20 Hz and 120 Hz. Note the relatively simple waveforms consisting mainly of P- and S-phases. The arrows indicate two secondary phases that are typical for the events of this cluster. Their origin is not known.

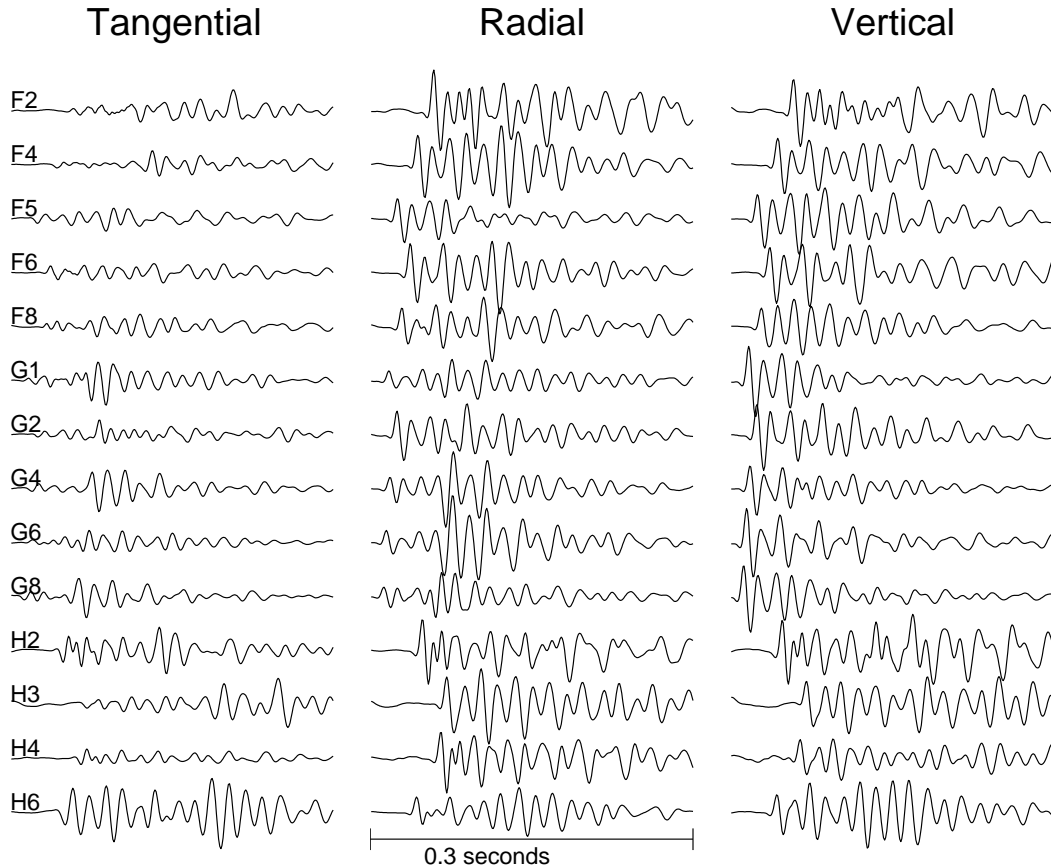


Figure 3.4: Ground displacement seismograms of a basal event recorded in 2006. For clarity, the signals were filtered between 20 Hz and 120 Hz. The waveforms strongly differ from the ones shown in Figure 3.3, because they exhibit relatively long coda.

We focus on a basal cluster recorded in 2004. The events cluster at a depth of about 154 m, close to the glacier bed. A seismogram of an icequake belonging to this cluster is shown in Figure 3.3. This seismogram shows features typical for this cluster: 1. First arrivals are compressional at all recording azimuths. 2. The signals are rather simple consisting mainly of the P- and S-phase. 3. There are two small phases that are common to most events of this cluster: The black arrow marks a phase between the P- and S-wave, which can be noted mainly on stations A1, A2 and A3. The origin of this phase is not clear. The white arrow indicates a small phase after the P-wave that can be noticed on nearly all stations. We have tested the hypothesis that this phase is the basal reflection via 1D waveform modelling. The lag between this phase and the direct P-wave is consistent with a reflection off the glacier bed if it is separated from the source by about 22 m. However, in this case, synthetic waveforms also show a large S-reflection, which cannot be seen in the data. This indicates that the small phase behind the P-wave is not a reflection, but has a different origin. We thus conclude that the source is close enough to the glacier bed that reflections are part of the direct arrivals. Through waveform modelling we found that this is the case if the source is separated by about 10 m or less from the glacier bed.

These basal cluster events share waveform characteristics with many other basal icequakes recorded during the 2004, 2006 and 2007 field campaigns. However, they also distinguish themselves from a number of other basal events. Figure 3.4 shows an example

of a seismogram of a different type of basal icequake. This event was recorded in 2006 by a seismic network similar to the 2004 network. Apart from the impulsive first arrivals, these waveforms do not resemble the ones shown in Figure 3.3. They possess a long coda, which makes it difficult to identify S-wave arrivals. The coda may be caused by reflections, trapped waves or water resonances near the source. As source modelling of such an event is extremely difficult and may not be possible with moment tensor representations, we focus the current study on events with simple waveforms as shown in Figure 3.3.

3.4 Inversion Scheme

3.4.1 Formulation of Inverse Problem

The elastic response at time t and location \mathbf{x} relative to a seismic source represented by a seismic moment tensor is (Aki and Richards, 2002)

$$u_n(\mathbf{x}, t) = M_{pq}(t) * G_{np,q}(\mathbf{x}, t). \quad (3.1)$$

In this equation subscripts correspond to the three Cartesian components and a subscript after a comma is a derivative with respect to the corresponding component. $u_n(\mathbf{x}, t)$ is the n^{th} component of ground displacement and M_{pq} is the 3-by-3 seismic moment tensor. $G_{np,q}(\mathbf{x}, t)$ represents the n^{th} component of the ground displacement at location \mathbf{x} and time t in response to a force impulse in direction p . The symbol $*$ indicates a time convolution. Assuming that the time dependence of $M_{pq}(t)$ can be written as a product of a constant tensor M_{pq} and a source time function $s(t)$, we can replace the convolution by a product and replace the term $G_{np,q}(\mathbf{x}, t)$ by its convolution with $s(t)$, labelled as $\bar{G}_{np,q}(\mathbf{x}, t)$. Mapping the index pairs (p, q) into a single index i running from 1 to 9 gives the following expression:

$$u_n(\mathbf{x}, t) = \bar{G}_{ni}(\mathbf{x}, t) \times M_i \quad (3.2)$$

As the seismic moment tensor is symmetric, only M_1, M_2, \dots, M_6 are unique. The terms $\bar{G}_{ni}(\mathbf{x}, t)$ represent the elastic response to vector dipoles (single seismic moment tensor elements), and we will henceforth refer to them as 'Green's Functions'. Equation 3.2 poses a linear inverse problem, which we invert for M_i in two ways: First, using least squares, which gives the unconstrained moment tensor and, second, using a grid search over tensile crack moment tensors. We call the two schemes full and tensile crack moment tensor inversion, respectively. The full moment tensor inversion is unconstrained and has six degrees of freedom, corresponding to the six vector dipoles. The tensile crack moment tensor inversion has three degrees of freedom, corresponding to the strike and dip of the fault planes and the moment equivalent. The latter technique corresponds to the tensile crack + double-couple grid search employed by Minson et al. (2007) and Walter et al. (2009) with a vanishing double-couple component. When constraining the moment tensor to represent a tensile crack opening we assume a Poisson's ratio of 0.36. This is the same value used by Walter et al. (2009) to invert the seismograms of near-surface and intermediate-depth event. A different choice for the Poisson's ratio alters the relative strength of the isotropic and CLVD components, which decompose a tensile crack moment tensor (Walter et al., 2009).

3.4.2 3D Moment Tensor Inversion

The inversion scheme given in Equation 3.2 differs from the formulation outlined in Jost and Herrmann (1989), which uses fundamental faults rather than vector dipoles as Green's Functions. Their method has been used in deviatoric moment tensor inversions (Dreger, 2003). For full moment tensor inversions, a recently corrected form of the equations given in Jost and Herrmann (1989) has been successfully applied to earthquakes with a substantial isotropic component (Minson and Dreger, 2008; Minson et al., 2007).

The advantage of fundamental faults is that only one set of the 8 synthetic time series has to be generated for a given source-receiver distance. A linear superposition of fundamental faults can then be used to obtain the elastic response to any moment tensor source at any given azimuth. The benefit of this azimuthal independence is lost if the seismic velocity model is not azimuthally symmetric. This is the case for the present study site, where the glacier bed exhibits a 3D topography. For such 3D velocity models, fundamental fault Green's Functions would have to be generated at each recording station. For the present study, we use vector dipoles instead of fundamental faults. This corresponds to the inversion scheme of Equation 3.2. The 3D structure of the velocity model requires the calculation of 18 time series (three components for each of the six vector dipoles) at all recording station locations. It should be mentioned that reciprocity can reduce the computational expenditure when generating 3D synthetics for sources and receivers distributed over larger regions of the seismic velocity model. However, in the present case we focused on only a few source hypocenters and one seismic array, and we therefore did not employ reciprocity in the generation of Green's Functions.

The 3D synthetics were generated using the finite difference code `fd3d` (Olsen, 1994). The velocity model was discretized in a $264 \times 192 \times 220$ grid, and at the edges an absorbing boundary condition was applied over a thickness of 20 grid points. In all directions the distance between gridpoints was 2 m. The glacier surface was assumed flat, an assumption which in Walter et al. (2009) gave good results for moment tensor inversions of icequakes at shallow and intermediate depths. As a source-time function we used a Müller-Brüstle Function (Brüstle and Müller, 1983) with a duration of 0.02 seconds. Measured seismograms and Green's Function synthetics were filtered between 20 Hz and 70 Hz.

We focused on Green's Functions for four types of seismic velocity models, which are specified in Table 3.1. Model GRANITE3D consists of homogeneous ice resting on bedrock, whose topography was derived from the radio-echo soundings described previously in Section 3.2. The same bed topography was used to generate the model TILL3D. However, for this model we placed an intermediate low-velocity layer between the ice and bedrock. Model GRANITE1D is similar to model GRANITE3D, except that the interface is a horizontal plane. Model HOMOOG is a homogeneous half space of ice. These four models represent four degrees of complexity. The homogeneous half space is the simplest seismic velocity model of a glacier consisting of homogeneous ice and a free surface, only. TILL3D is the most complex model considered, because it includes the bed's 3D topography and some material properties of the ice-bedrock interface. In this sense, the GRANITE1D and GRANITE3D models are cases of intermediate complexity. The former introduces a glacier bed, to which the latter adds a 3D topography.

Error bars of hypocentral locations of the basal icequakes are ~ 10 m (Walter et al, 2008). For the bed elevation, the uncertainties can be as high as 10 % of the ice thickness

Table 3.1: Specifications of seismic velocity models used in the present study. In the GRANITE3D and TILL3D models the topography of the glacier bed was derived from radio-echo soundings. The source was placed at 156 m depth. Layer interfaces with a 3D topography are marked with a *. In this case, the given layer thickness corresponds to the epicentral location.

Model Name	Thickness m	v_p m/s	v_s m/s	ρ kg/m^3
HOMOG	∞	3630	1790	917
GRANITE1D				
Layer 1	162	3630	1790	917
Layer 2	∞	5000	2550	2750
GRANITE3D				
Layer 1	162*	3630	1790	917
Layer 2	∞	5000	2550	2750
TILL3D				
Layer 1	160*	3630	1790	917
Layer 2	4*	2500	1200	1500
Layer 3	∞	5000	2700	2750

(Sugiyama et al. 2008). At the epicentral location of the basal icequake cluster the radio-echo soundings determined a glacier thickness of 175 m. In order to satisfy the condition that between 20 Hz and 70 Hz the basal reflections are part of the direct arrivals, we placed the bed 6 m beneath the source. This was done by adding an offset of 13 m to the glacier bed, which lies within uncertainties.

We note that those velocity models accounting for the glacier bed (GRANITE1D, GRANITE3D AND TILL3D) drastically simplify the ice-bedrock interface. The presence of pervasive eroded material, basal crevassing, highly damaged ice or pockets of accumulated melt water can significantly complicate the wave field. Introducing a slow seismic velocity layer in the TILL3D model is a rather rough approximation to the complicated velocity structure which may be present if the glacier does not rest on bedrock directly. Using 1D waveform modelling we noticed that if present, a slow velocity layer has to be thin (~ 4 m). At the frequency band of interest, this intermediate layer otherwise leads to synthetics that no longer have the relatively simple waveforms consisting of only P- and S-phases.

3.5 Sensitivity to Velocity Model

As previously described the waveforms shown in Figure 3.3 suggest that the source is close enough to the glacier bed that the basal reflections amplify the direct P- and S-waves. As the GRANITE3D and TILL3D models contain merely an approximation to the true basal topography and the ice-bedrock interface, the Green's Functions calculated with these models may not accurately reproduce the observed basal reflections. Therefore, we need to investigate how sensitive the moment tensor inversion is to errors in the Green's Functions, which arise from inaccuracies of the modelled reflections and errors in the velocity profile in general.

We investigate how well the signals of a seismic source close to the ice-bedrock interface can be inverted using Green's Functions of a wrong velocity model. Synthetic seis-

mograms are calculated for a source placed 6 m above the glacier bed in the GRANITE1D and the GRANITE3D model and 4 m above the 4 m thick low velocity layer in the TILL3D model. The GRANITE1D synthetics are inverted using Green's Functions computed with the HOMOOG model. The GRANITE3D synthetics are inverted with HOMOOG and GRANITE1D Green's Functions. Finally, we invert the TILL3D synthetics with GRANITE3D Green's Functions. In all cases, we use the same source-station geometry as for the basal cluster.

The sensitivity tests were performed for two end-marker types of sources: a tensile crack and a pure double-couple fracture. We varied the strike and dip of the fault planes in increments of 10° . For the double-couple source the rake was fixed to 90° . The inversions in the sensitivity tests were performed automatically and the waveforms fits were not visually inspected for each inversion run. The overall variance reduction was calculated using the median of the variance reductions of the individual stations. This is unconventional, as usually the arithmetic mean is used. However, the arithmetic mean is more susceptible to outliers, such as individual stations with extremely low fit quality. As we did not manually or automatically remove such stations in the sensitivity studies, we calculated the overall variance reduction with the median to reduce the impact that a single station has on the overall variance reduction. When inverting data seismograms, however, we conformed to the convention of using the arithmetic mean.

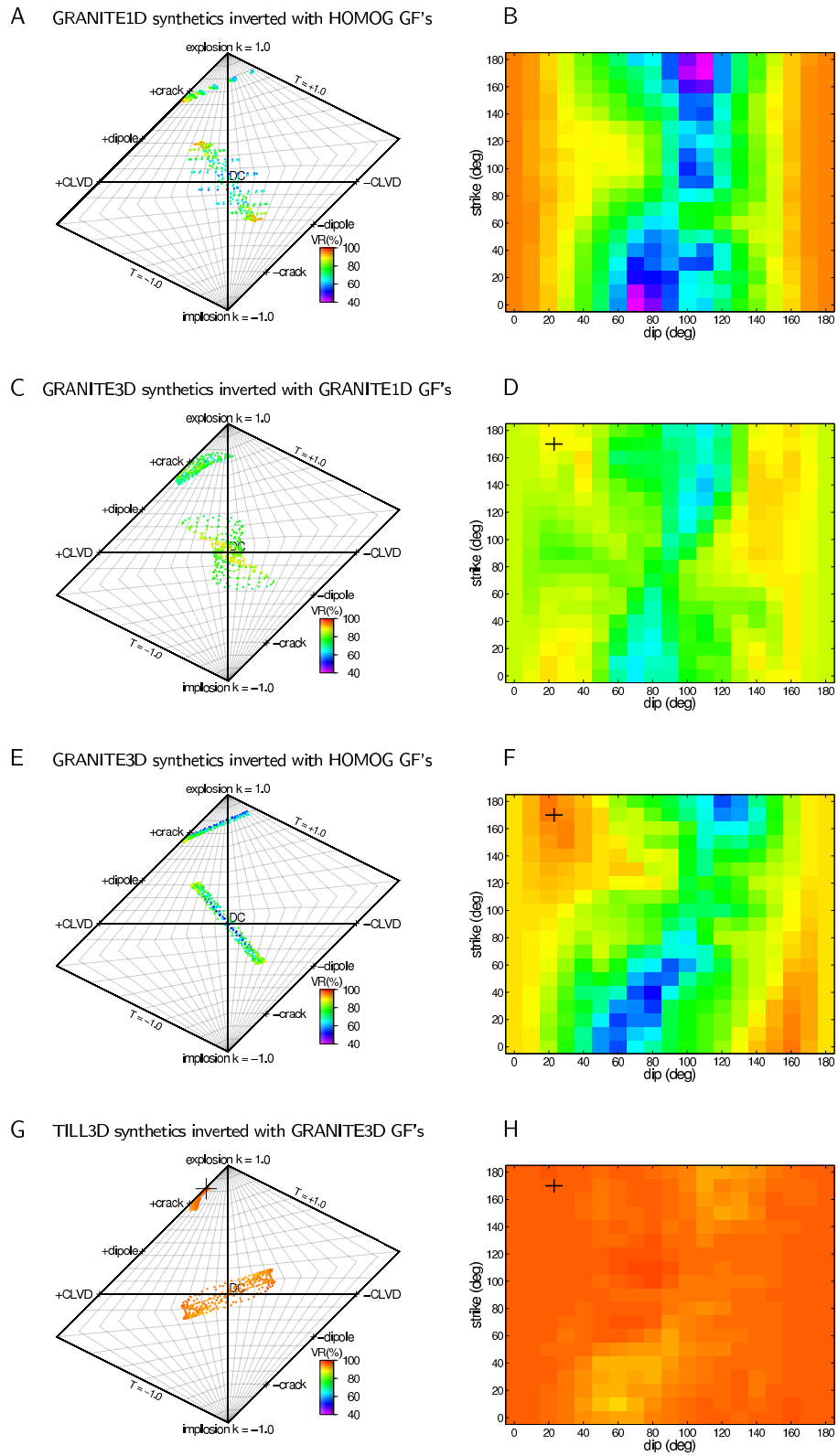


Figure 3.5:

Figure 3.5 (previous page): Results of sensitivity studies of the full moment tensor inversion: Source-type plots of inversion results of tensile crack and double-couple synthetics (left) and variance reductions for the tensile crack synthetics (right). A and B: Synthetic sources in the GRANITE1D model inverted with HOMOOG Green's Functions. C and D: Synthetic sources in the GRANITE3D model inverted with GRANITE1D Green's Functions. E and F: Synthetic sources in the GRANITE3D model inverted with HOMOOG Green's Functions. G and H: Synthetic sources in the TILL3D model inverted with GRANITE3D Green's Functions. In the source-type plots each dot is color-coded according to the variance reduction of the solution it represents. In all cases, the solutions separate into two populations corresponding to the inversions of tensile crack and double-couple synthetics. At the same time, large deviations from the true source type exist for some fault plane orientations. The fit quality depends on the orientation of the tensile crack fault planes. In case of the synthetic tensile crack in the GRANITE3D model, the highest fit quality is achieved for a strike and dip value similar to the orientation of the glacier bed near the source, as indicated by the black cross hairs. Notice that using HOMOOG Green's Functions provides variance reductions of up to 94 % when inverting GRANITE1D and GRANITE3D synthetic tensile cracks. In the latter case, the HOMOOG Green's Functions can even perform better than the GRANITE1D Green's Functions, although large deviations from the correct source-type occur. For all fault plane mechanisms, GRANITE3D Green's Functions can invert TILL3D synthetics with high fit qualities (Panels G and H). The variance reductions lie between 90 % and 96.5 %. The large cross hairs in panel G correspond to the inversion of the tensile crack source with bed-parallel fault planes.

Figure 3.5A, C, E and G show the source-type plots (Hudson et al., 1989) of the sensitivity studies. Each dot corresponds to a fault with a different strike and dip. For all cases we notice that the inversion results separate into two populations, which are located in distinct regions of the grid according to whether the synthetic source is a tensile crack or a double-couple. This indicates that the inversion results correctly distinguish between a tensile crack and a double-couple source, even though the Green's Functions model basal reflections incorrectly or not at all.

In most cases, the fit quality of the synthetic tensile cracks depends on the strike and dip (Figure 3.5B, D, and F) of the fault planes. In the case of the GRANITE1D synthetic tensile cracks inverted with HOMOGENEOUS Green's Functions (Figure 3.5B) there is a strong dependence on dip, and best results are achieved for near-horizontal fault planes. Variance reductions lie between 41 % and 94 %. There is a weaker dependence on the strike. This dependence is due to the station distribution as this is the only source of azimuthal variation for the generation of GRANITE1D synthetics.

Inverting GRANITE3D tensile crack synthetics with GRANITE1D Green's Functions (Figure 3.5D) gives variance reductions between 61% and 90%. Somewhat surprisingly, Figure 3.5F shows that inverting GRANITE3D tensile crack synthetics with HOMOGENEOUS Green's Functions can give slightly better results than inversions with GRANITE1D Green's Functions. However, this depends on the fault plane orientation of the tensile crack. Figure 3.5F shows that best results can be achieved for near-horizontal fault planes with strikes running approximately North-South. This coincides with the orientation of the bed of the GRANITE3D model in the vicinity of the synthetic source (black cross hairs in Figure 3.5D, F and H). A reason why HOMOGENEOUS Green's Functions perform better at specific fault plane orientations than GRANITE1D Green's Functions may be found in small later arrivals, such as multiples or head waves. These are missing in the HOMOGENEOUS synthetics whereas they are present in the GRANITE1D synthetics. However, in the latter case, the secondary arrivals may have phases and amplitudes, which are different from the secondary arrivals in the GRANITE3D synthetics. Modelling secondary arrivals incorrectly with GRANITE1D Green's Function may thus have a more negative effect on the variance reduction than not modelling them at all, as in the case of the HOMOGENEOUS Green's Functions.

The sensitivity tests thus show that Green's Functions of a homogeneous half space can model waveforms whose direct P- and S-wave trains were modified by reflections of an adjacent glacier bed. This holds for an inclined bed as in the GRANITE3D model as well as for a horizontal one as in the GRANITE1D model.

When using GRANITE3D Green's Functions to invert tensile crack synthetics of the TILL3D model, the variance reduction is high ($> 90\%$) for all fault plane orientations (Figure 3.5H). This suggests that omitting the thin basal low-velocity layer in the generation of Green's Functions affects the inversion quality only marginally. However, the results for the double-couple can acquire a substantial CLVD component (Figure 3.5G). For the tensile crack with bed-parallel fault planes, the omission of the low-velocity layer leads to an artificial increase in isotropy, as indicated by the large cross in Figure 3.5G.

So far we have performed sensitivity tests for the full moment tensor inversion, only. Concerning the tensile crack moment tensor inversion, we now test how accurately the fault plane orientations of a synthetic basal tensile crack can be recovered with Green's Functions of an incorrect medium. We focus on three cases: TILL3D synthetics inverted with

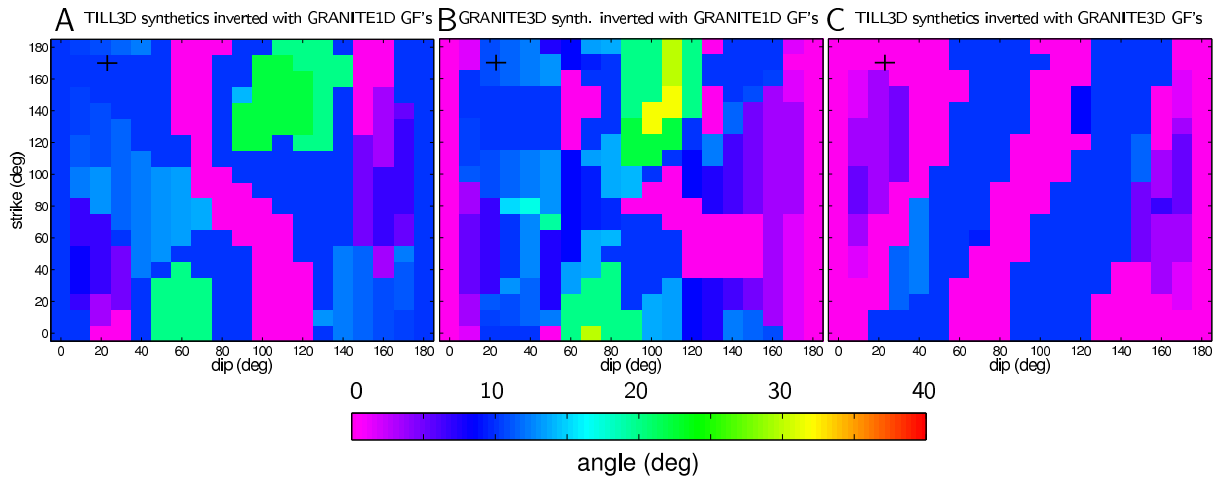


Figure 3.6: Results of sensitivity studies of the tensile crack moment tensor inversion. Shown is the angle that the inverted tensile crack fault planes make with the fault plane orientation calculated with the tensile crack moment tensor inversion. Note that this angle is never larger than 32° . For the TILL3D synthetics inverted with GRANITE3D Green's Functions the results agree to within 12% for all fault plane orientations. Disagreement usually occurs at near-vertical fault plane orientations, whereas near-horizontal fault plane orientations give good agreement. This resembles the performance of the full moment tensor inversion as shown in Figure 3.5.

GRANITE1D Green's Functions, GRANITE3D synthetics inverted with GRANITE1D Greens Functions and TILL3D synthetics inverted with GRANITE3D Green's Functions. As before we vary the orientation of the fault planes. This time, however, we use the tensile crack moment tensor inversion. Saving computational time, we search strike and dip in increments of 10° and we search over 20 different moment magnitudes. We then calculate the angle between the tensile crack fault planes of the forward synthetics and the tensile crack fault planes as determined by the inversion.

Figure 3.6 shows the results of these sensitivity studies. In most cases the fit results agree with the initial fault plane orientations to within 20° . In the case of the TILL3D synthetics inverted with GRANITE3D synthetics the mismatch is 10° or smaller for all fault plane orientations (panel C). Only for the GRANITE3D sources inverted with GRANITE1D (panel B) there is a mismatch of up to 32° . The individual fit results show that in this case the recovered fault plane orientations are still vertical. Yet there can be a considerable mismatch, because the fitted fault planes dip in the opposite direction as fault planes of the forward synthetics. For this inversion as well as the TILL3D synthetics inverted with GRANITE1D Green's Functions (panel A) the largest mismatches occur predominantly for near-vertical fault planes with strikes above 110° or below 30° . GRANITE1D inversions of TILL3D synthetics recover horizontal fault planes to within 10° (panel A). In the other cases, near-horizontal fault planes are recovered exactly. The sensitivity studies thus indicate that the ability of the tensile crack moment tensor inversion to recover fault plane orientations is rather robust with respect to the basal topography and material. Specifically, most tensile crack fault plane orientations can be recovered to within 20° with inversions using Green's Functions calculated for a horizontal bed. The results furthermore suggest that ignoring a low velocity layer near the glacier base does not influence the calculation of fault plane orientations substantially.

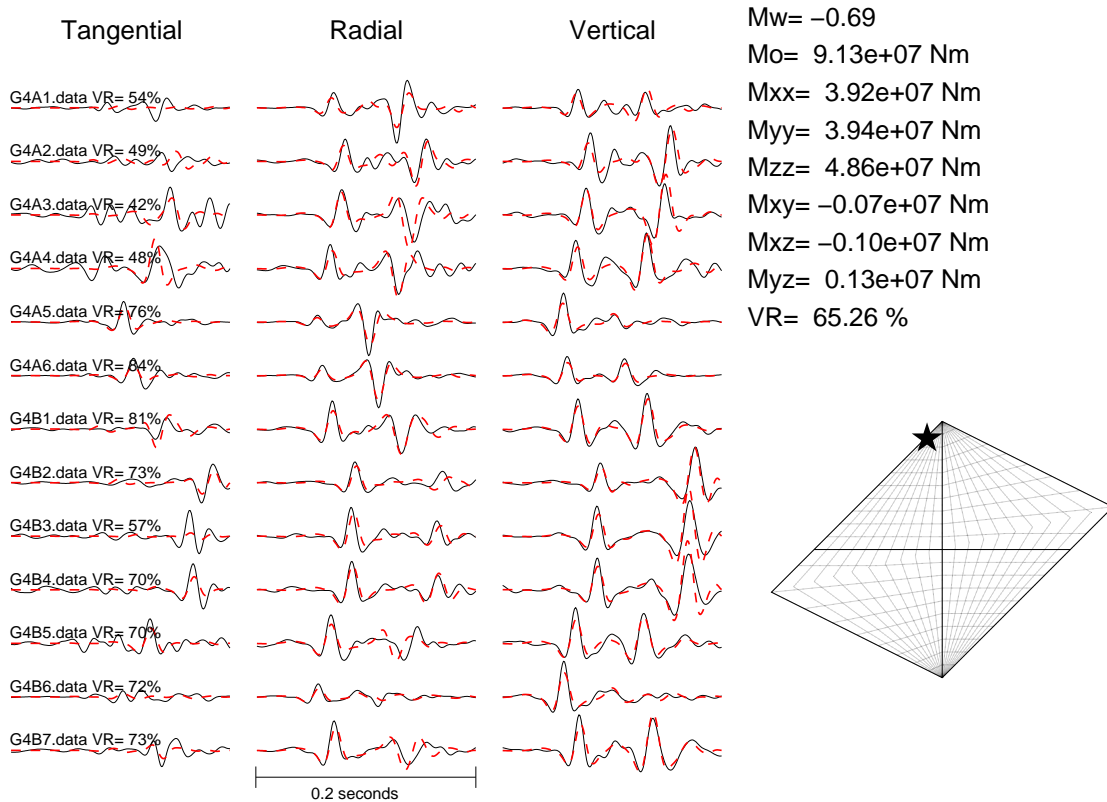


Figure 3.7: Waveform fits of the full moment tensor inversion of the basal event that occurred on June 16 at 05:58:12. The black solid line and the red dashed line represent data and synthetic fit, respectively. Green's Functions were generated using the TILL3D seismic velocity model. Note that the determined source type is highly isotropic.

3.6 Results of Full Moment Tensor Inversion

Seismic events of the basal cluster were recorded between June 15 and July 1, 2004. We inverted 14 out of 28 seismograms using TILL3D, GRANITE3D, GRANITE1D and HOMO-G Green's Functions. Events recorded between June 25 and 29 were not analyzed, because only 7 of the 14 seismometers were operational during this time period. Furthermore, 4 events which yielded very low fit qualities were excluded from the analysis. The seismogram of one event was not inverted as it contains a double event. In the GRANITE3D and TILL3D inversion we varied source depth and velocity of the glacier bed through trial and error to increase the fit quality of the June 16 event, which has particularly clean signals. The values given in Table 3.1 correspond to the best solution and were used for all events. The computational power required for the finite difference code generating the 3D Green's Functions did not allow for systematic grid searches over these parameters.

Waveform fits for all analyzed events were visually inspected and where necessary synthetics were time shifted against the data to increase the variance reduction. This was done by manually adjusting the z_{corr} value (Walter et al., 2009). As bed reflections change the shape of the first arrivals, z_{corr} values were not the same for inversions with different Green's Functions. Note that the Green's Functions were calculated without a reduction

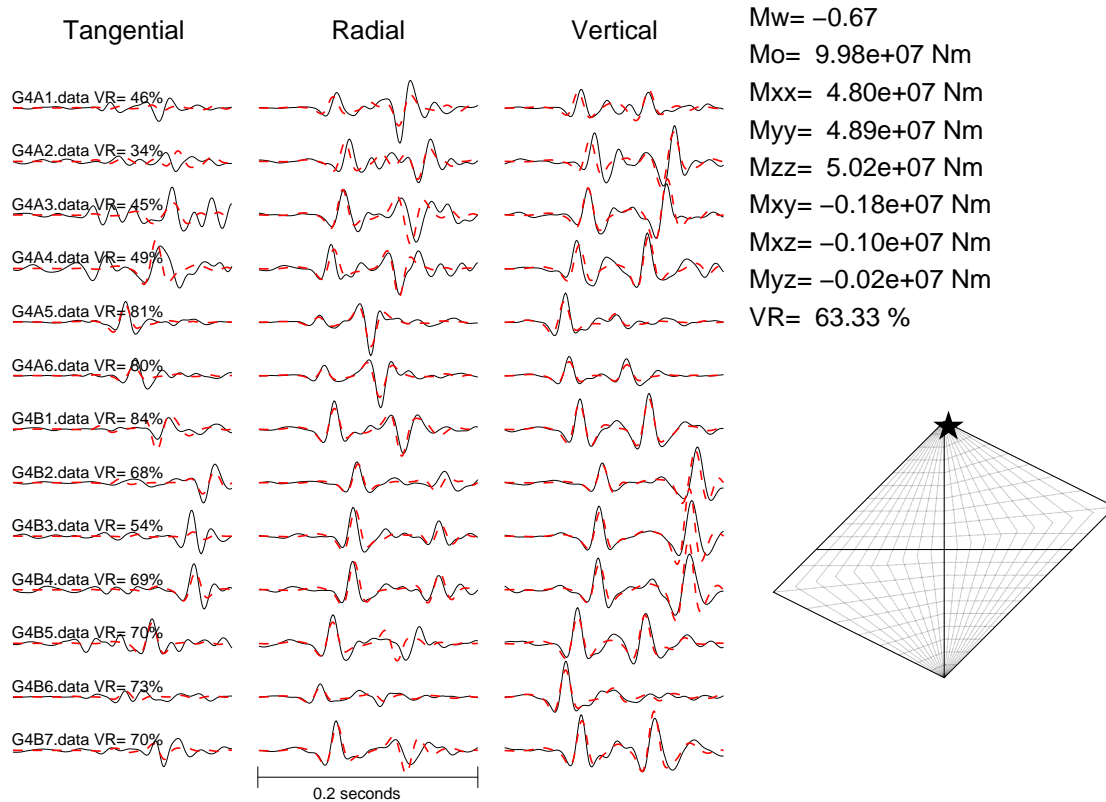


Figure 3.8: Waveform fits of the full moment tensor inversion of the same event shown in Figure 3.7, however this time using GRANITE3D Green's Functions. The black solid line and the red dashed line represent data and synthetic fit, respectively. Note that the determined source type is highly isotropic and closer to a pure explosion than in the TILL3D inversion (Figure 3.7).

velocity. Hence, the $zcorr$ values are not proportional to the source-receiver distances.

Figure 3.7 shows the waveform fits of the June 16 event using the full moment tensor inversion with TILL3D Green's Functions. The fit reproduces most phases well giving a variance reduction of 65.3%. Misfit occurs mainly on the tangential component. The source-type plot indicates a large isotropic component, which is strong evidence that this event is a tensile crack opening and not a shear dislocation. Using GRANITE3D Green's Functions, the variance reduction decreases by only two percent (Figure 3.8). The source type is again highly isotropic and somewhat closer to a pure explosion.

The results of all full moment tensor inversions are summarized in Table 3.2. Variance reductions for inversions with TILL3D Green's Functions are usually highest lying between 43% and 65%. For most events the variance reduction only decreases by one or two percent when GRANITE3D Green's Functions are used. However, the fit quality decreases by around 10% when using GRANITE1D Green's Functions. On the other hand, HOMOOG Green's Functions allow for fit qualities comparable to the TILL3D and GRANITE3D Green's Functions. In fact, some events exhibit best fit qualities with HOMOOG Green's Functions.

Figure 3.9 gives a summary of the source types determined with the full moment tensor inversions using the four sets of Green's Functions. In all cases the source mechanisms

Table 3.2: Variance reductions of full moment tensor inversions using Green's Functions of the TILL3D, GRANITE3D, GRANITE1D and HOMOG seismic velocity models. Notice that for most events the TILL3D Green's Functions achieve the highest fit qualities. However, for several cases the HOMOG Green's Functions yield better fit results. Nonetheless, TILL3D, GRANITE3D and HOMOG Green's Functions achieve similar fit qualities when compared to the GRANITE1D inversion results.

Source Time	VR (%) TILL3D	VR (%) GRANITE3D	VR (%) GRANITE1D	VR (%) HOMOG
Jun 15 04:41:16	61.8	60.5	48.4	60.8
Jun 16 05:58:12	65.3	63.3	50.9	60.6
Jun 17 04:44:23	61.7	60.7	49.2	60.3
Jun 17 07:41:54	58.9	58.1	50.1	59.0
Jun 19 07:46:25	63.1	61.1	49.8	55.1
Jun 19 07:46:26	55.7	54.9	45.6	53.3
Jun 20 01:51:57	52.3	52.3	41.6	52.9
Jun 22 22:39:23	42.7	42.1	29.9	43.1
Jun 24 04:39:14	51.8	48.8	39.0	45.2
Jun 30 04:15:54	51.9	50.7	39.2	51.0
Jul 01 04:29:22	50.2	48.6	36.6	46.1
Jul 01 05:50:43	51.0	48.2	38.5	39.0
Jul 01 06:17:55	42.8	42.8	32.7	42.3
Jul 01 07:58:43	53.2	54.8	44.6	59.6

have a stronger isotropic component than a tensile crack with a Poisson's ratio of 0.36, as used in the present work. The highly isotropic components may be explained by explosive sources. However, we do not pursue this interpretation further as we consider explosions as natural seismic sources in glacier ice unlikely. The most plausible fault mechanism with a similarly high isotropic component is a tensile crack. In this view, the exceedingly high isotropic degrees determined by the full moment tensor inversions are due to errors in the Green's Functions, which we analyze at this point.

Compared to the TILL3D and HOMOG inversions, the GRANITE3D inversions determine a particularly large isotropic component (Figure 3.9). Some mechanisms are practically explosions. As a pure explosion does not produce any S-waves, the dominating SV-waves in the GRANITE3D fit (Figure 3.8) contain a large amount of basal P to SV conversions. The HOMOG Green's Functions, on the other hand, do not contain any basal reflections. The waveform fits of the SV waves are thus purely direct waves. Consequently, the determined source mechanism is less isotropic, as it has to produce S-energy, which in the case of the GRANITE3D inversion is compensated for by basal P to SV conversions. All but one of the TILL3D inversions determine source types, with isotropy comparable to the results of the HOMOG inversions. The basal reflections and conversions amplify the P and S-phases in a way that a less isotropic source is required than in the GRANITE3D inversion. On the contrary, the basal reflections and conversions in the GRANITE3D model amplify the SV-wavelet more than the P-wavelet, causing the moment tensor inversion to suppress the generation of direct S-waves thus leading to a stronger isotropic component. Neither the HOMOG nor the TILL3D inversions recover a pure tensile crack mechanism. This is likely due to the material properties of the glacier bed, which none of the four models completely captures. In both inversions, however, the mechanisms are closer to a tensile crack than in the GRANITE3D inversion. This being said, we do acknowledge that the assumed Poisson's ratio of 0.36 may be inaccurate. A

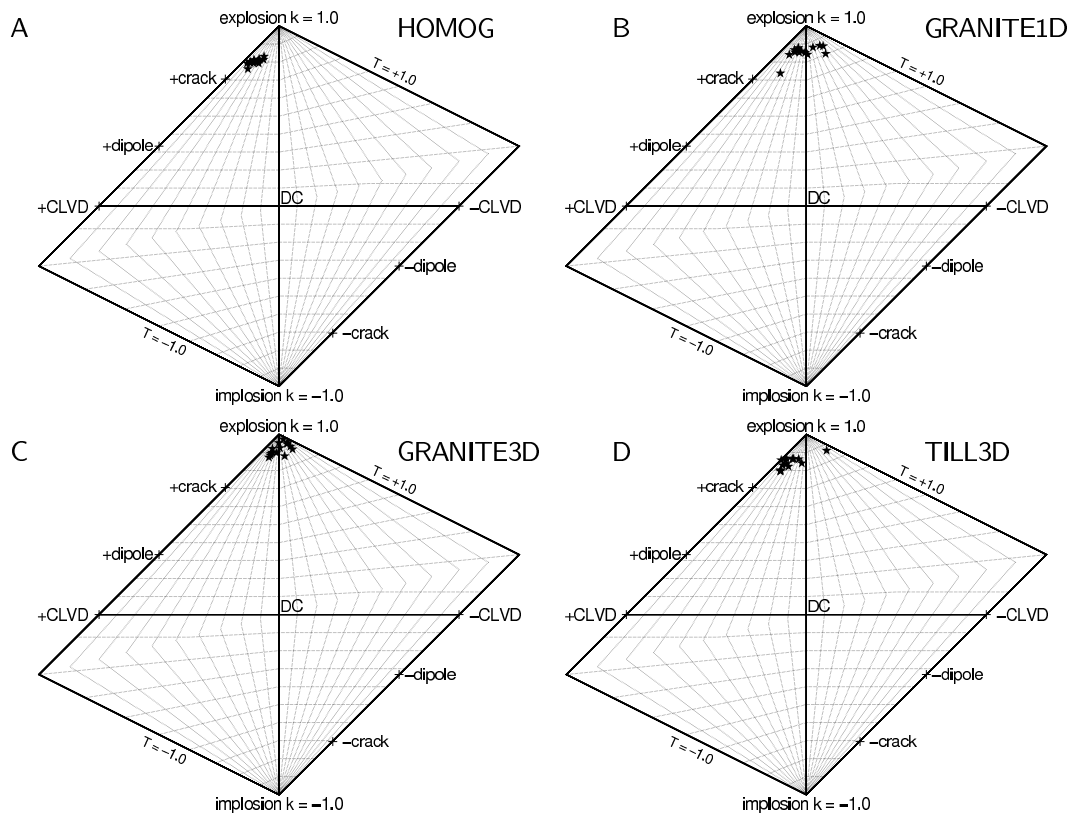


Figure 3.9: Source type plots of full moment tensor inversions of the data using HOMOG (A), GRANITE1D (B), GRANITE3D (C) and TILL3D (D) Green's Functions. In all cases a large isotropic component is recovered. Note that for the GRANITE3D inversions the source types are very close to pure explosions. Both HOMOG and TILL3D Green's Functions provide a lower degree of isotropy. .

Table 3.3: Variance reductions of full and tensile crack moment tensor inversions using Green's Functions of the TILL3D and GRANITE3D seismic velocity model. The decrease in variance reduction (number in parenthesis) when constraining the moment tensor to represent a tensile crack is larger for the GRANITE3D inversion. This confirms the source-type plots shown in Figure 3.9, which show that the results of the TILL3D inversion are closer to a tensile crack than the results of the GRANITE3D inversion. The strike and dip values are calculated with the tensile crack moment tensor inversion.

Source Time	TILL3D				GRANITE3D			
	VR Full (%)	VR Crack (%)	strike (°)	dip (°)	VR Full (%)	VR Crack (%)	strike (°)	dip (°)
Jun 15 04:41:16	61.8	59.0 (-2.8)	200	14	60.5	57.4 (-3.1)	188	20
Jun 16 05:58:12	65.3	60.4 (-4.9)	192	14	63.3	56.3 (-7.0)	190	24
Jun 17 04:44:23	61.7	58.2 (-3.5)	184	14	60.7	56.5 (-4.2)	184	22
Jun 17 07:41:54	58.9	55.5 (-3.4)	186	18	58.1	51.9 (-6.2)	186	28
Jun 19 07:46:25	63.1	57.0 (-6.1)	240	14	61.1	51.9 (-9.2)	216	22
Jun 19 07:46:26	55.7	51.9 (-3.8)	188	20	54.9	48.7 (-6.2)	198	26
Jun 20 01:51:57	52.3	48.1 (-4.2)	186	18	52.3	46.8 (-5.5)	182	26
Jun 22 22:39:23	42.7	40.6 (-2.1)	8	0	42.1	38.2 (-3.9)	170	16
Jun 24 04:39:14	51.8	48.6 (-3.2)	92	10	48.8	42.5 (-6.3)	152	14
Jun 30 04:15:54	51.9	48.4 (-3.5)	30	8	50.7	44.9 (-5.8)	150	10
Jul 01 04:29:22	50.2	47.7 (-2.5)	242	18	48.6	44.9 (-3.7)	226	22
Jul 01 05:50:43	51.0	42.2 (-8.8)	250	18	48.2	36.7 (-11.5)	312	58
Jul 01 06:17:55	42.8	42.1 (-0.7)	74	18	42.8	39.0 (-3.8)	106	16
Jul 01 07:58:43	53.2	52.0 (-1.2)	226	20	54.8	52.4 (-2.4)	218	24

higher Poisson's ratio would move the pure tensile crack mechanism closer to the HOMOOG and TILL3D inversion results. In general, compared to the GRANITE3D model, the HOMOOG and TILL3D Green's Functions move the mechanisms in the direction of a tensile crack. This is a more realistic source type than an explosion as suggested by the GRANITE3D inversions. However, as a homogeneous half space is unrealistic for a finite glacier we choose TILL3D as our favorite model.

We conclude that whereas all presented inversions determine highly isotropic moment tensors we favor the TILL3D model for a variety of reasons: First, the fit qualities tend to be highest. Second, the source mechanisms are closer to a tensile crack than the source mechanisms determined by the GRANITE3D inversions. Third, the TILL3D model is more realistic than the HOMOOG model, as it contains the basal topography determined by radio-echo soundings.

3.7 Results of Tensile Crack Moment Tensor Inversion

Using the TILL3D and GRANITE3D Green's Functions we inverted for a tensile crack moment tensor. The grid search was first performed using 20° increments for the strike and dip, and subsequently the increments were refined to 2° around the values giving the best variance reduction. Table 3.3 shows the variance reductions and fault plane orientations determined by the tensile crack moment tensor inversion. The variance reductions are systematically lower than the values of the full moment tensor inversion. The decrease in variance reduction from the unconstrained full moment tensor inversion to the constrained tensile crack moment tensor solution is smaller for the TILL3D Green's

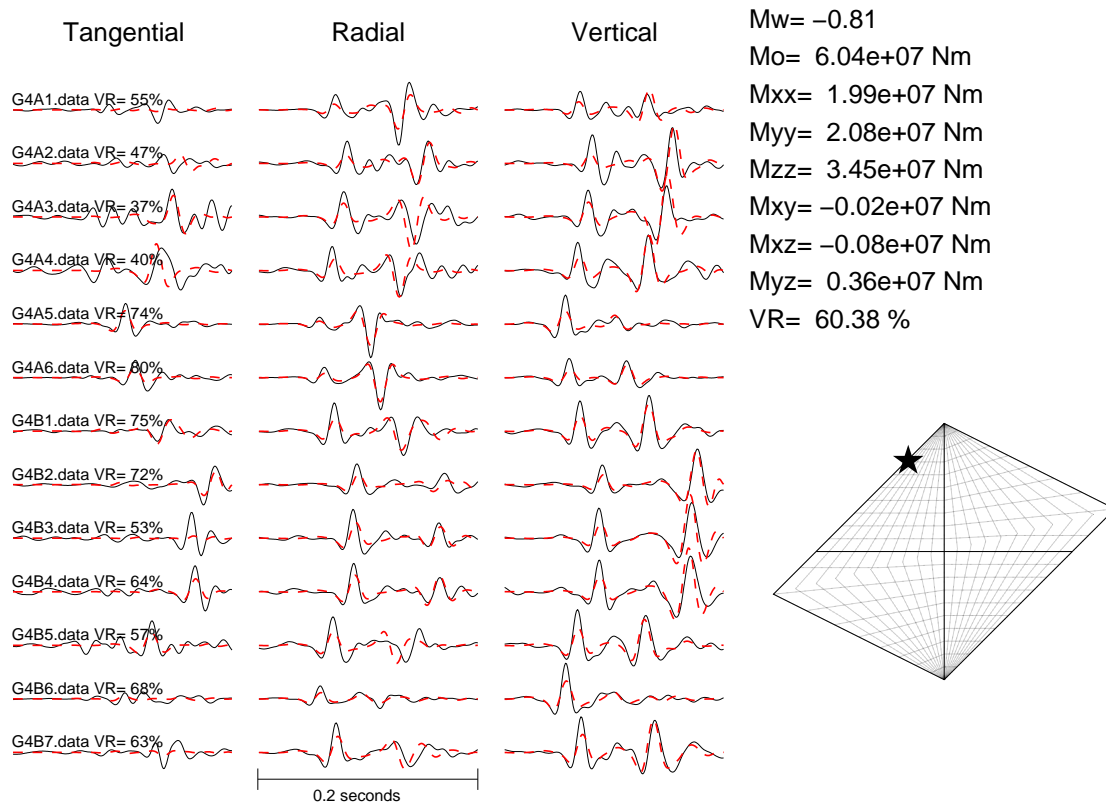


Figure 3.10: Waveform fits of the tensile crack moment tensor inversion of the same event shown in Figure 3.7. The black solid line and the red dashed line represent data and synthetic fit, respectively. Green's Functions were generated using the TILL3D seismic velocity model. Compared to the full moment tensor inversion, the variance reduction is about 5 % lower.

Function than for the GRANITE3D Green's Function (numbers in parenthesis). The explanation can be found in the degree of isotropy of the source mechanisms determined with the full moment tensor inversion. As the TILL3D inversion results lie closer to the tensile crack mechanism than the GRANITE3D results, less fit quality is sacrificed when constraining the moment tensors to tensile crack mechanisms.

Figure 3.10 shows the tensile crack moment tensor inversion with TILL3D Green's Functions for the June 16 event, whose full moment tensor inversion is shown in Figure 3.7. The fit does not reproduce the impulsive P-waves as well as the full moment tensor inversion. The source-type plot of the latter (Figure 3.7) suggests that a higher degree of isotropy is required to fit the impulsive P-phases. In other words, the isotropic part of the tensile crack moment tensor is not adequate to reproduce the impulsive P-phases. Apparently, a full moment tensor can reproduce the impulsive P-phases, because its isotropic moment is not constrained. In order to reconcile this observation with a tensile crack, we suggest that the basal reflections do not amplify the P-phase enough relative to the S-phase. Most likely the three layer TILL3D model does not capture details of the glacier bed. Although we tried different values for the thickness and seismic velocity of the intermediate layer as well as for the velocity of the glacier bed, we cannot guarantee that we found the optimal values. Furthermore, a single intermediate layer may not correctly represent a combination of eroded material, water and damaged ice. The true basal condi-

tions apparently produce relative amplitudes of P- and S-reflections, which cannot entirely be modelled using a single intermediate layer as in the TILL3D model. We therefore conclude that the lower fit qualities of the tensile crack inversion as well as the overestimation of the isotropic moment of the full moment tensor inversion are due to an oversimplified velocity model rather than a true explosive source.

The dip values determined by the TILL3D tensile crack inversions lie between 10° and 20° (Table 3.3) indicating near-horizontal fault planes. For about half of the events the strike values lie between 180° and 200° , which means that the fault planes dip towards West. The remaining events have largely varying strike values. At rather small dip values it may be difficult to calculate reliable strike values with the tensile crack moment tensor inversion. In the extreme case of 0° dip the strike is actually undefined. Thus, we suggest that the large strike variation of about half of the events may not be physical but rather due to numerical instabilities in the inversion of near-horizontal tensile cracks. The tendency of these events to have lower variance reductions supports this interpretation.

To check the robustness of these results, we also report the results of the tensile crack inversions using the GRANITE3D Green's Functions (Table 3.3). The values are similar although there is less variation in strike. Furthermore, we performed the tensile crack moment tensor inversion of the June 16 event with Green's Functions of a horizontal bed (GRANITE1D model) and a homogeneous half space (HOMOG model). For the former case the variance reduction drops by 14 % with respect to the TILL3D inversion, and the strike and dip values are 184° and 32° , respectively. Using HOMOG Green's Functions, the variance reduction drops by only 5 %. Strike and dip are 182° and 24° , respectively. Near-horizontal fault planes that dip towards West thus seem a robust result for the tensile crack sources of the basal icequakes considered in this paper.

This result is furthermore consistent with qualitative characteristics of the waveforms. At station B6, most energy arrives in the P-phase (Figure 3.3). The meaning of this observation can be understood considering the azimuthal dependence of the radiation pattern of a circular tensile crack (e. g. Chouet 1979):

$$\begin{aligned} u^r &\sim \lambda/\mu + 2 \sin^2(\theta) \sin^2(\phi) \\ u^\phi &\sim \sin(\theta) \sin(2\phi) \\ u^\theta &\sim \sin(2\theta) \sin^2(\phi) \end{aligned} \quad (3.3)$$

These relations hold for a tensile crack opening in the vertical x-z plane. ϕ and θ are the azimuth and elevation angles, respectively. u^ϕ and u^θ are the corresponding components of the ground displacement. u^r denotes the ground displacement in the radial direction. λ and μ are the Lamé constants. The maximal amplitude of the P-radiation is proportional to u^r , whereas the respective maximal amplitudes of the SH- and SV-radiation are proportional to u^ϕ and u^θ . Note that the maximal amplitude of the P-wave is different from zero in all directions. On the other hand, no SH- or SV-energy is radiated at $(\phi, \theta) = (90^\circ, 90^\circ)$, the direction along which the tensile crack opens.

The lack of S-energy recorded at station B6 has two implications: First, the source does not emit S-waves in the direction of B6. Second, no basal S-reflections reach station B6. Both points can be explained by a tensile crack source whose fault planes are perpendicular to the line that connects it with station B6 and parallel to the glacier bed. Such a source does not emit S-energy towards B6. Furthermore, the basal reflections towards B6 are normal to the bed, which means that no S-wave reaches the reflection point and

no P-energy is converted to S-energy upon reflection. Considering the source-station geometry, we can thus estimate the fault plane orientation. For the cluster events, the angle between the line connecting source and station and the vertical axis is 20° . Furthermore, the epicenter lies east of station B6, suggesting that the fault planes dip towards West. We therefore conclude that the waveform characteristics are consistent with the quantitative results of the tensile crack moment tensor inversions (Table 3.3).

With the determined fault plane orientations we once again turn to the results of the sensitivity studies. In Figure 3.5G we showed the inversion results for a tensile crack in a TILL3D medium inverted with GRANITE3D Green's Functions. In the case of bed-parallel fault planes (cross hairs) the determined moment tensor has a stronger isotropic component than a tensile crack source. This is similar to the behaviour we observed for the inversion of the data: The GRANITE3D Green's Functions provided sources with higher isotropy than the TILL3D Green's Functions. The sensitivity studies presented in Figure 3.5G thus suggest that the large isotropic components determined in the GRANITE3D inversions of the data are the result of omitting the basal slow velocity layer. Therefore, we restate that a slow basal velocity layer is needed to improve the performance of the moment tensor inversion with respect to the two-layer GRANITE3D model.

Near-horizontal fault planes suggest that in addition to the tensile crack opening, the source may also undergo a shear dislocation due to the downhill motion of the glacier. This corresponds to the superposition of a tensile crack and a double-couple source, both of which share common fault planes (e. g. Minson et al., 2007). Therefore, we added a double-couple component to the tensile crack moment tensor inversion and repeated the grid search for the event shown in Figure 3.10. The variance reduction improved by less than 0.1 % and the determined double-couple component was 100 times smaller than the tensile crack component. Therefore, we conclude that the basal events do not have any significant double-couple component.

3.8 Discussion

Possibly the most profound result of the present study is that in order to model our basal icequakes, a highly isotropic moment tensor is necessary. The events are therefore not due to shear failure during stick-slip motion, but rather due to tensile crack openings, which is the mechanism also responsible for surface crevasse openings. Furthermore, considering the results of moment tensor inversions as well as qualitative waveform characteristics, we concluded that the tensile fault planes are near-horizontal.

Walter et al. (2008) suggested that basal icequakes beneath Gornergletscher are caused by large deformation rates that occur during variations of basal sliding, which can be induced by drastically varying basal water pressures. Near-horizontal fault planes indicate that during such water pressure variations the basal stress state is rather complicated. A reason for such fractures may be the closing of water-filled cavities at the glacier bed. When growing during increasing water pressures, such cavities enhance basal sliding. In the absence or during the rapid evacuation of water, the cavities quickly close (Iken, 1981). The ice above the closing cavity may deform quickly enough to fracture across near-horizontal fault planes.

In the calculation of synthetic seismograms we placed the source close enough to the ice-bedrock interface so that reflections are not distinct from first arrivals but amplify them, as suggested by the simple waveforms of the measured seismograms. When using Green's Functions of a two layer velocity model consisting of ice and bedrock, full moment tensor inversions indicate exceedingly strong isotropic components. Introducing an intermediate low velocity layer at the glacier bed tended to lower the isotropy of the source, although it remained too high for a tensile crack. Together with the good fit results obtained with such a three layer model, this suggests that a basal low-velocity layer is necessary to model the seismograms of our basal events. Although we cannot state with certainty which physical conditions exist near the glacier base, these results may reflect the presence of unconsolidated material such as glacial till. Despite the strong inclination of the glacier bed beneath the study site such material may accumulate at least locally in topographic depressions. Another explanation for the low velocity layer may be found in basal crevassing. Gischig (2007) showed that surface crevasses can locally decrease seismic velocities by more than 10%. A highly damaged basal ice layer can therefore be expected to have significantly lower seismic velocities.

The moment tensor inversions of the data as well as the sensitivity tests furthermore showed that a homogeneous half space can satisfactorily fit waveforms whose direct P- and S-wave amplitudes are altered by basal reflections. We concluded that this is inherent to the geometry of the problem, such as the proximity of the source to the ice-bedrock interface and the fault plane orientation. An alternative explanation for the success of the Green's Functions of the homogeneous half space to model basal icequakes may be that the ice-bedrock interface does not reflect significant amounts of P- and S-waves. We consider it possible that fissures, water lenses and eroded material may absorb large amounts of elastic energy and therefore suppress basal reflections. In this case, the Green's Functions of the homogeneous half space would be sufficient as no basal reflections would have to be modelled. However, as previously pointed out, we were not able to find a realistic combination of layered material producing only small amounts of P- and S-reflections that would be consistent with the waveforms shown in Figure 3.3, and therefore we do not favor this explanation.

The good inversion results attained with the Green's Functions of a homogeneous half space could also be explained by a bimaterial fracture occurring exactly at the ice-bedrock interface. In this case, seismic energy is emitted into the glacier ice as well as into the bedrock, but none is reflected. Such a model is supported by the fault plane orientation, which is roughly parallel to the glacier bed. However, such bimaterial tensile fractures would be expected during increasing water pressures, when the glacier may separate from the bed, and not during low or decreasing water pressures, which was the case during the occurrence of basal icequakes (Walter et al. 2008). Therefore, we find a source within the ice more likely than a bimaterial rupture at the ice-bedrock interface.

In order to achieve good waveform fits, 3D Green's Functions had to be used in the moment tensor inversions. Approximating the ice-bedrock interface by a horizontal plane decreased variance reductions by 10% or more. Although the sensitivity studies showed robustness of the calculated fault mechanisms with respect to errors in Green's Functions, we therefore argue that for icequake moment tensor inversions at the current study site 3D Green's Functions were necessary. The sensitivity studies furthermore showed that for different fault mechanisms, such as double-couple sources and near-vertical tensile cracks, errors in Green's Functions can have a much larger impact on the results of

moment tensor inversions. Calculations of other basal icequakes may therefore bare further difficulties, depending on the nature of the source and the ice-bedrock interface near the hypocenters. On the other hand, the sensitivity studies showed that moment tensor inversions can be subject to ambiguities concerning the velocity profile used to calculate Green's Functions. In our case, Green's Functions of a homogeneous half space performed surprisingly well in the inversion, although we are certain that this model is incorrect, as the glacier is of finite depth.

Having focused on a single cluster with particularly clean waveforms, only, we acknowledge that there are likely other basal failure mechanisms which radiate seismic energy. The waveforms shown in Figure 3.4 point towards a high complexity of source and path effects. Further source studies of such events will likely lead to more interesting insights into basal processes but may require approaches which extend beyond moment tensor representations of material fracture.

Chapter 4

Basal Icequakes During Changing Subglacial Water Pressures Beneath Gornergletscher, Switzerland

FABIAN WALTER¹, NICHOLAS DEICHMANN²,
MARTIN FUNK¹

¹Versuchsanstalt für Wasserbau, Hydrologie und Glaziologie (VAW), ETH Zürich, 8092 Zürich,
Switzerland

²Institut für Geophysik, ETH Hönggerberg, CH-8092 Zürich, Switzerland

Published, *Journal of Glaciology*

Citation: Walter F., N. Deichmann and M. Funk (2008). Basal icequakes during changing subglacial water pressures beneath Gornergletscher, Switzerland. *Journal of Glaciology*, 54, 186.

ABSTRACT: Using dense networks of three-component seismometers installed in direct contact with the ice, the seismic activity of Gornergletscher, Switzerland, was investigated during the summers 2004 and 2006 as subglacial water pressures varied drastically. The causes of these pressure variations are the diurnal cycle of meltwater input as well as the subglacial drainage of Gornersee, a nearby marginal ice-dammed lake. Up to several thousand seismic signals per day were recorded. Whereas most icequakes are due to surface crevasse openings, about 200 events have been reliably located close to the glacier bed. These basal events tend to occur in clusters and have signals with impulsive first arrivals. At the same time, basal water pressures and ice-surface velocities were measured to capture the impact of the lake drainage on the subglacial hydrological system and the ice flow dynamics. Contrary to our expectations we did not observe an increase of basal icequake activity as the lake emptied, thereby raising the subglacial water pressures close to the flotation level for several days. In fact, the basal icequakes were usually recorded during the morning hours, when the basal water pressure was either low or decreasing. During the high pressure period caused by the drainage of the lake, no basal icequakes were observed. Furthermore, GPS measurements showed that the glacier surface was lowering during the basal seismic activity. These observations lead us to conclude that such icequakes are connected to the diurnal variation in glacier sliding across the glacier bed.

4.1 Introduction

Icequakes are seismic events inside glaciers, ice streams, frozen lakes or other large bodies of ice. For several decades they have been subject to a variety of studies. One benchmark was set by Neave and Savage (1970), who associated seismic events on Athabasca Glacier, Alaska, with the opening of surface crevasses. Thirty years later, Deichmann et al. (2000) showed that although an alpine glacier's seismic activity is dominated by crevasse openings, icequakes can occur at any depths. Whereas seismic emission from glacial ice has been studied in a variety of contexts such as the breaking-off of hanging glaciers (Faillettaz et al., 2008) and glacier calving (O'Neel et al., 2007; O'Neel and Pfeffer, 2007), seismic sources near the glacier bed are usually linked to basal motion and subglacial hydrology.

Weaver and Malone (1979) studied seismic events on glacierized volcanos in the Cascade Range, U. S. A. They reasoned that a number of their detected signals are due to sudden slip motion of the glacier across the bedrock. Métaixian et al. (2003) investigated icequakes detected on Cotopaxi Volcano, Ecuador. They detected signals which most likely originate from resonances of water-filled ice cavities, which may be activated by ice cracking or sudden changes in water flow near the glacier base.

Basal icequakes have been used to study conditions beneath Antarctic ice streams. Frequent radiation of seismic energy from near the ice stream base is usually associated with the absence of a deformable sediment layer, which is assumed to be a controlling factor in ice stream dynamics (e. g. Anandakrishnan and Bentley 1993; Anandakrishnan and Alley, 1994; Smith, 2006; Danesi et al. 2007).

Stuart (2005) studied the seismic emissions from a surging glacier in Svalbard, Spitsbergen. He found that specific basal icequakes may be directly related to the surging process.

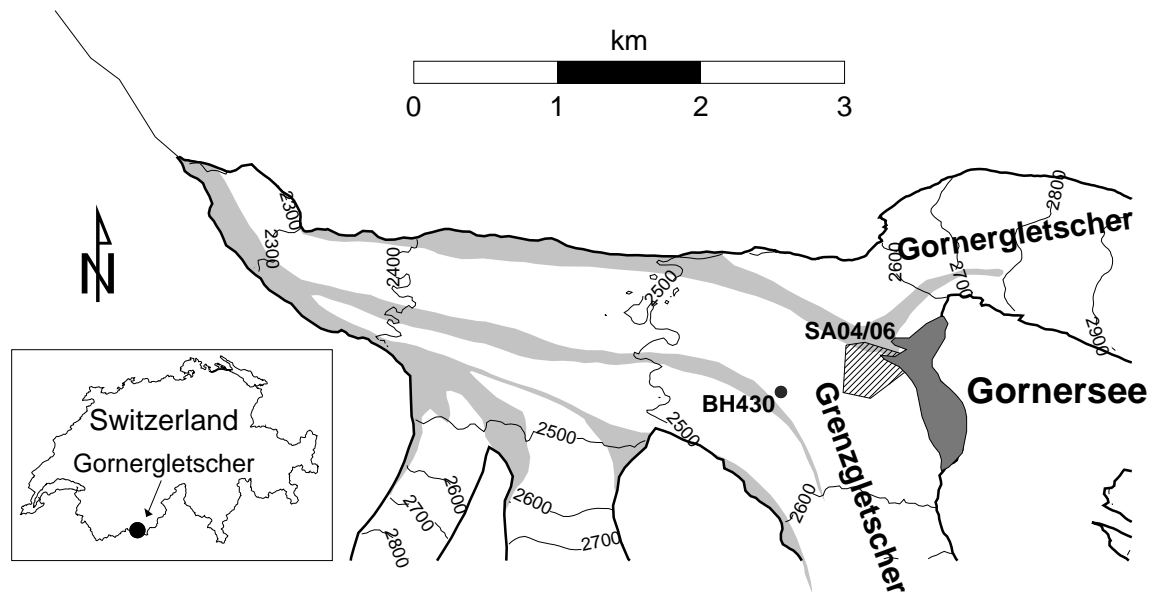


Figure 4.1: Overview of Gornergletscher. At the confluence area Gornersee is shown. Contour lines of surface elevation are shown (numbers give meters above sea level). The grey shaded areas are debris-covered portions of the glacier. The boundaries of the seismic networks deployed in the field campaigns of 2004 and 2006 are indicated by the hatched area. A pressure transducer was installed at the base of BH430, a 430 m deep borehole drilled to the glacier bed in 2004.

They originate from cracks ahead of the surging front, through which water penetrates to the bed. This induces a lubrication and heat transfer, which allows the surge front to move down-glacier.

In the present work we study basal icequakes on Gornergletscher and their relationship to changes of the subglacial water pressure. There are two main processes that induce these pressure changes by altering the water input into the subglacial drainage system: First, the daily increase in surface melt during the warm hours of the day and second, the sudden drainage of Gornersee, a marginal lake at the confluence of the two main tributaries of Gornergletscher, Switzerland. In both cases we observed increases in water levels inside boreholes of 100 m or more. Because this study was part of a comprehensive field and modeling investigation of the drainage of Gornersee we had the chance to include data on glacier hydrology and dynamics in the seismic analysis.

The sudden drainage of water masses located inside, beneath, or at the margin of a glacier is a well known phenomenon referred to by the Icelandic term 'jökulhlaup'. During a jökulhlaup, the discharge of affected proglacial streams can increase rapidly, often with hazardous consequences. Peak discharges can differ by several orders of magnitudes. Estimates for Pleistocene events are as high as $20 \times 10^6 \text{ m}^3 \text{ s}^{-1}$ (Roberts, 2005), whereas the peak discharges of Gornersee are on the order of $10 \text{ m}^3 \text{ s}^{-1}$. The high destructive potential of jökulhlaups underlines the need for investigations aimed at predicting magnitudes and onsets of the drainage events (Haeberli, 1983; Richardson and Reynolds, 2000; Björnsson, 2002; Raymond and et al., 2003).

The theoretical treatment of jökulhlaups poses two particular challenges: a description of the initiation mechanism and a description of the flow of water through englacial or subglacial channels. A model describing the evolution of englacial channels as a competition

between melt-enlargement and creep-closure has been studied and applied to a variety of flood events (Nye, 1976; Spring and Hutter, 1981; Spring and Hutter, 1982; Clarke, 2003). These studies, however, do not account for the possibility of brittle deformation of glacier ice. Roberts et al. (2000) showed that fracture processes play an important role in the englacial routing of flood water during a jökulhlaup. They identify hydrofracturing as a mechanism responsible for fracturing the ice: Fractures are driven into the ice above the glacier bed when the hydraulic pressure exceeds the threshold of the overburden pressure plus tensile strength of the ice. Clarifying the role of brittle deformation of glacier ice during the onset and progress of the drainage event was a major motivation for the present study.

4.2 Field site

The field experiments were conducted on Gornergletscher near Gornersee, which annually forms at the confluence of Gornergletscher and Grenzletscher located next to the Monte Rosa massiv in Switzerland's canton Valais (see Figure 4.1). The lake can contain up to several million cubic meters of water and drains subglacially almost every summer. For detailed discussions of Gornersee outburst floods, in particular those of 2004 and 2005, the reader is referred to Huss (2007) and Sugiyama (2007).

At the initiation of the outburst floods, the lake volumes in 2004 and 2006 were of comparable size at about $4 \times 10^6 \text{ m}^3$. In 2004, the lake drained subglacially with peak discharges of about $15 \text{ m}^3 \text{ s}^{-1}$. A rapidly rising discharge curve and large uplifts of up to 3 m of the glacier surface (Weiss, 2005) near the lake suggest ice dam flotation as a possible triggering mechanism. In 2006, Gornersee drained across the glacier surface: The lake level rose until a narrow lake arm reached a nearby moulin. The overflowing lake water almost immediately filled the moulin, raising its water level to that of the lake. After about one day, the moulin had adjusted to the large amount of lake water input. Consequently, a strong current developed inside the lake arm. The water flow gradually melted a spillway into the ice converting the lake arm into a fast flowing stream. The slow deepening of the canal formed a canyon and only allowed for peak discharges of less than $5 \text{ m}^3 \text{ s}^{-1}$.

4.3 Seismic Setup and Instrumentation

Figure 4.1 shows the locations of the seismic networks installed in 2004 and 2006. The networks consisted of 14 and 24 seismometers, respectively. Other measurement sites relevant to this work are shown in the detailed maps of the seismic arrays in Figure 4.2.

The setup consisted of three-component seismometers recording the velocity of ground motion in direct contact with the ice. The analog seismic signals were converted to digital ones by a seismic recorder ('GEODE' by geometrics). Up to eight seismometers could be linked to one GEODE. The GEODES applied an anti-aliasing, low-pass filter, whose frequency response decreases by -3dB at 83% of the Nyquist frequency. Apart from an analog-to-digital high-pass filter, which only affected frequencies below 2 Hz, no additional filters were applied at the recording stage. The GEODES were linked in series via an ethernet cable. A laptop equipped with an external hard disk was connected to

Table 4.1: Recording specifications. The variables are explained in the text. In 2006, the value of t_{pre} was changed several times to values in the range given here.

	2004	2006
Sampling Frequency	1000 Hz	4000 Hz
threshold ratio	10	20
n_{trig}	4	10
t_{rec}	2 s	1 s
t_{pre}	0.5 s	0.4-0.5 s

the 'master GEODE' and served as a storage device. Synchronization of all channels is guaranteed by the recorder, while absolute time is provided by the laptop's clock.

The majority of instruments were 1 Hz seismometers (Lennartz LE-3D; henceforth 'surface seismometers') placed on the glacier surface. The manufacturer specifies a flat frequency response up to 80 Hz. Surface melt required daily leveling of these instruments. In addition, 28 Hz geophones (Geospace GS-20DH; henceforth 'deep borehole seismometers') were placed in boreholes drilled with a hot-water drill to depths between 50 m and 250 m. In 2006, six additional 8 Hz borehole seismometers (Geospace GS-11D, henceforth 'shallow borehole seismometer') were installed at a few meters below the surface. For both types of borehole seismometers, the frequency response was assumed flat, at least up to the corner frequency of the anti-aliasing filter.

An amplification of 24dB and 36dB was applied to the surface seismometers and the borehole seismometers (both 8 Hz and 28 Hz devices), respectively. Table 4.1 summarizes the values of recording parameters that differed in the two field seasons. Because the recorders were not equipped with the software module necessary for continuous recording, only events detected by an automatic self-trigger algorithm were recorded. The trigger operated in the following way: A root mean square (rms) value of two concurrent time windows is computed. The rms value over the previous 800 ms 'long-time average' (LTA) window and the previous 80 ms 'short-time average' (STA) window are calculated and compared. When the ratio $\gamma = \text{STA}/\text{LTA}$ exceeds a given threshold (Table 4.1), that station is said to have triggered. In order to initiate recording, a minimum of n_{trig} channels had to satisfy the trigger condition. The trigger algorithm was applied to all three channels of each seismometer. Since for both years n_{trig} was greater than three, a single 3 component seismometer could not trigger the system. Once activated, recording took place for an amount of t_{rec} seconds. The recording window also included the signal detected prior to triggering, indicated by t_{pre} . In order to avoid multiple triggering per event, the trigger remained unarmed for a few tenths of a second after event detection.

4.3.1 2004 configuration

In 2004, 14 surface and one deep borehole seismometer (at 100 m depth) were operational between June 15 and July 8 (see Figure 4.2). The seismometer naming conventions were chosen such that the letter indicates which GEODE they were connected to, and the number specifies the seismometer. For the 2004 network, two GEODES were used, each connected to seven seismometers. GEODE A served as the master GEODE, to which the recording laptop was connected.

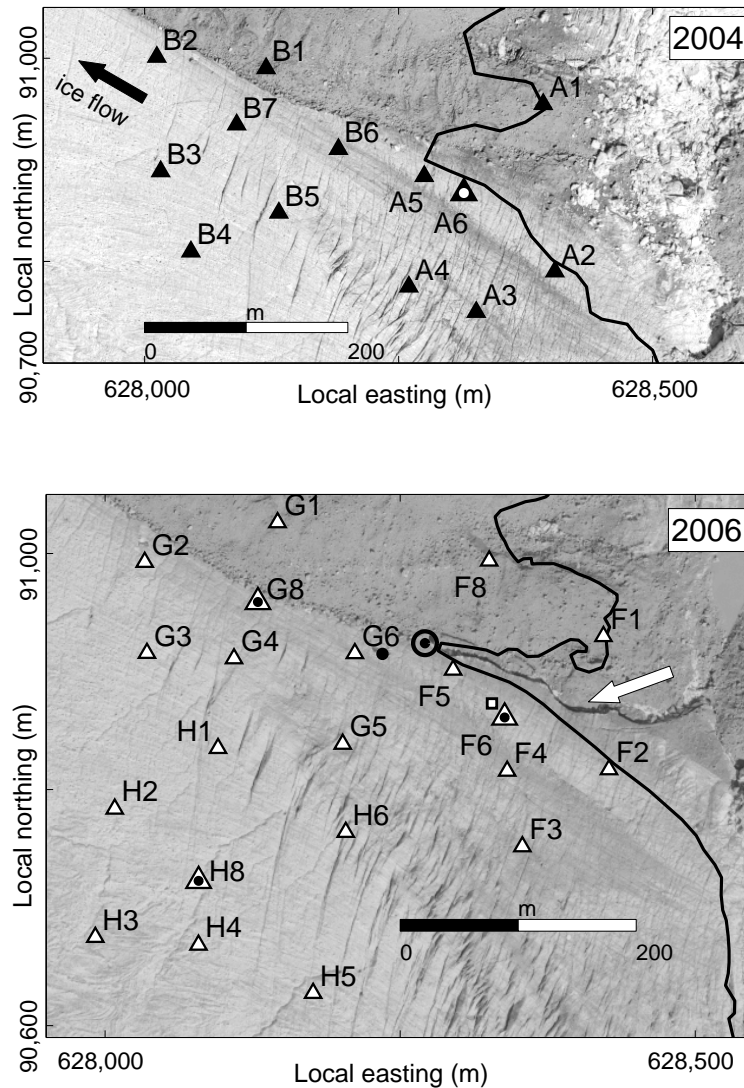


Figure 4.2: Ortho-photographs of the areas of the seismic networks in 2004 (upper) and 2006 (lower). The seismometers are indicated by triangles and a GPS unit by a white square (2006). At the locations of the large triangles with dots, a surface as well as a deep bore hole seismometer were installed. A black dot is plotted at the position of a 150 m deep borehole (BH6) to the glacier bed equipped with a pressure transducer (2006). The solid line represents the lake outlines at maximum lake level. The circled dot in the lower picture indicates the position of the moulin into which the lake drained in 2006, incising a canyon into the ice (white arrow). Coordinates of the Swiss Grid are shown.

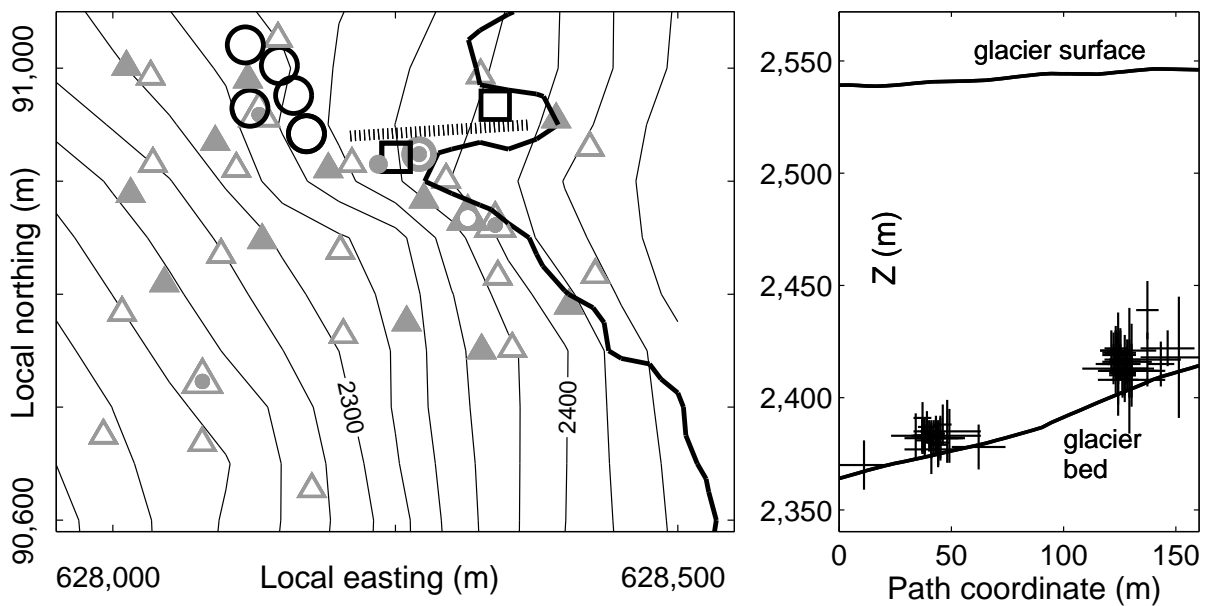


Figure 4.3: Left: Epicenters of deep icequake clusters detected in 2004 (big empty squares) and 2006 (big empty circles). Empty and solid triangles represent the 2004 and 2006 seismic stations, respectively. The lake outline (thick black line), borehole and moulin are indicated as in Figure 4.2. The contour lines approximate the elevation of the glacier bed (in meters), as determined via radio-echo sounding (Huss, 2005). The dashed line indicates the vertical cross-section path to show the hypocentral locations of the icequake clusters (right panel of this figure). Right: Hypocenters of the two 2004 clusters. The crosses indicate the icequake locations and uncertainties thereof as determined by the inversion described in the text. Coordinates of the Swiss Grid are shown.

4.3.2 2006 configuration

In 2006, the seismic setup consisted of 15 surface seismometers, three deep borehole seismometers (at 40 m, 140 m and 250 m depths) and six shallow borehole seismometers, operational between May 29 and July 28 (Figure 4.2). Three GEODES (F,G and H) were used to connect the seismometers to the recording laptop located at GEODE F (master GEODE). Figure 4.2 also shows the location of the moulin, into which the lake drained. Less than 40 m away, a borehole (BH6) had been drilled to the glacier bed and a pressure transducer installed. This allowed for monitoring of the basal water pressure in the vicinity of the moulin. As the lake drained into the moulin, these measurements were particularly valuable.

4.4 Seismic data

During the field seasons of 2004 and 2006, about 35,000 and 50,000 seismic events were detected, respectively. As expected (Deichmann et al., 2000; Neave and Savage, 1970; Aschwanden, 1992), the vast majority of the recorded signals was due to seismic sources close to the surface, probably associated with the opening of crevasses. Less than half a percent of all recorded events have been located at depths below the crevassing zone. However, these events are of particular interest in the context of this study, because they might be related to water propagation through sub- or intraglacial channels.

4.4.1 Identification of deep events

Because of the large number of recorded seismic signals, a form of automated signal recognition had to be used. We developed two techniques to identify the seismograms of deep icequakes among the large data sets: An automated waveform discriminator based on the presence or absence of the Rayleigh phase and a cross-correlation search.

The seismograms of deep icequakes show substantial differences to those originating from shallow depths (Deichmann et al., 2000): The P-wave recorded by near-surface sensors is very impulsive and strongest on the z-component. Additionally, the Rayleigh phase, which is characteristic of signals of shallow icequakes, is missing or much less pronounced in the records of deep events. Since the Rayleigh phase produced by shallow icequakes is of lower frequency than P- and S-phases, which dominate the deep icequake signals, the frequency of the dominant phase can be used as an automated waveform discriminator. Once the waveform discriminator based on the frequency content finds a set of deep events, a time domain cross-correlation can be used to find events with similar seismograms: We cross-correlate the z-component time series of a 'master' event with those of all other events detected in the particular field season. Each track is cross-correlated independently, which means that each track may show a maximum cross-correlation at a different lag. The spread in lag differences s_{lag} and the maximum cross-correlation coefficient R_{max} are used to quantify waveform similarity. 'Perfect similarity' is indicated by $R_{\text{max}} = 1$ and $s_{\text{lag}} = 0$. The cross-correlation search identified up to several dozens of events with similar seismograms that had previously been missed by the waveform discriminator.

4.4.2 Hypocenter location procedure

The icequake locations were found using a procedure described in Lee and Steward (1981). An inversion algorithm searches for locations in space yielding theoretical P- and S- arrival times as close to the hand picked ones as possible. The theoretical arrival times were calculated with user-input seismic velocities. Specifying higher velocities for the deep borehole seismometers accounted for crevasses and fissures near the glacier surface known to cause a slower seismic velocity zone within the top 20 m (Gischig, 2007). The seismic velocities we used were determined via a set of explosions at distinct locations throughout the seismic network. The arrival time picking accuracy was usually 5 ms or better. The uncertainties in locations are given by one standard deviation of the location errors calculated from the diagonal elements of the inverse normal equations scaled by the assumed timing errors. Most of the time, the uncertainties were no larger than 10 m in all directions. In some instances, however, they were as high as 30 m. The vertical component was generally subject to larger uncertainties than the horizontal ones.

4.5 Results

4.5.1 Deep icequake locations

2004 locations

More than 80 deep events were identified and located in the summer 2004. Most of these cluster in two distinct regions near the glacier bed. The epicenters of the remaining deep events are outside the seismic array. Consequently, the quality of their locations is poor and does not allow for further analysis of their source depths and possible clustering activity. Figure 4.3 shows the epicenters of the two basal clusters inside the seismic network. The clusters contain about 30 events each and their signals show a high degree of similarity which makes them very suitable for the cross-correlation search and suggests that they have similar source mechanisms. The hypocenters are located at depths of 150m. This corresponds closely to the glacier thickness as determined by radio-echo soundings (Huss, 2005). These thickness measurements, however, can contain an error of up to 20 % of the thickness. Taking the uncertainties of the icequake locations into consideration, as well, we cannot determine at this point whether the icequakes are at the ice-bedrock interface, just above or just below it. The signals of the western-most 2004 cluster (Figure 4.3) show a higher degree of similarity than those events belonging to any other cluster detected in 2004 and 2006. Figure 4.4 shows the first seven recordings from this cluster, which occurred over a time of about one week. The events belonging to this subset show particularly high coherence. Any pair of seismograms belonging to this subset yields a correlation coefficient R of 0.86 or higher when using the entire waveform and 0.98 when using the first P-arrival, only (using a bandpass filter between 5 and 80 Hz). Like most of the basal icequakes considered in this study, signals of the ones shown in Figure 4.4 lasted between 0.1 s to 0.2 s at all stations. Figure 4.4 furthermore shows typical impulsive P-arrivals, which are particularly pronounced on the vertical component. The second main phase is the direct S-arrival, whereas no significant Rayleigh wave can be seen. Besides the two basal clusters, about 25 deep icequakes located about 500 meters north-west of the array were found. For these, the location quality in all dimensions is very poor

(uncertainties of up to 100 m). This is due to the bad azimuthal distribution of recording seismometers. Yet the signals show impulsive first arrivals, typical for deep icequakes. Furthermore, the first motions of the P-waves recorded at the deep borehole seismometer indicate that the hypocenters lie at depths comparable to the depth of this seismometer (100 m). Whereas the clustered events lying within the network have pronounced P- and S-phases, the signals of the deep events lying outside the seismic network have little or no S-energy.

2006 locations

The set of deep icequakes detected in 2006 shows several differences to that of 2004. In 2006, the total number was nearly 200, as opposed to about 80 in 2004. This may be partially due to the larger seismic array. Similar to 2004, the majority of the 2006 basal icequakes shows clustering. However, about 40 deep icequakes in the 2006 set were not associated with a cluster. Of these 40 scattered events, more than half were reliably located at intermediate depths within the ice. Therefore, their sources were unlikely to be associated with surface crevassing, which is confined to depths of about 20 m (Paterson, 1994) or with basal brittle fracture. Deichmann et al. (2000), found only one such event on Unteraargletscher, Switzerland. Although the location quality was good, it seemed somewhat suspicious that among over three hundred located icequakes on Unteraargletscher only one occurred at intermediate depths and several dozens near the glacier base. Figure 4.3 shows the region of highest activity containing five clusters with over 120 events. The sizes of the clusters are quite different: they contain between about 10 and 50 icequakes. Most deep icequakes show the typical impulsive P-arrivals, which are usually compressive possibly indicating a highly isotropic source. However, unlike in 2004, some events also show dilatational first arrivals which may be evidence for a deviatoric source or a collapse.

4.5.2 Icequake activity

In the remainder of this paper, variations in icequake activity on different time scales are discussed. The focus is directed to the events belonging to the 2004 and 2006 basal clusters shown in Figure 4.3 (henceforth basal cluster events). As will be shown, the activity of basal cluster events reaches its maximum during times when the remaining seismicity, consisting almost exclusively of surface icequakes, is relatively low.

Influence of trigger

Water flow on the surface and within the glacier can substantially increase the seismic background noise of the glacier and thus decrease the trigger sensitivity of the instruments. Enhanced water flow can be the result of precipitation events. Precipitation records of 2004 and 2006 show several such events throughout the summer. We scrutinized the data sets to evaluate if the timing of precipitation events may introduce a substantial bias to the trigger sensitivity and thus event detection. The patterns in event detection presented here show no systematic dependence on the occurrence of precipitation events. Regarding changes of seismic activity on a diurnal scale and with respect to the lake drainage, we

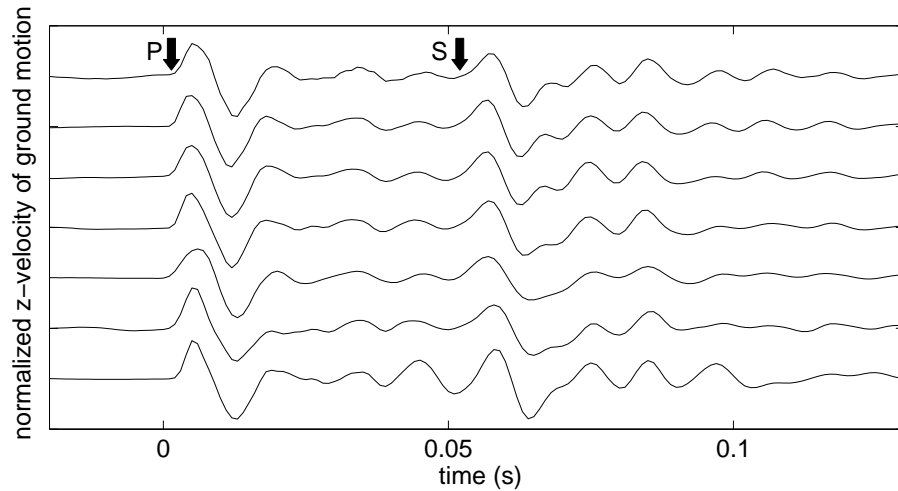


Figure 4.4: Vertical velocity seismograms of a subset of icequakes belonging to the western 2004 cluster, all recorded at station A6 (Figure 4.2 and Figure 4.3). P- and S-arrivals are indicated. A 2nd order causal Butterworth bandpass filter with corner frequencies of 5 and 80 Hz was applied to each signal. The events were recorded between June 15 and June 20, 2004. Among all events belonging to this cluster they show the highest degree of similarity ($R \geq 0.86$ for entire waveform and $R \geq 0.98$ for first P-arrival).

therefore conclude that the changing trigger sensitivities induced by precipitation events may be neglected.

The diurnal surface melt cycle, however, does induce a considerable trigger bias: During the day, meltwater runoff into streams and moulins increases the seismic background noise of the glacier. Because the trigger is effectively measuring signal to noise ratio (using the STA/LTA threshold), as noise increases the trigger sensitivity decreases. This means that the trigger is more sensitive at night or in the early morning hours. As we are concerned with secular variations in seismic activity, we must account for variations in trigger sensitivity that could falsely be interpreted as seismic activity variability. In this and the following section, the approach to this problem is explained in detail using the 2004 set of recorded signals. An equivalent procedure was applied to the 2006 data.

The changing trigger sensitivity also affects the performance of the waveform discriminator. Events with high signal to noise ratios are more easily identified, a characteristic that deep events during night times are more likely to possess than those during day times. The cross-correlation technique, on the other hand, is less sensitive to changes in background noise, because prior to performing the cross-correlation the signals are bandpass filtered between 5 and 200 Hz. This is further discussed at the end of this section.

Because the majority of identified deep icequakes occur in clusters and have similar signals (Figures 4.3 and 4.4), the cross-correlation technique detects these events efficiently once a single or few members of the cluster are found by the STA/LTA method. If events were only found via the waveform discriminator it is difficult to judge whether their occurrence reflects actual seismic activity or merely a time of low background noise with high signal-to-noise ratios. On the other hand, the cross-correlation technique permits event detection that is less sensitive to background noise. Therefore, we have analyzed only clusters whose event-detection was via the cross-correlation technique.

In order to investigate the changing trigger sensitivity, the relative strengths of the

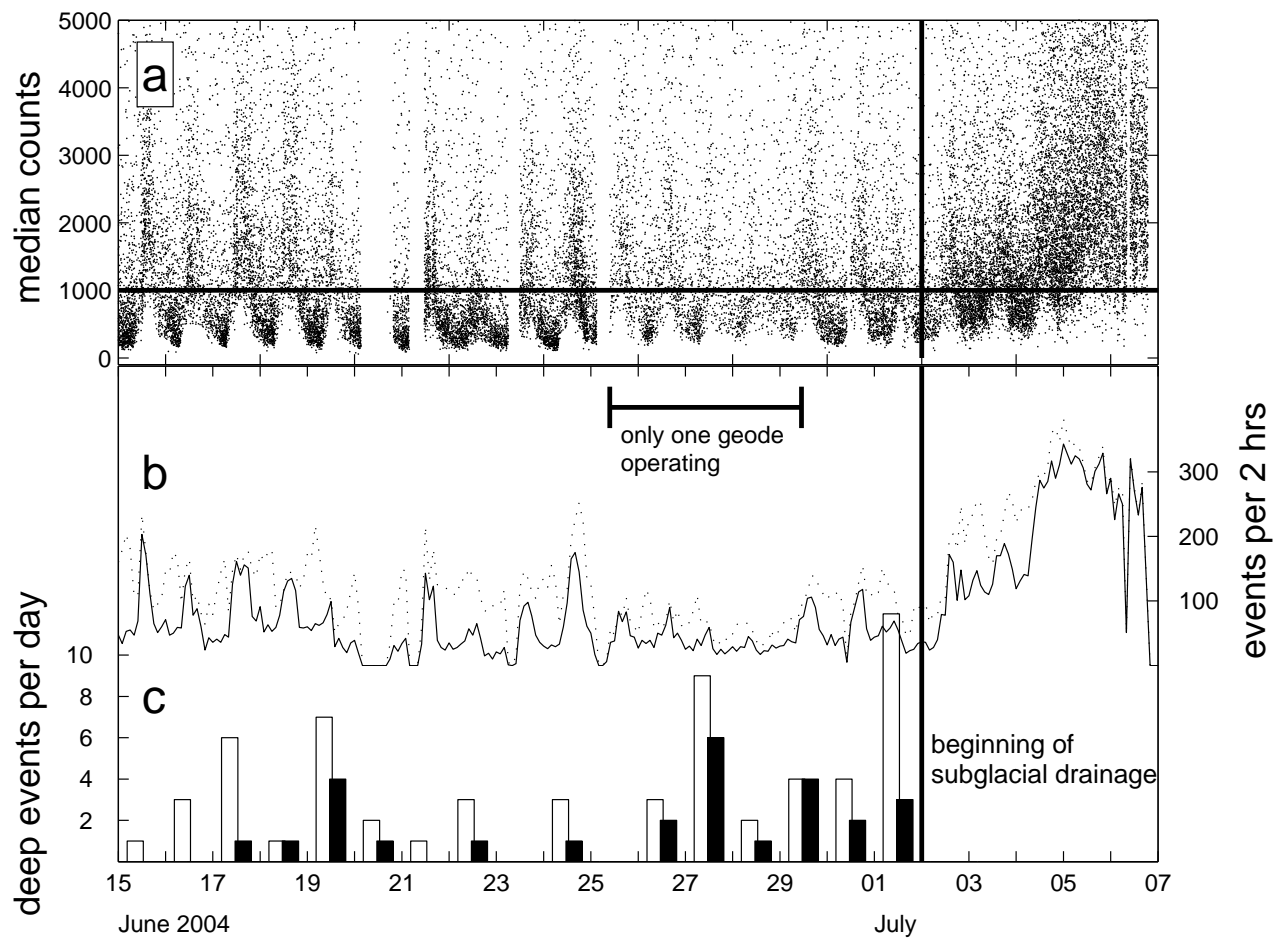


Figure 4.5: Seismic activity on Gornergletscher measured by the 2004 seismic array. (a) Median counts of the recorded seismic signals are calculated by taking the median of the maximal amplitudes at all 14 seismometers. Each black dot corresponds to one recorded event. For illustration purposes the strongest 10% of the signals is not shown. The strengths of the weakest seismic signals are prone to diurnal variations due to the high daytime noise. The horizontal line represents the median count cut (minimum completeness). On June 20, 21, 23, 25, 29, 30 and July 6 there are missing recordings due to instrument malfunctions. Between June 25 and June 29 only the seven seismometers of Geode A were operating. (b) Seismic activity in bins of two hours. The dotted line includes all recorded signals, the solid line only those with median counts above 1000 (horizontal line in a). (c) Histogram of the activity of deep events. Empty columns include all events belonging to the 2004 clusters shown in Figure 4.3, the solid columns only those with median counts above 1000 (horizontal line in a). Note that no basal cluster events were detected after the beginning of the lake drainage.

recorded signals were determined: For each event, the median of the maximum amplitudes of all seismometers was computed. Figure 4.5a shows the result for the 2004 data. Varying on a diurnal scale, as expected, the median count level of the weakest signals can be used as a proxy for trigger sensitivity: At night, signals can be recorded that would be too weak to trigger the system during the day. Therefore, these 'weak' events may reflect the trigger sensitivity rather than diurnal variations in seismic activity. Based on Figure 4.5a we assume that above a median count level of 1000 counts (horizontal line in Figure 4.5a), the recorded events form a complete set ('strong' events), meaning that they would be strong enough to trigger recording at any time of day.

For the 2006 data, those events subject to changing trigger sensitivities were determined in the same manner. The only difference is that the threshold was found to be 2000 counts, twice as high as in 2004. The reason was that the low level cut-off of icequake median counts is not as clear as in 2004. This most likely is an effect of the different trigger settings (Table 4.1) and the larger number of seismometers.

To confirm the robustness of the cross-correlation search with respect to seismic background noise, we conducted search runs with 2004 basal cluster signals to which we artificially added noise. The goal was to examine if signals with added daytime noise generally do not pass the search criteria whereas those with night time noise do. In that case the changing background noise of the glacier strongly influences the performance of the cross-correlation search.

The noise time series was extracted from a 0.5 s pre-event time window of the regular 2 s event files. The 0.5 s of seismic noise was then concatenated with itself to a 2 s noise time series. For each day during which basal cluster icequakes were detected, 24 noise seismograms were constructed, each one containing noise from a different hour of the day. To these noise time series we added the basal cluster signals of the same day. We then performed the cross-correlation search on each cluster using the time series that consisted of the sum of noise and signal.

Out of the 24 strong basal cluster events that were found in 2004, 17 events were detected by the cross-correlation search in all cases of added noise. Three events were no longer detected during several or all hours during both day and night. Two events failed detection with daytime noise while passing detection with night time noise. However, this was only the case during one or two afternoon hours. Merely two events were so weak that they could only be detected during low-noise morning hours. Thus we conclude that for the majority of strong basal cluster events detection via cross-correlation search is not sensitive to changing seismic background noise.

4.5.3 Background glacier seismicity (2004)

Before the lake drained, between 20 and 100 events per hour were recorded (Figure 4.5b). Note that between June 25 and June 29 only one geode was operating, which is likely the cause of reduced daily peaks. As the lake drained, the number of strong events increases to more than 150 events per hour on July 5. During the first half of the drainage, the fraction of weak icequakes is significantly larger than during the maximum of the seismic activity on July 5, when the large majority of icequakes passes the median count cut (Figure 4.5b). It is difficult to assess the meaning of this observation, since the locations

of these icequakes have not been determined. The change in relative abundance of weak and strong signals may be due to changes in location or changes in source strength.

As shown in Figure 4.5c, up to twelve basal cluster events per day were found. Almost half of them are strong enough to pass the median count cut. On July 1, just prior to the lake drainage, 12 basal cluster events occurred. Although most of them are weak, this seems to mark a period of high activity. During following days (between July 2 and July 7, which marks the end of the recording), while Gornensee drained, no more basal cluster events were detected. Yet on July 2, 3 and 4 the night time seismic noise level appears to be low enough to allow recording of weak basal cluster events as on July 1. After July 5, the lake drainage seems to increase the seismic background noise significantly (Figure 4.5a). This probably inhibits recording of weak events even during the night.

4.5.4 Diurnal activity

It is clear from Figure 4.5b that the activity of icequakes shows significant variations within a diurnal range. To illustrate these variations, the icequake occurrence (source times) stacked for each hour of the day is shown in Figure 4.6. Only days that show no gaps in recording were used for this stack (see Figure 4.5 caption). The icequake activity as determined from all strong recorded signals (black solid line) reaches a daily maximum in the early afternoon. During night time and morning hours the activity is much lower. This is expected since during the warm hours of the day, glacier flow reaches a maximum because of basal sliding. Note that the diurnal signal in activity does not appear when including the weak events (dotted line). We suggest that the larger number of recorded weak events compensates for the actual lower activity rate at night.

The small subset of basal cluster events shows a different diurnal variation (histogram in Figure 4.6, top): none of the strong basal cluster events occur during the times of maximum seismic activity shown by the black line. They instead tend to occur during the early morning hours or late at night when the overall seismic activity reaches a low.

As can be seen in Figure 4.6 (bottom), the data of 2006 reproduces these diurnal fluctuations in icequake activity: Again, when considering the set of 'strong icequakes', the overall seismic activity reaches a maximum between early and late afternoon. On the other hand, the activity of basal cluster events is highest during night times and the early morning hours.

The systematic occurrence of the stronger deep icequakes, which is opposite to that of the overall seismic activity is a central point of the present work. This is a robust observation because potential biases of the diurnal variations of the trigger sensitivity were accounted for by considering only those icequakes above the median count threshold. Furthermore, as we showed above, the daytime seismic background noise is not strong enough to prevent detection of strong basal cluster icequakes via cross-correlation search. In order to stress this point, consider the 17 strong basal cluster events that are detected despite the addition of daytime noise. None of the basal cluster events of 2004 occurred between 12:00 and 20:00, an 8 hour long time window. If the 17 strong ones occurred randomly throughout the day and independently of each other, then the probability of not detecting any of them between 12:00 and 20:00 would be $(1 - \frac{8\text{h}}{24\text{h}})^{17} = 0.001$. We therefore attribute the systematic detection of basal cluster icequakes during night time hours

to changing source activity and not to changes of the detection threshold due to diurnal variations of the seismic background noise.

4.6 Discussion

The analysis of the diurnal activity of the basal cluster icequakes showed the following main results: First, strong basal cluster events occur predominantly in the morning hours or late at night. Second, the overall seismic activity of the glacier, in contrast to that of the basal cluster events, is maximal in the afternoon. Third, there is no evidence that the lake water input leads to an increase in basal cluster events. In fact, during the 2004 subglacial drainage and at the onset of the 2006 overflow of Gornensee, no basal cluster icequakes were detected.

These results cannot be explained by hydrofracturing, by which cracks are opened up with high water pressures. If this were the process responsible for the basal cluster events, high source activity would be expected during the warm hours of the day when meltwater enters the subglacial drainage system with the potential to increase basal water pressures drastically. Also the influx of water due to the lake drainage alters the subglacial hydrological conditions in a manner to favor hydrofracturing rather than to suppress it.

4.6.1 Comparison with basal water pressure

A comparison between the source times of basal cluster icequakes and the time series of basal water pressures measured in nearby boreholes is further evidence against hydrofracturing. Figure 4.7 shows the data of pressure sensors in bore holes BH430 (2004) and BH6 (2006). Their locations are given in Figures 4.1 and 4.2. Whereas borehole BH430 was somewhat remote from the 2004 seismic network and the basal cluster events detected that year (about 800 m from the center of the seismic array), borehole BH6 was drilled in the immediate vicinity of the 2006 clusters and of the moulin that the lake drained into (see Figure 4.3).

Prior to the lake draining, both time series show large diurnal pressure fluctuations of up to 100 m or more which nearly reach flotation level during pressure peaks. This is evidence for the good connection of the boreholes to the subglacial drainage system. During the 2004 lake drainage, for about four days, the basal water pressure remained high even during night time, when it usually drops. Thus, diurnal pressure fluctuations are much less pronounced. Note that the pressure rise is not exactly coincident with the beginning of the lake drainage. This time lag may be due to the distance between lake and borehole. It is also difficult to define an accurate beginning of the 2004 drainage event, since supraglacial drainage and icedam flotation preceded or accompanied the subglacial drainage (Huss, 2007).

In 2006, a similar pressure rise was observed during the beginning of the drainage. Again, for about two days, the water pressure did not fall during the night. This high pressure level could also be observed at the surface. Once the lake overflowed into the moulin, it quickly filled it, so that the water level reached the glacier surface. However, unlike in

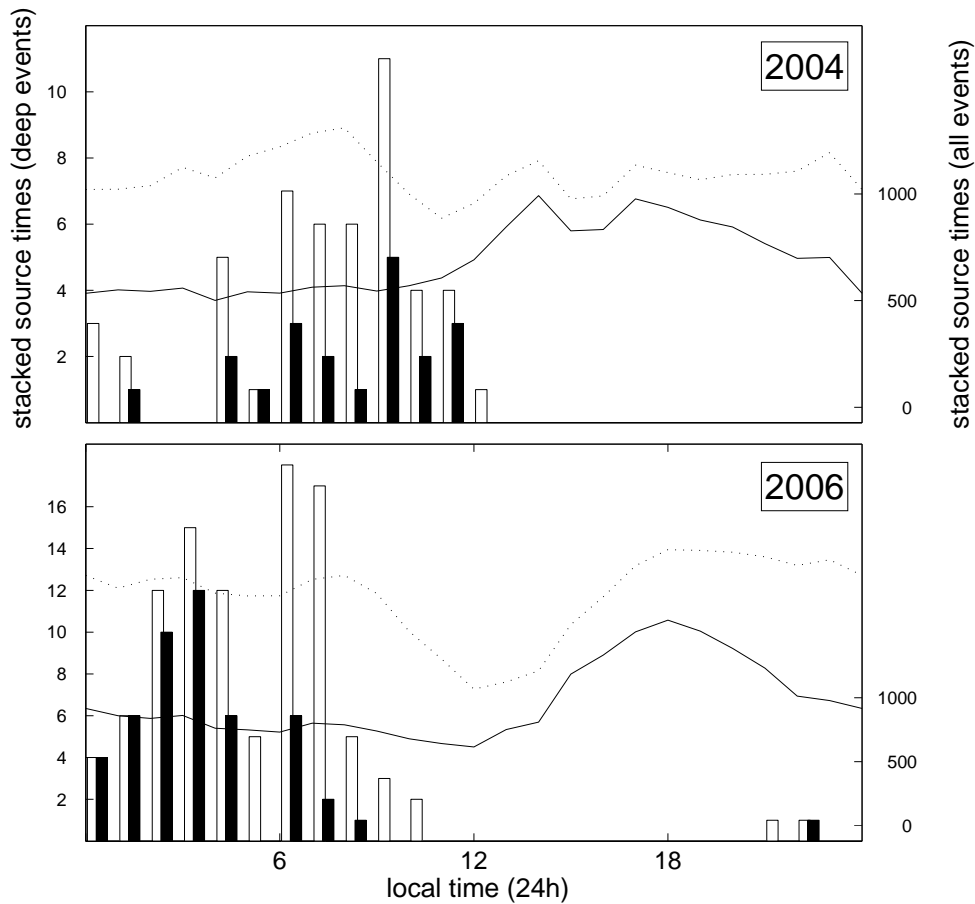


Figure 4.6: Stacked times of icequake occurrences ('source times') of years 2004 (upper) and 2006 (lower). The histogram shows the stacked source times of deep icequakes. Empty columns correspond to all basal cluster events and solid columns to those above the median count cut. The dotted line shows the stack for all detected events (shallow or deep). The solid line represents the subset of events passing the median count cut. Note the relatively even distribution of all seismicity, with a small peak in the afternoon, whereas the basal cluster events appear to exclusively occur in the early morning and late evening hours.

2004, after about one day, the subglacial drainage system adjusted to the water input and the diurnal pressure fluctuations manifested themselves once again.

Figure 4.7 (top) also indicates the source times of the basal cluster events in 2004 and 2006. In 2004, all cluster events occur on the falling limbs of the diurnal pressure peaks. None occur at the pressure peaks. Furthermore, no basal cluster icequakes occur just prior to and during the lake drainage.

The 2006 basal cluster events (Figure 4.7, bottom) occur almost exclusively at the lowest pressures measured on the day of their occurrence. As in 2004, no basal cluster events were detected during the high pressure period of the lake drainage. Basal cluster events were recorded again after the moulin saturation when pressure fluctuations resumed.

Summing up the comparison between the diurnal fluctuations of basal cluster icequake activity and basal water pressure it can be stated that there is no evidence that high water pressures cause basal icequakes. Instead, these seismic events seem to occur during low or decreasing water pressures. It is therefore unlikely that hydrofracturing is the cause of these seismic events.

4.6.2 Comparison with surface motion

Between July 1 and July 5, 2006 continuous GPS measurements are available from a receiver installed near station F6 (Figure 4.2). Figure 4.8 shows the (average) stacked surface uplift for this time period. The accuracy of a single GPS measurement is ± 0.3 cm (Sugiyama and Gudmundsson, 2004). The graph further shows the stacked basal water pressure of the same period as measured in borehole BH6 as well as the temporal occurrence of basal cluster events detected in this time period. The GPS data was very noisy and was smoothed before stacking. This was done using a moving average filter with a shape given by the function $(1 - (d/w)^2)^2$, where d is the distance in time from a data point to the center of the filter and $w = 4$ hours is the filter length. In addition, an overall trend was subtracted from the time series. It should be mentioned that the GPS data was too noisy in order to take time derivatives of the horizontal coordinates to reliably determine diurnal fluctuations in horizontal surface velocities.

The surface uplift shows a pronounced diurnal fluctuation. The peak is reached at around 20:00, whereas the low occurs just before noon. The surface lowering during the morning hours is interrupted by a small bump starting at around 04:00. This feature can also be seen in the unstacked data. The origin of this change in lowering rate is not known.

These fluctuations from the overall trend have an amplitude of about one centimeter, which is several times smaller than the diurnal uplifts observed further down on the glacier tongue (Huss, 2007, Weiss, 2005). The reason for this is probably that further down the glacier bed becomes horizontal. This allows for the temporary storage of daily meltwater with the potential to lift up the glacier over larger regions. Under the seismic study site, on the other hand, only the glacier's surface is horizontal whereas its bed is strongly inclined (Figure 4.3). Meltwater runs down this incline and can only be stored in small quantities in local depressions. A large uplift of the glacier over larger areas is therefore not possible.

Figure 4.8 shows the key relationship between surface uplift and the source times of the basal cluster events: The latter occur exclusively during the period of surface lowering.

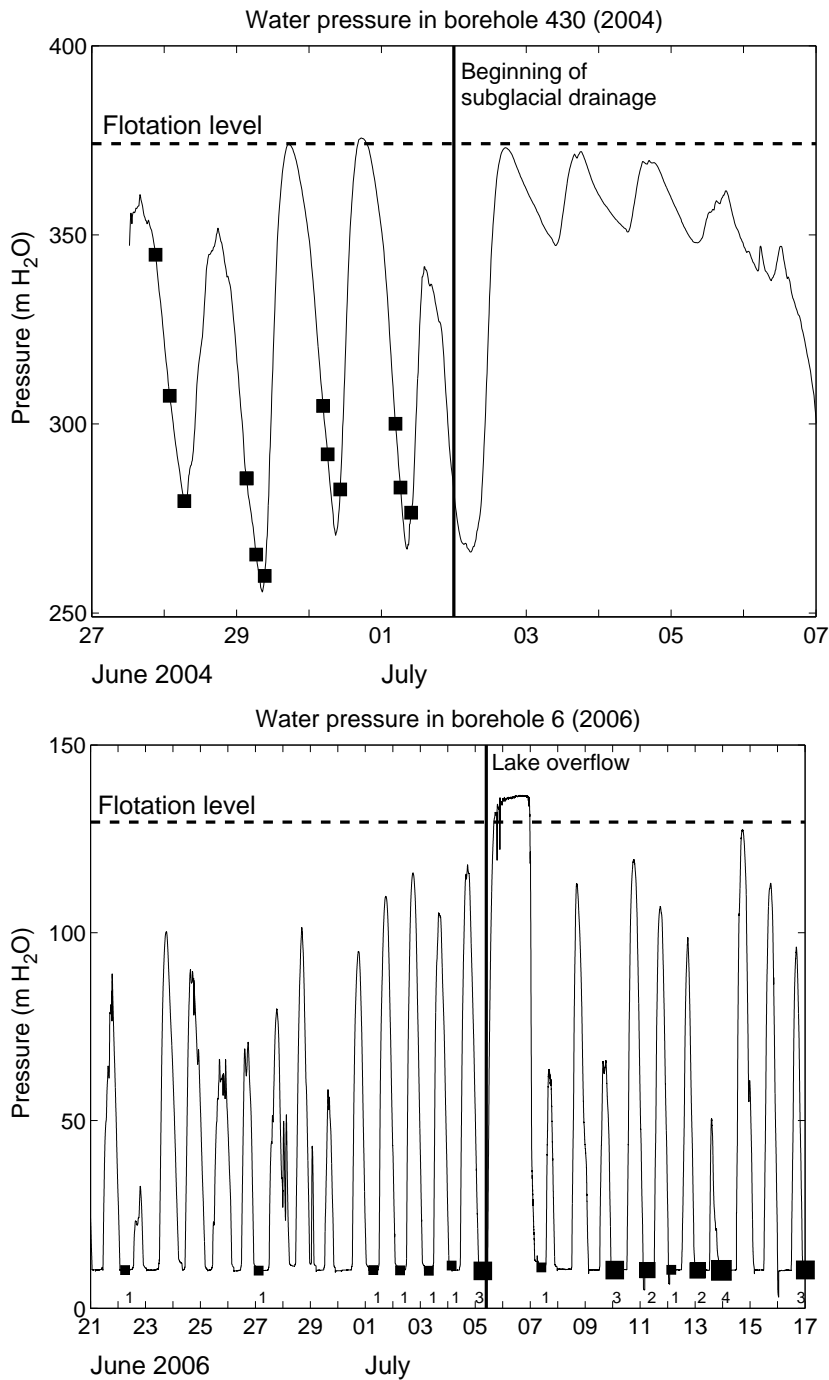


Figure 4.7: Basal water pressures as measured in borehole 430 (upper panel, see Figure 4.1 for location) and borehole BH6 (lower panel, see Figure 4.2, 2006, for location). The pressure sensor in borehole BH6 was installed about 20 m above the bed, resulting in a low pressure cut-off whenever the water level sank below the pressure sensor. The solid vertical line marks the beginning of the lake drainage events for each year. Superimposed on the pressure time series are the source times of the 'strong' basal cluster icequakes of that year (black squares). For 2006, the size of the squares indicates how many icequakes occurred during that time period (their number is given below each square). Note that the basal cluster icequakes occur only at pressure decreases or near minima.

Considering also the weak events (empty bars), the figure suggests that the basal cluster events may be related to the bump that interrupts the overall lowering of the surface. Another interesting observation is that the surface uplift reaches its maximum after that of the basal water pressure. Sugiyama and Gudmundsson (2004) made the same observation on Unteraargletscher, Switzerland.

4.6.3 Source mechanism

A central yet open question that arises from this investigation is what mechanism causes basal clustering of icequakes. The seismic moment tensors of these events would give quantitative information about fault geometry, fault strength and failure mechanism (e.g. double-couple or isotropic) and are therefore of high value in answering this question. As a second step, modeling glacier flow subject to strong changes of basal boundary conditions can provide clues about the deformation of basal ice layers. The modeled stress and strain fields can help understand why the fracture types as given by the moment tensor solutions occurred. At this point, we discuss possible source mechanisms considering the temporal fluctuations in activity and observed seismogram characteristics.

One possible reason for icequakes near the ice-bedrock interface may be sudden slip motion of the glacier. Previously, such motions were studied under Antarctic ice streams (Anandakrishnan and Bentley, 1993; Anandakrishnan and Alley, 1994), which have a sliding component to their motion. Weaver and Malone (1979) concluded that seismic signals obtained from monitoring three Cascade Volcanos in Washington State, U. S. A., originated from such motion, as well. Considering the signal characters we now present evidence against such a source.

A slip motion is a shear failure near the base of the glacier. It produces a seismic radiation pattern consistent with a double-couple source (Aki and Richards, 2002) which is a function of the azimuth of the vector connecting source and recording station. This dependence manifests itself in a quadrantal azimuthal distribution of compressive and dilatational first arrivals of the seismic waves. Specifically, if the slip occurs in a plane parallel to the glacier bed and in the downhill direction, the first P-wave motions uphill of the failure region will exhibit dilatational polarity, whereas those downhill of it are compressive (for a discussion of seismic radiation patterns of specific sources see Aki and Richards, 2002). Anandakrishnan and Bentley (1993) noticed first arrival patterns that are expected for slip motion under the Antarctic Ice Streams B and C. As far as the present study is concerned, all 2004 and the large majority of the 2006 basal cluster events show compressive first motions, only. Scrutinizing one of the 2004 basal clusters, it was found that slip motion in the direction of the bed inclination cannot produce compressive first arrivals at all stations (Gischig, 2007). Although full waveform inversions to calculate the seismic moment tensor are needed to describe the seismic sources of the basal cluster events rigorously, the radiation pattern of first arrivals indicates that stick-slip motion is not responsible for the majority of basal cluster events.

4.6.4 Basal processes

Tensile failures within the basal ice layer can produce compressive first motions at all azimuths and thus seem more plausible than shear failure. Hydrofracturing can cause

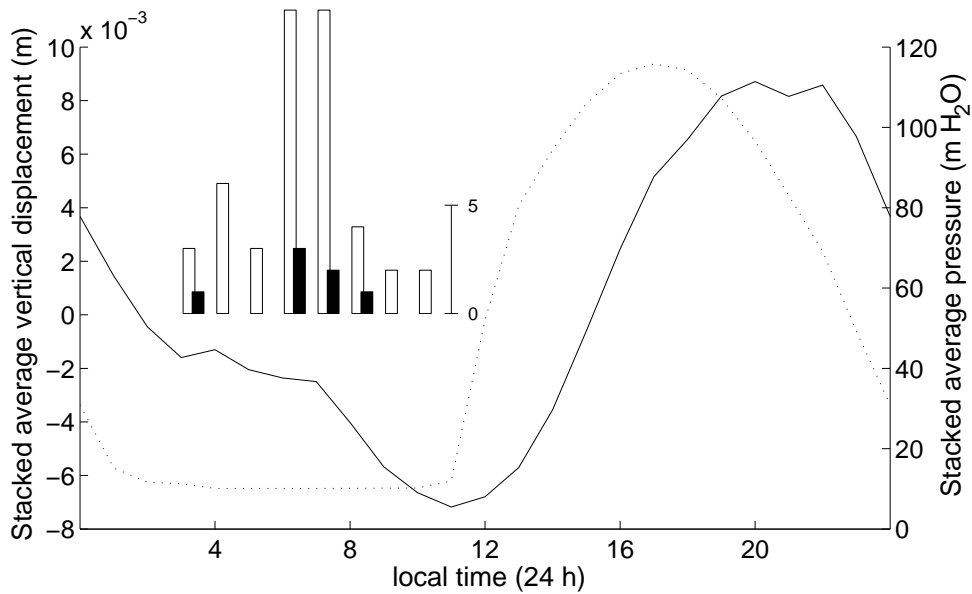


Figure 4.8: Comparison between surface uplift (solid line), basal water pressure (dotted line) and the source times of basal cluster events (histograms) between July 1 and July 5, 2006. Empty columns represent the stacked source times of all detected basal cluster events, solid columns those of the strong ones. The surface motion and basal water pressure were measured with a GPS unit near station F6 and inside borehole BH6, respectively (Figure 4.2). The uplift and pressure graphs were produced by stacking and averaging the time series during the 5 days. The GPS data has been smoothed with a moving average filter (see text). Note that the basal cluster icequakes occurred at times when the surface was lowering.

these kinds of failures. For instance, pressurized water may enter preexisting cracks and extend them. This process has been studied theoretically for surface and bottom crevasses (Van der Veen, 1998a; Van der Veen, 1998b; Van der Veen, 2007). However, we also reject this kind of mechanism due to the diurnal activity of the basal cluster events, which tends to peak at low or decreasing water pressures.

The dependence of glacier sliding on basal water pressure provides a better explanation than hydrofracturing does. In the remainder of this discussion we make some propositions of how sliding may affect basal cluster activity and what role basal water pressure might play.

Equation 4.1 is an empirical relation between sliding velocity u , basal shear stress τ and the difference of basal water pressure p_w and ice overburden pressure p_i , also called effective pressure (Paterson, 1994).

$$u = k\tau^p(p_i - p_w)^{-q} \quad (4.1)$$

Here, p and q are positive integers and k is a constant that depends on the thermal and mechanical properties of the glacier ice and increases with decreasing bed roughness. According to this equation sliding is drastically enhanced for subglacial water pressures approaching the ice overburden pressure, which is the case at or near the study sites of the present work (Figure 4.7). If the water pressure reaches flotation level over a large enough region of the glacier bed, it can decouple the glacier from its bed. On the other hand, the large diurnal water pressure drops near the bed lead to a strong decrease in sliding. As the basal ice layer couples to the bed again it has to undergo large deformation rates due to the braking action of the bedrock on the glacier base.

We suggest that this deformation of basal ice is responsible for its tensile fracturing and thus causes the basal cluster icequakes. Although the coupling of the ice to the bed may cause primarily shear stresses, failure can still occur in the direction of maximum tension, similar to what is observed in the case of simple shear at glacier margins (Paterson, 1994). The high basal deformation might be favored in distinct regions due to the presence of obstacles, high bed roughness or spatially unevenly distributed water masses. This can explain the clustering behavior of these icequakes. An interesting observation is that the locations of the 2006 clusters had not produced basal icequakes in 2004. An explanation may be the changing subglacial drainage system. At a certain time, a region of the glacier bed may be particularly well connected to the drainage system. The large diurnal basal water pressure differences result in large deformation rates and fracturing of nearby basal ice during low water pressures. In a subsequent year the drainage system may have changed and the large pressure fluctuations needed to cause fracturing of the basal ice layer are no longer occurring in this region.

Another explanation for basal cluster events may be found in the evolution of water filled cavities at the glacier bed. The bed near the seismic network may be too inclined (Figure 4.3) to allow basal water to accumulate and decouple the glacier over a large region. However, the large diurnal fluctuations in basal water pressure causing varying sliding velocity may still lead to large enough deformation rates of basal ice to cause basal cluster events. During high basal water pressure periods water filled cavities on the lee-sides of bed undulations grow. Iken (1981) showed that this cavity growth greatly enhances sliding. As the pressure drops the large hydrostatic pressure inside the basal glacier ice

causes it to fill the cavities again. In this process ice may actually flow 'uphill' into the cavity. The large diurnal fluctuation of the basal water pressures suggest that water may leave such cavities rapidly. In this case large deformation rates can be expected as the basal ice closes the cavities rather quickly, possibly leading to basal cluster events. This process may explain the observation that basal cluster events occur as the surface lowers (Figure 4.8): The small diurnal lifting and lowering of the surface may be due to the local evolution of cavities. In this case the lowering would correspond to the closing of these cavities. It should be emphasized, however, that cavity creation is just one of the possible explanations for surface uplift. The latter may also be due vertical straining, which has been shown to vary on a diurnal scale as well (Sugiyama, 2003).

Generally, the basal ice beneath the study site can be expected to be particularly prone to large deformation rates. Whereas the glacier bed is strongly inclined, its surface is nearly horizontal in this region. Consequently, the ice thickness grows quickly in the down-glacier direction. The basal shear stress, τ in equation 4.1, essentially has to support large parts of the downhill force on the ice. As the thickness increases so does the downhill force and thus the basal shear stress. According to equation 4.1 the sliding velocity also increases in the downhill direction thus leading to stretching of the ice near the glacier bed. This can explain why the basal cluster events can be expected particularly in this part of the glacier.

4.7 Conclusion

We have studied the effect of diurnal basal water pressure variations and the drainage of a glacier-dammed lake on seismic emissions near the base of Gornergletscher. This investigation was part of a comprehensive field and modeling effort to understand the interaction of the Gornersee drainage with glacier dynamics and hydraulics. The seismic network thus operated concurrently with acquisition of GPS and borehole pressure data. This allowed for comparison between the glacier's seismic activity, dynamics and hydraulics. No evidence was found that the passage of the lake water through or under the glacier caused brittle deformation radiating seismic energy. Instead, basal cluster icequakes predominantly occurred during low or decreasing water pressure. During water pressure peaks caused by the lake drainage and daily surface melt no basal cluster events were detected. Therefore, we cannot report the detection of hydrofracturing of basal ice in the vicinity of the study site such as observed by Roberts et al. (2000). We explain the basal icequake activity that we detected on Gornergletscher by considering variations in sliding velocity caused by basal water pressure fluctuations. This model assumes that deep basal icequakes are caused by tensile fracturing near the glacier bed rather than stick-slip motion. The compressive arrivals of P-waves observed at all azimuths are an indication for tensile faulting, too. Shear faulting as in the case of stick-slip motion would produce a quadrantal pattern of compressive and dilatational P-arrivals (Aki and Richards, 2002).

As a next step, full waveform inversions to estimate source properties should be made to further characterize icequake sources. In addition, numerical ice flow models can help understand how large basal deformation rates can occur as basal hydrological conditions change. In this view, measurements of inclinometers installed inside the glacier in the summer 2006 may be of great value. They, too, show diurnal signals which are likely to be induced by varying basal water pressures (VAW, unpublished data).

In any case, passive seismic measurements such as those described here provide a suitable means to study basal processes. In the current study this is particularly interesting since the lake drainage causes an abrupt perturbation to the subglacial conditions which has a significant impact on the entire glacier.

Acknowledgements

The project was funded by the Swiss National Science Foundation, grants No. 200021-103882/1 and 200020-111892/1. We are grateful to many members of VAW, the Institute of Geophysics and the Swiss Seismological Service of ETH. By making their instruments available, H.-R. Maurer and the Applied and Environmental Geophysics group made the seismic measurements possible. Seismogram picking was done with the software package SNAP written by M. Baer. The Swiss military provided valuable help in form of transportation of equipment via helicopter. The reviews of S. Anandakrishnan and M. Roberts were extremely helpful and are gratefully appreciated. Furthermore, we would like to express gratitude to M. Werder, M. Huss, A. Bauder, M. Lüthi, R. Gutzler, B. Nedela and J. Clinton for their constructive comments during the preparation of this manuscript and for their help during the field campaigns.

Chapter 5

Outlook on Analysis of the Gornergletscher Seismic Data

5.1 Overview of Future Work

Only a small fraction of the seismic data recorded during the field seasons of 2004, 2005, 2006 and 2007 has been analyzed. The vast majority of recorded icequakes has not been investigated, let alone been located. Furthermore, there are aspects of the seismic records, such as the ambient seismic noise, or records of nearby tectonic earthquakes, which did not directly fit into the context of the present work but nevertheless should be pursued in future research efforts. So far, the analysis of the Gornergletscher seismic data has been focused on a very small subset of events. As the data was investigated in the context of changing hydrological conditions inside and under the glacier, those events well below the surface crevassing zone have been of interest. Continuous data recorded in 2007 contain a large number of basal icequakes, whose source times and fault mechanisms have yet to be investigated in the context of basal water pressure variations. Whereas this complements results of previous studies of basal icequakes, we also propose studies of near-surface seismicity, as it provides information about ice dynamics near the surface, which was concurrently investigated with geodetic measurements.

For all field seasons, it would be interesting to study the changes of near-surface seismicity prior to, during and after the drainage of Gornensee. It has been shown that the glacier's surface motion responds to the drainage event (Huss et al., 2007; Sugiyama et al., 2007 and Riesen, 2007). Consequently fracture processes emitting seismic energy are also expected as a response to the drainage.

Aside from the regular icequakes that have been the center of attention of the present work, the glacier's seismic background noise should be subject to future investigations. In North America, seismic background noise as generated by ocean waves has been used in seismic tomography studies (e. g. Shapiro et al., 2005) and ground motion prediction via calculation of Green's Function responses from the ambient noise field (e. g. Prieto and Beroza, 2008). Furthermore, Burtin et al. (2008) developed a method to use seismic noise as a means to monitor hydrodynamic processes in a trans-Himalayan river.

Water flow on the glacier surface, within the glacier or at its bed likely emits seismic noise that can be analysed as in the above mentioned studies via signal stacking and cross-

correlating. That way, changes of water flow due to the diurnal melt cycle and the lake drainage could be identified and allow for insights into the location of drainage passages. For this purpose, continuous data acquired in the summer 2007 is particularly useful.

A large calving event occurred during the 2007 field season. In the process, about one million cubic meters of ice were lifted under buoyant forces. This event was accompanied by a surge of seismic events. The seismic record is several minutes long and consists of many sub-events. Relative locations and fault mechanisms of the individual cracks composing the seismic record during the calving event will elucidate crack initiation and propagation leading to the calving event thus contributing to the results of previous seismic studies of glacier calving (O'Neel et al., 2007 and O'Neel and Pfeffer, 2007).

In all these investigations it is important to determine icequake or ambient noise source locations. So far this was done by calculating hypocenter locations from hand-picked arrival times. This is only possible if the events have impulsive p- and/or s-arrival times. Seismograms of distant icequakes or ambient noise lack such clear arrivals and can therefore not be located with this technique. However, such signals often share a high degree of coherence among stations allowing for the application of seismic array techniques (e. g. Rost and Thomas, 2002). The advantage of array seismology is that the locating procedure can be automated and no hand picking is necessary. Preliminary results have shown that such techniques can be applied to the seismic arrays on Gornergletscher in order to reliably determine back-azimuths.

5.2 2007 Data Set

The main goal of the 2007 data was to detect basal icequakes with a continuously recording seismic array. As previous measurements had shown that the sensitivity of the trigger algorithm changes due to fluctuations in seismic background noise (Walter et al., 2008) continuous measurements were needed to record basal icequakes even during times of high seismic background noise.

The data analysis followed a procedure similar to that outlined in Walter et al. (2008). We applied a triggering algorithm to the continuous data set to extract a set of icequake records equivalent to the 2004, 2005 and 2006 records. Subsequently, a waveform discriminating algorithm was applied to the triggered data set to identify deep icequakes. These events were then located by hand-picking their arrival times. Once several clusters of deep icequakes were found, a cross-correlation search over the *continuous* record was used to find more members of a given clusters in the continuous data set. As the cross-correlation is less sensitive to seismic background noise, it finds events that had been missed by the trigger algorithm.

Besides the basal events, the 2007 data set features another interesting seismic record: On July 1 a large calving event ($\sim 10^6 m^3$) occurred, during which the glacier tongue that terminated in the lake broke off via hydraulic jacking. This event was recorded by all seismic instruments. A detailed study of source locations and mechanisms will offer the unique opportunity to study fracture processes during glacier calving.

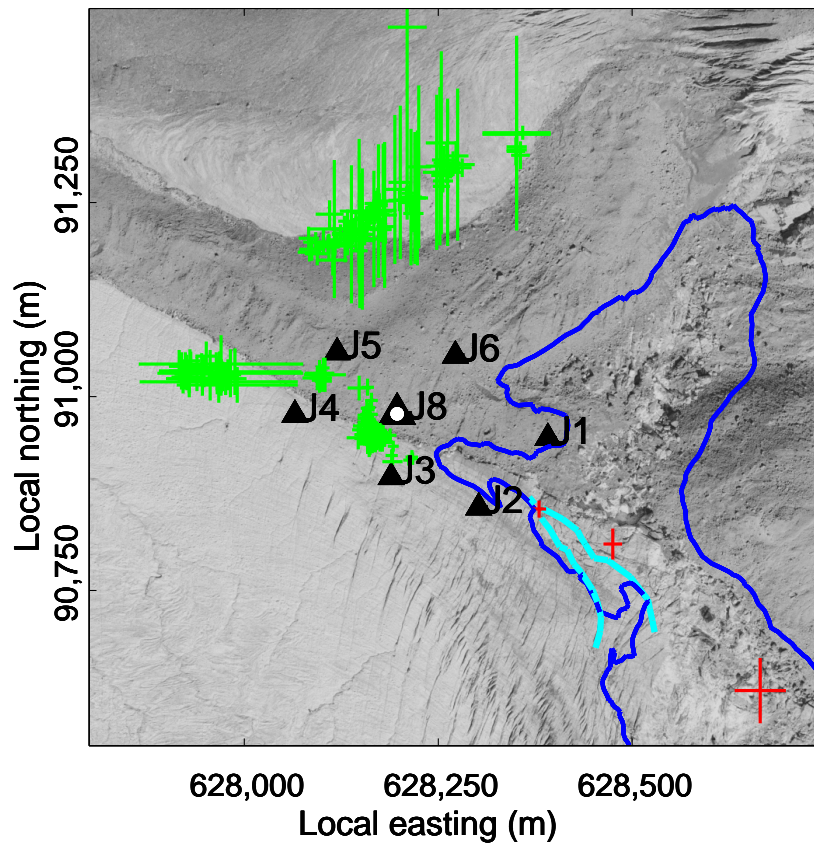


Figure 5.1: 2007 seismic array and event epicenters with location uncertainties. Green crossbars represent clustering basal events and red crossbars represent selected seismic events associated with the calving event on July 1 2007. At the larger dotted triangle a borehole seismometer (at 122 m depth) was installed below a surface seismometer. The blue line represents the lake outline at the highest lake level in 2007. The cyan line outlines part of the ice tongue that detached from the glacier in the process of the calving event.

5.2.1 2007 Seismic Array

Between May 25 and July 22, 2007, we installed 7 borehole seismometers near the glacier surface and one borehole seismometer at a depth of 122 m (Geospace GS-20DH and GS-11D) (Figure 5.1). The array was operational between May 25 and July 22 and recording in continuous mode at a sampling frequency of 1000Hz.

5.2.2 2007 Basal Icequakes: Results

Close to 500 basal events and about 30 intermediate events have been identified and located in the summer of 2007. We have concentrated the analysis on the basal icequake cluster (consisting of over 300 events) near station J8 (Figure 5.1). Figure 5.2 shows the

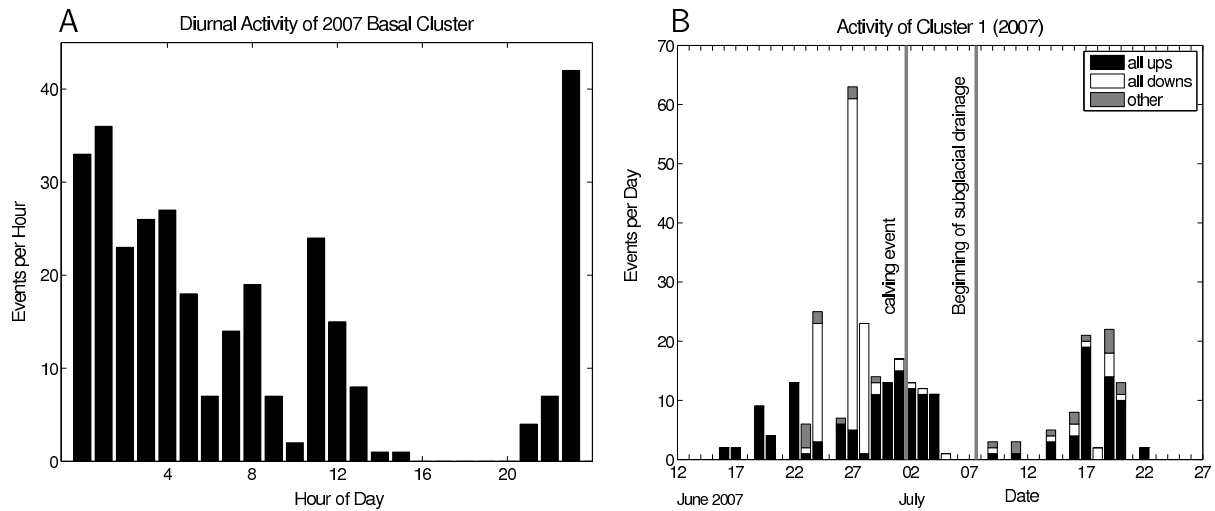


Figure 5.2: Activity of the basal cluster near J7 recorded in 2007. The diurnal activity as represented by stacked source times (A) shows a low during the afternoon hours, confirming earlier results from measurements in 2004 and 2006. The cluster was active for more than a month (B). Black and white bars represent opening- and closing-type sources, respectively. During the last week of June, the activity of closing-type events was remarkably high.

activity of this cluster. The stacked histogram of source times (A) shows the same trend that was previously observed in the activity of basal icequakes on Gornergletscher (Walter et al., 2008; Chapter 4). The seismic activity is highest during the night and the early morning hours and lowest during the (warm) afternoon hours. The activity of the cluster does not appear to respond to the calving event or the lake drainage (Figure 5.2B). An interesting observation concerning this basal cluster is that it is made up mainly of two distinct types of events. The first type has impulsive P-arrivals (first motion 'up'), which are compressive at all recording azimuths. This is a waveform characteristic that had been observed in previously recorded basal icequakes and is evidence of a tensile crack opening. The waveforms of the second type are very similar, except that their first motions are dilatational ('down') at all recording stations. Only about half a dozen such events had been observed previously in 2006. Such patterns of first motion suggest a collapsing or closing crack source.

Figure 5.3 shows the seismograms of two events belonging to the basal cluster beneath station J8 (Figure 5.1). Both were recorded at station J4. The horizontal axes x and y have not been rotated into the source-station coordinate system and do not correspond to geographic directions. The events lie eight days apart, but the orientation of the axes is the same for both events. Figure 5.3A most likely shows the seismogram of an opening crack, as at all azimuths compressive first motions were recorded. The waveforms in Figure 5.3B, on the other hand, correspond to a closing crack, with dilatational first motions at all stations. Note that the relative amplitudes of P- and S-waves varies between events, which suggests different fault plane orientations.

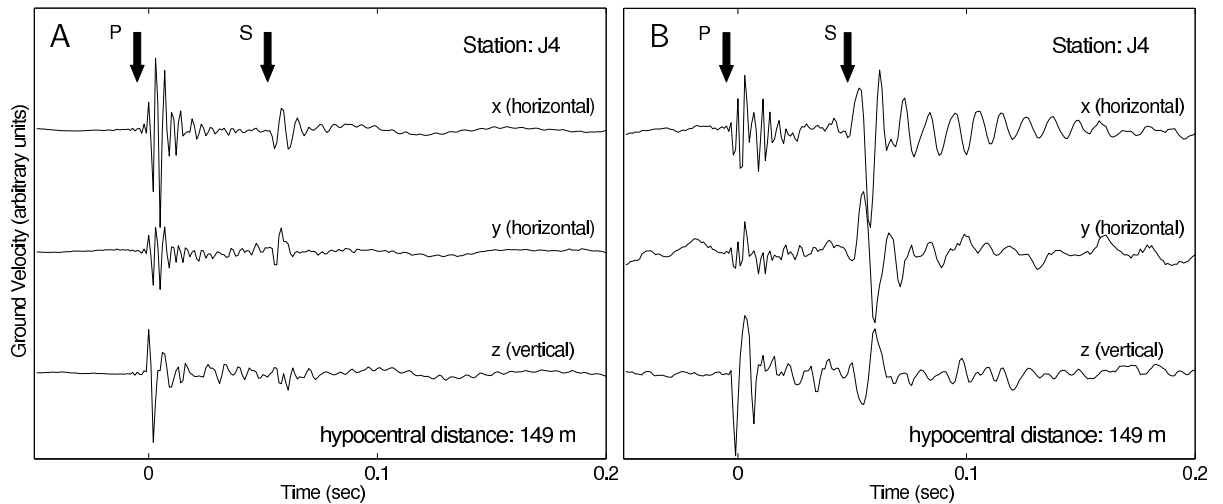


Figure 5.3: Seismograms of two events belonging to the 2007 basal cluster beneath J8. Both seismograms were recorded at station J4. Panel A shows an opening-type and panel B a closing-type event. Note that differences in P- and S-amplitude ratios exist, which hints towards differences in fault plane orientations.

5.2.3 Basal Cluster 2007: Future Work

Moment tensor solutions for events of the basal cluster beneath J4 should be calculated for a large number of events. This may show if systematic differences exist in the fault plane orientations of opening and closing-type events. Furthermore, the cluster activity should be compared to records of basal water pressure, surface motion and borehole inclination. Does the surge of closing-type events on June 27, 2007, correspond to a particular motion or pressure event?

5.2.4 2007 Calving Event

On July 1, 2007, a large calving event occurred on Gornersee. About $10^6 m^3$ of ice of the glacier tongue were lifted by buoyancy and detached from the glacier (Figure 5.1). The tongue underwent a rotational motion in the sense that the eastern side submerged in the lake moved upward by more than 9 m, while the western side attached to the glacier initially remained fixed to the glacier. Within minutes, the ice on the western side of the ice tongue was not able to support the upward motion and consequently failed along a 'hinge crack'. The final vertical displacements across this crack were as high as 3 m.

5.2.5 Seismicity During 2007 Calving Event

The calving event is clearly visible on the continuous seismic record (Figure 5.4). All records show a surge of seismic activity, about two minutes long. Station G7J1, which was located closest to the lake, shows an extended period of uninterrupted ground vibration, often strong enough to clip the signal (Figure 5.4A). Figure 5.4B shows an unusually strong seismic event that appears to mark the initiation of the calving event. This seismic event was located in the basin of the lake (most southern red crossbars in Figure 5.1).

However, P- and S- arrivals are difficult to identify, and may in fact have been picked incorrectly. Hence, the given location may not be reliable. A number of strong events then followed, one of which is shown in Figure 5.4C (epicenter at center red crossbars, in Figure 5.1).

An interesting seismic event was found about five minutes prior to the main calving event. It is shown in Figure 5.4D. Located near station G7J2 (most northern red crossbars in Figure 5.1) it has first motions in the 'up' direction only at stations G7J1 and G7J2. At all other stations, the polarities of first motions are opposite. This suggests a source mechanism other than a tensile crack opening, such as a double-couple or a CLVD. The former may be evidence for a vertical dip-slip fault suggested by the vertical displacement across the hinge-crack.

5.2.6 2007 Calving Event: Future Work

A first step would be to identify individual icequakes in the seismic record during and just prior to the calving event. These events can then be picked and located if the signals permit hand-picking of first arrivals. Furthermore, for similar events, high-precision relative locations will likely indicate rupture geometry and fracture propagation directions. For good azimuthal coverage, the procedure by Deichmann and Garcia-Fernandez (1992) can be applied. If the sources are well outside the seismic network, 'source-array' techniques (Rost and Thomas, 2002) can be applied to calculate relative locations. Subsequently, moment tensor inversions should be applied to selected events in order to study the role of shear and tensile failures.

5.2.7 Seismic Noise Cross-Correlation with 2007 Continuous Data

Preliminary results show 1-hour long segments are enough to bring out correlation maxima between different stations. Figure 5.5 shows the results of the correlation using 1-hour segments between 05:00 and 05:59 on July 9 (Figure 5.5, upper) and between 08:00 and 08:59 on July 10 (Figure 5.5, lower). The lake began to drain on July 7, which means that both time series used may have recorded seismic noise due to the propagation of water through sub- and intraglacial channels. The cross-correlated time series are the vertical components of stations G7J5 and G7J6. In order to minimize the effect of icequakes, 1bit normalization was applied to the time series (Bensen et al., 2007). The lags at which the cross-correlations reach their maximum, called 'zero-lag', are different from zero in both plots. This indicates that the source of the ambient noise is located in a preferred direction. Specifically, a positive zero lag shown in both cross-correlations means that the noise source is closer to station G7J5 than to station G7J6. This is consistent with a noise source located in the lake or at its margins.

The two cross-correlations are not identical and the zero lag for the cross-correlation of July 9 is larger than the zero lag on July 10. This means that the glacial seismicity is not identical at both times. As the zero lags changes, one may speculate that the noise source is located at a different azimuths. If the noise is mostly due to lake drainage channels, this change in azimuths may indicate changes in water routing.

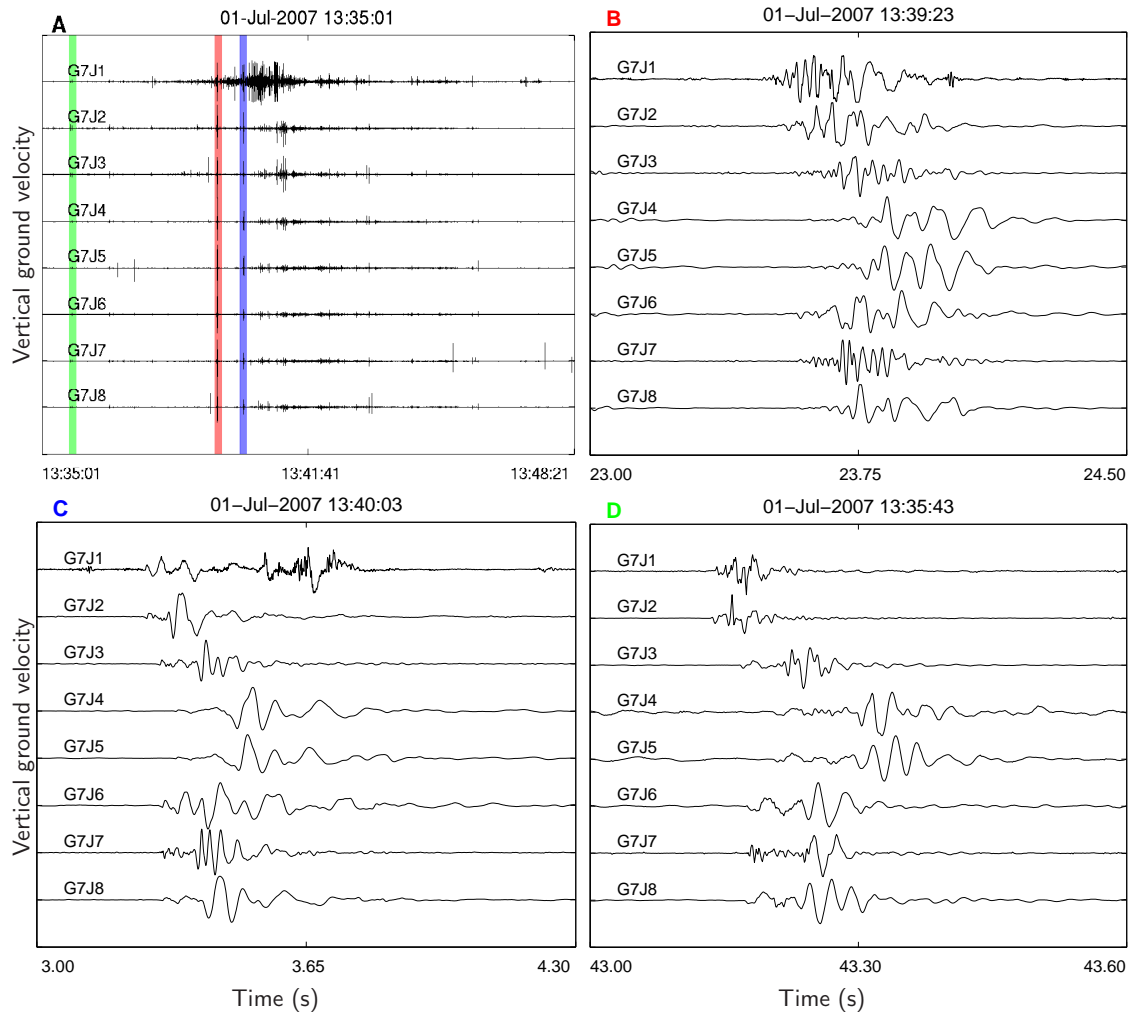


Figure 5.4: Seismic record of calving event on July 1, 2007. A: 13 minute long record containing the seismicity accompanying the detachment of the ice tongue from the glacier. Note that station G7J1 shows the strongest ground motion as it was closest to the calving front. B-D: Seismograms of individual events contained in the record shown in panel A.

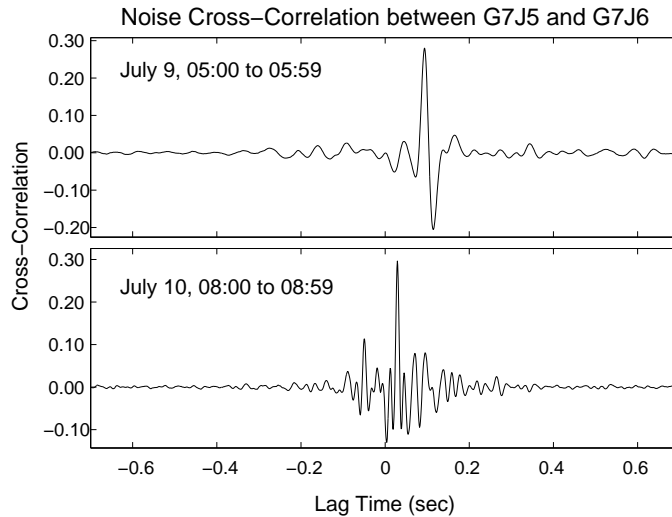


Figure 5.5: Cross-correlation of two one-hour segments of continuous data (1bit normalization applied). The vertical component of ground velocity recorded at stations G7J5 and G7J6 was used in the cross-correlation. Note that the zero lag is different for the two cross-correlations, hinting towards a change in noise source.

A powerful application of ambient noise cross-correlation is the possibility to extract Green's Function responses. Specifically, cross-correlating the z-component time series at station G6J5 with the x-component time series at station G6J6 will give the x-ground motion at station G6J6 due to a force impulse in the z-direction at station G6J5. Cross-correlating the component pairs zx, zy and zz, we can therefore retrieve the ground motion at station G6J6 in response to a vertical force at station G6J5. Figure 5.6 shows the results. The main motion is planar, and we rotated the ground motion about the z-axis such that the plane of motion coincides with the paper plane. This suggests that the ground motion due to a vertical force impulse located at station G6J5 is a Rayleigh wave.

5.2.8 Noise Correlation: Future Work

It should be further investigated how the azimuths of the seismic sources change over time. Thus it may be possible to monitor drainage channel locations of the lake outburst and of the diurnal surface melt. The determination of azimuths can be done using array techniques (see Section 5.3). Furthermore, phase velocities can be calculated from Green's Functions obtained via cross-correlation. It should be investigated if next to Rayleigh phases, P- and S-phases can also be deduced. Such phase velocities can then be used in a seismic tomography, which is particularly interesting in view of changes of water content in the glacier ice.

The quality of noise cross-correlation is reduced if distinct seismic signals from earthquakes (or icequakes as in the present study) are present in the time series. Due to the high frequency of event occurrence this may compromise the success of ambient noise studies on temperate glaciers. In order to reduce the effect of distinct seismic signals in noise records, several processing techniques have been developed and are documented in Bensen et al., 2007.

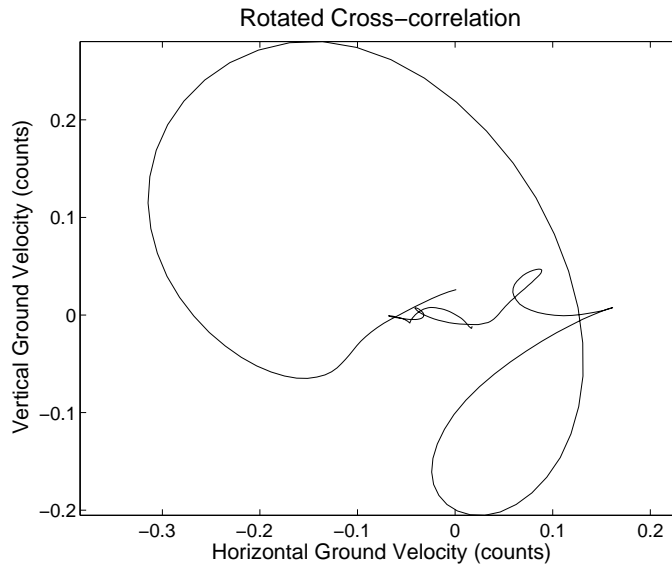


Figure 5.6: 2D illustration of ambient noise cross-correlation between two one-hour noise records of stations G7J5 and G7J6. The cross-correlations between the component pairs zx , zy and zz were plotted against each other and then rotated to the plane of the main phase. This corresponds to the ground motion response at station G7J5 to a vertical force impulse at station G7J6. According to the elliptical shape shown in the figure, this response is dominated by a Rayleigh wave.

5.3 Array Techniques

The seismic networks installed on Gornergletscher in the summers of 2004, 2005, 2006, and 2007 were located in areas where the drainage of Gornersee was expected to have a substantial impact on the glacier dynamics. In order to attain high-quality epicentral locations, a good azimuthal coverage of the seismic sources of interest was desired.

'Array seismology' (Rost and Thomas, 2002) is a terminology commonly used for processing techniques applied to seismic data from sources, which are not recorded with a good azimuthal coverage. Instead, the seismic source is located outside the array. As a consequence, locations based on arrival-time inversions can be subject to large uncertainties. On the other hand, the seismic signals arriving at the array are usually highly coherent. If the source is far enough away from the seismic array so that the seismic waves arrive as plane waves, the signal coherency can be exploited to determine the back-azimuth to the epicenter and apparent slowness of the seismic phases (e. g. Del Pezzo et al., 1997). If the source is close enough to the array so that the wave fronts still have a substantial curvature, circular wavefront-geometry can be used to estimate a source-array distance (Almendros et al., 1999).

For planar and circular waves, back-azimuth and epicentral location can be found via 'beam-forming' (Rost and Thomas, 2002). For a given back-azimuth or test location the theoretical arrival time delays between stations are calculated using a specific horizontal slowness. The individual traces are then shifted according to these time delays and stacked. At the correct back-azimuth or location this 'beam' is amplified to a maximum. Instead of stacking, cross-correlations between stations can be used, too. The horizontal slowness of the dominant wave phase can be determined by a grid search over this

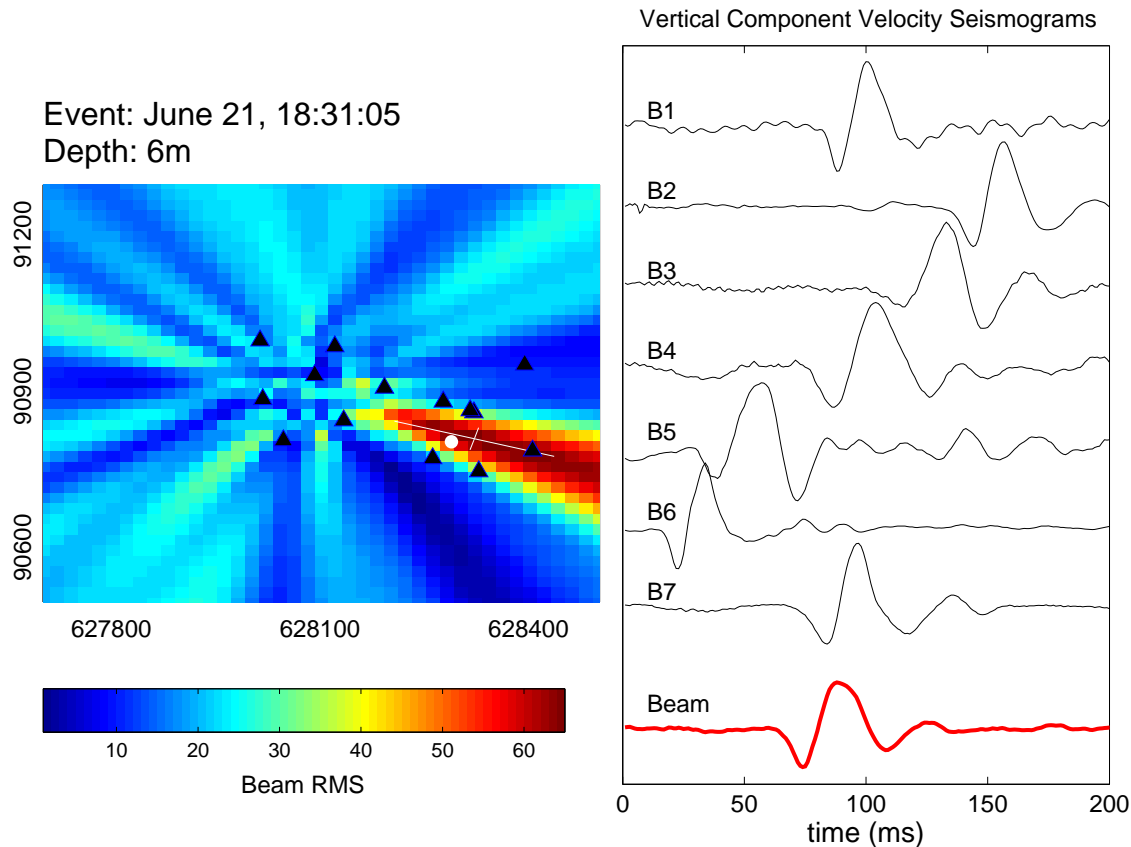


Figure 5.7: Epicentral location of a near-surface event as found by maximizing the RMS value of the beam (white cross bars). This method was developed by Roux (2008). Seismic stations are represented by triangles. The location calculated by arrival time inversion lies within the error bars of the beam-forming location. The vertical seismograms used in the beam-forming are dominated by the Rayleigh phase (right panel).

parameter.

5.3.1 Array Techniques: Future Work

Roux (2008) applied the beam-forming technique to the 2004 seismic data set using the circular-wavefront-geometry to find epicentral locations of near-surface icequakes. Figure 5.7 shows the result for a near-surface event which occurred near station A4 (see Figure 4.2 for the 2004 seismic array). This region of the glacier is of particular interest, as the surface crevasses frequently emit seismic energy. The white cross bars indicate the epicentral location determined by the beam-forming techniques. Within these error bars the RMS of the beam is at least 90 % of its maximum. The white dot gives the location determined by inverting hand-picked arrival times. As the event is located inside the eastern part of the seismic network, only the western stations were used ('B' stations). The vertical component velocity seismograms show a dominating Rayleigh wave.

The location determined by the beam-forming technique agrees well with the location calculated by arrival time inversion. This shows that array techniques can be used to determine approximate icequake locations. As the data sets of all years consist of between

30000 and 100000 events, array techniques are a useful tool to sort the catalogs by approximate icequake locations. As discussed in Section 5.2.7, the ambient noise likely is located at particular back azimuths. Hence, array-techniques could also be used to study the temporal and spatial evolution of noise sources, such as lake drainage channels.

Chapter 6

Conclusion

Seismic signals emitted by large bodies of ice have previously been studied in a variety of glaciological and seismological contexts. In the present work, I investigated seismic radiation emitted from small fractures within the glacier ice. These types of seismic events are commonly referred to as 'icequakes'. Two aspects of glacier seismicity were the focus of this thesis: 1) characterization of seismic sources in glacier ice and, 2) linking basal icequake activity to the subglacial hydrological conditions. The latter was of particular interest in the context of the annual drainage of the glacier-dammed lake Gornersee.

The seismic moment tensor was used to characterize selected icequake sources. I studied events that occurred near the surface, near the glacier bed and at intermediate depths. Due to the high degree of homogeneity of the glacier ice I was able to model the path using relatively simple Green's Functions. For the moment tensor inversions of near-surface and intermediate-depth events I generated Green's Functions for a homogeneous half space. For basal icequakes I furthermore used Green's Functions of a velocity model consisting of ice and underlying bedrock. The topography of the ice-bedrock interface was determined by radio-echo soundings.

I found two possible fracture modes: tensile and shear dislocations. Tensile faulting is consistent with the high density of surface crevasses within the study site. I estimate that this fracture mode is responsible for more than 99% of all events I recorded on Gornergletscher. The seismograms of intermediate icequakes can also be modelled with moment tensors representing this fracture mode. As these events were located at depths where the ice-overburden pressure is expected to inhibit tensile faulting, I concluded that the intermediate-depth icequakes are evidence for englacial water lenses or water flow reducing the effective stress. The events of a selected cluster of basal icequakes also had tensile fault mechanisms. This result is of pivotal importance, as it shows that these seismic signals are not produced by stick-slip motion but are the consequence of basal crevasse or hair fissure openings. Since the tensile fault planes of these sources were found to be near-horizontal, I cannot explain them by longitudinal stretching of the basal ice. I suggest that these events occur as the consequence of the rapid closure of draining water-filled cavities at the glacier base. These results indicate that throughout the glacier thickness, tensile faulting is the main fracturing mode. Additionally, I found a cluster of near-surface events whose sources are shear dislocations. Although only a dozen events with shear-faulting sources have been identified, this is an important result, as it shows that ice can also fail under shear straining.

In my study of fault mechanisms of basal icequakes I selected one cluster with particularly simple waveforms. Whereas there are more clusters with similar signal characteristics, a large number of basal icequakes with substantially different waveforms were also found. Some show less impulsive first arrivals, others are characterized by long coda. The latter feature may indicate the presence of seismic waves trapped near the glacier bed, water resonances or finite source properties. For such events, the seismic moment tensor may not be an adequate source representation. Another class of basal icequakes shows dilatational first arrivals at all recording azimuths indicating a collapsing crack as a source mechanism. The variety of signal characteristics points out the need for more source studies of basal icequakes.

Concerning the link between glacial seismicity and the outburst floods of Gornerssee I focused on temporal fluctuations in basal icequake activity. This has two main reasons: First, I expected the outburst flood to influence the basal seismicity. When the flood water is routed through the subglacial drainage system, the increasing basal water pressure leads to enhanced basal motion. The activity of basal icequake clusters does indeed correlate with basal water pressures as they tend to occur at low or decreasing water pressures. This suggests that these seismic signals are emitted during fracturing of the basal ice layer, which undergoes large deformation rates when the glacier couples to its bed after periods of water pressure-enhanced sliding. As an alternative explanation I further suggest that basal icequakes are a consequence of drastic ice deformation above closing water-filled cavities. The second reason for the study of basal icequakes is their tendency to cluster in distinct locations. This contributes to high signal correlations among the events of a single cluster, which was used in cross-correlation searches of the seismic catalog to find more cluster events. As such cross-correlation searches are robust with respect to seismic background noise, which increases during the warm hours of the day, I was able to identify and locate basal icequakes which had been missed by trigger algorithms or signal discriminators.

I therefore established a link between fracture processes within Gornergletscher and the outburst floods of Gornerssee. Somewhat contrary to my expectations, I found that the lake drainage inhibits basal seismicity rather than favoring it. On the other hand, I did not find evidence for hydrofracturing, the process by which material fracturing occurs because pressurized water within the glacier reduces the effective pressure to allow for the extension of tensile cracks. This can occur even at depths where in the absence of water the compressive hydrostatic pressure within the ice is high enough to suppress tensile fractures. I still consider it likely that hydrofractures occur during the englacial and subglacial routing of the large amounts of flood water or during calving events. The presence of tensile seismic sources at intermediate depths is a strong indicator for hydrofracturing. However, in view of the basal icequake activity, the results indicate that fracturing as a consequence of changes in glacier sliding more effectively emits seismic energy than hydrofracturing. In general, I certainly acknowledge that seismic evidence of hydrofracturing may have been recorded during the seismic field campaigns. However, the signals may not have triggered the detection algorithms, either because they lacked impulsive first arrivals or because they were too weak. Another possibility is also that substantial hydrofracturing may occur at the onset of the lake drainage, when the surface seismicity increases, too, thus masking other types of seismic signals. In conclusion, I state that although I could link the basal seismic activity to the lake drainage, I did not identify a burst of seismicity that could be associated with the breaching of a seal initiating the

lake drainage. Whereas I could infer some interesting insights into fracture processes at the surface, within the glacier and near the bed from passive seismic records, more such research efforts are necessary to develop an acquisition and processing technique of the seismic data to allow for an early warning system for outbursts of glacier-dammed lakes.

Appendix A

Decomposition of Tensile Crack Moment Tensor

The moment density tensor of a tensile opening in the z-plane ('crack' moment density tensor) m^{crack} is given by

$$m^{\text{crack}} = \begin{bmatrix} \lambda D_{\perp} & 0 & 0 \\ 0 & \lambda D_{\perp} & 0 \\ 0 & 0 & (\lambda + 2\mu) D_{\perp} \end{bmatrix}, \quad (\text{A.1})$$

where D_{\perp} is the fault normal slip and λ and μ are the Lamé moduli (Aki and Richards, 2002, p. 51). To get the moment tensor M^{crack} , the expression in Equation A.1 has to be multiplied by the fault area S . Thus, using $\nu = \lambda/(2(\lambda + \mu))$, where ν is the Poisson's ratio, we obtain

$$M^{\text{crack}} = M_0^{\text{crack}} \begin{bmatrix} 1 & 0 & 0 \\ 0 & 1 & 0 \\ 0 & 0 & (\frac{1}{\nu} - 1) \end{bmatrix}, \quad (\text{A.2})$$

where $M_0^{\text{crack}} = \lambda S D_{\perp}$. An important implication of Equation A.2 is that the Poisson's ratio of the material surrounding the source determines the relative strengths of the components of the diagonalized moment tensor, namely $1 : 1 : \frac{1}{\nu} - 1$. This is not the case for double-couple or explosion sources, for instance. M^{crack} can be decomposed as follows:

$$\begin{bmatrix} 1 & 0 & 0 \\ 0 & 1 & 0 \\ 0 & 0 & (\frac{1}{\nu} - 1) \end{bmatrix} = \frac{1}{3}(\frac{1}{\nu} + 1) \begin{bmatrix} 1 & 0 & 0 \\ 0 & 1 & 0 \\ 0 & 0 & 1 \end{bmatrix} + \frac{1}{3}(\frac{1}{\nu} - 2) \begin{bmatrix} -1 & 0 & 0 \\ 0 & -1 & 0 \\ 0 & 0 & 2 \end{bmatrix} \quad (\text{A.3})$$

Equation A.3 shows that the moment tensor of a tensile crack in the z-direction is a linear combination of an isotropic moment tensor and a CLVD that has its major axis in the z-direction. The relative strength of the two depends on the Poisson's ratio of the material surrounding the source. For $\nu = 0.36$, the value used in this study, the isotropic component is almost 5 times bigger than the CLVD.

Appendix B

Results of Moment Tensor Inversion of Chapter 2

Table B.1: Summary of moment tensor solutions for all inversions presented in Chapter 2. For each event the first, second and third lines correspond to the full, deviatoric and the crack+DC inversions, respectively. Moment tensors are given in 10^6 Nm.

Event	M_{xx}	M_{yy}	M_{zz}	M_{xy}	M_{xz}	M_{yz}	M_0
SURF_A 1	2.87	3.93	2.40	-0.75	0.15	-0.72	4.55
	6.62	1.84	-2.51	-0.78	0.07	-0.77	2.34
	2.36	3.47	1.76	-0.83	1.46	-0.70	4.12
SURF_A 2	0.95	1.32	1.10	-0.16	-0.06	0.12	1.43
	0.14	0.56	-0.69	-0.17	-0.09	0.09	0.63
	0.73	1.11	0.71	-0.16	-0.05	0.15	1.22
SURF_A 3	3.73	4.99	4.53	-0.62	-0.27	0.41	5.49
	0.56	1.99	-2.54	-0.66	-0.38	0.34	2.29
	2.72	4.01	2.57	-0.66	-0.19	0.45	4.41
SURF_A 4	1.28	1.82	1.50	-0.23	-0.24	0.14	2.00
	0.18	0.77	-0.95	-0.24	-0.28	0.12	0.88
	0.90	1.48	0.91	-0.24	-0.15	0.24	1.67
SURF_A 5	2.98	4.05	3.69	-0.54	-0.25	-0.08	4.27
	0.41	1.62	-2.03	-0.57	-0.34	-0.14	1.84
	1.99	3.11	1.80	-0.59	-0.07	0.05	3.37
SURF_B 1	1.49	-5.24	-1.26	-1.47	-1.67	6.41	2.61
	2.66	-4.10	1.44	-1.45	-1.64	0.66	4.10
	2.09	-4.14	0.25	-1.44	-1.38	0.52	3.14
SURF_B 2	1.26	-4.07	-0.75	-1.22	-1.17	1.03	2.18
	2.09	-3.26	1.17	-1.21	-1.14	1.05	3.25
	1.42	-3.46	-0.36	-1.18	-0.83	0.96	2.13
SURF_B 3	0.12	-0.74	-0.28	-0.36	-0.18	0.16	0.34
	0.33	-0.54	0.21	-0.36	-0.18	0.17	0.59
	0.16	-0.64	-0.12	-0.35	-0.11	0.15	0.34
SURF_B 4	0.81	-4.02	-0.97	-1.62	-1.58	1.31	2.40
	1.78	-3.07	1.29	-1.60	-1.56	1.33	3.74
	1.23	-3.29	2.61	-1.54	-1.13	1.28	2.64
SURF_B 5	0.41	-3.71	-1.32	-1.28	-1.12	0.69	1.38
	1.49	-2.66	1.18	-1.26	-1.09	0.70	2.80
	0.41	-3.71	-1.32	-1.28	-1.12	0.69	1.38
INT 1	0.654	0.740	0.599	-0.103	0.037	-0.064	0.832
	-0.012	0.082	-0.070	-0.110	0.021	-0.071	0.173
	0.402	0.517	0.400	-0.097	0.054	-0.095	0.625
INT 2	0.781	0.839	0.689	-0.130	0.069	-0.080	0.982
	-0.009	0.078	-0.087	-0.136	0.049	-0.088	0.216
	0.565	0.675	0.500	-0.153	0.067	-0.095	0.824
INT 3	0.641	0.638	0.544	-0.154	0.076	-0.087	0.839
	0.032	0.036	-0.068	-0.158	0.060	-0.094	0.232
	0.588	0.600	0.492	-0.152	0.085	-0.089	0.796

Appendix C

Moment Tensor Inversion Scheme Using Vector Dipoles

This appendix presents some details of how Equation 3.2 is transformed into a discrete numerical inversion scheme. For variable definitions, the reader is referred to Chapter 3.4.1. A seismic source represented by a moment tensor with elements M_{pq} induces the following ground displacement $u_n(\mathbf{x}, t)$ at point \mathbf{x} and time t :

$$u_n(\mathbf{x}, t) = M_{pq}(t) * G_{np,q}(\mathbf{x}, t). \quad (\text{C.1})$$

Using the manipulations described in Chapter 3.4.1, we obtain

$$u_n(\mathbf{x}, t) = \bar{G}_{ni}(\mathbf{x}, t) \times M_i. \quad (\text{C.2})$$

Here, the time dependence of the seismic moment tensor $M_{pq}(t)$ was moved to the terms $\bar{G}_{ni}(\mathbf{x}, t)$, which are consequently the convolution of the original Green's Functions $G_{np,q}(\mathbf{x}, t)$ and the source time function. The indices of (p, q) of $M_{pq}(t)$ were mapped into the index i of M_i as follows:

$$\begin{aligned} (p, q) = (1, 1) &\rightarrow i = 1 \\ (p, q) = (1, 2) &\rightarrow i = 2 \\ (p, q) = (1, 3) &\rightarrow i = 3 \\ (p, q) = (2, 2) &\rightarrow i = 4 \\ (p, q) = (2, 3) &\rightarrow i = 5 \\ (p, q) = (3, 3) &\rightarrow i = 6 \end{aligned} \quad (\text{C.3})$$

We call the terms $\bar{G}_{ni}(\mathbf{x}, t)$ 'Green's Functions'. They constitute the seismic responses to vector dipoles. In the present work they were computed with the software packages FKRPROG (Saikia, 1994), reflectivity (Müller, 1985) and fd3d (Olsen, 1994). Equation C.2 holds for each sample in a seismogram. If the seismogram consists of k data points, we can write Equation C.2 in matrix form as

$$\begin{bmatrix} u_x^1 \\ u_x^2 \\ \vdots \\ u_x^k \\ \\ u_y^1 \\ u_y^2 \\ \vdots \\ u_y^k \\ \\ u_z^1 \\ u_z^2 \\ \vdots \\ u_z^k \end{bmatrix} = \begin{bmatrix} g_x^{xx,1} & g_x^{xy,1} & g_x^{xz,1} & g_x^{yy,1} & g_x^{yz,1} & g_x^{zz,1} \\ g_x^{xx,2} & g_x^{xy,2} & g_x^{xz,2} & g_x^{yy,2} & g_x^{yz,2} & g_x^{zz,2} \\ \vdots & \vdots & \vdots & \vdots & \vdots & \vdots \\ g_x^{xx,k} & g_x^{xy,k} & g_x^{xz,k} & g_x^{yy,k} & g_x^{yz,k} & g_x^{zz,k} \\ \\ g_y^{xx,1} & g_y^{xy,1} & g_y^{xz,1} & g_y^{yy,1} & g_y^{yz,1} & g_y^{zz,1} \\ g_y^{xx,2} & g_y^{xy,2} & g_y^{xz,2} & g_y^{yy,2} & g_y^{yz,2} & g_y^{zz,2} \\ \vdots & \vdots & \vdots & \vdots & \vdots & \vdots \\ g_y^{xx,k} & g_y^{xy,k} & g_y^{xz,k} & g_y^{yy,k} & g_y^{yz,k} & g_y^{zz,k} \\ \\ g_z^{xx,1} & g_z^{xy,1} & g_z^{xz,1} & g_z^{yy,1} & g_z^{yz,1} & g_z^{zz,1} \\ g_z^{xx,2} & g_z^{xy,2} & g_z^{xz,2} & g_z^{yy,2} & g_z^{yz,2} & g_z^{zz,2} \\ \vdots & \vdots & \vdots & \vdots & \vdots & \vdots \\ g_z^{xx,k} & g_z^{xy,k} & g_z^{xz,k} & g_z^{yy,k} & g_z^{yz,k} & g_z^{zz,k} \end{bmatrix} \begin{bmatrix} m_{xx} \\ m_{xy} \\ m_{xz} \\ m_{yy} \\ m_{yz} \\ m_{zz} \end{bmatrix} \quad (\text{C.4})$$

For the data seismogram u_n^j as well as for the Green's Functions $g_n^{pq,j}$, the index j labels the sample and the index n denotes the component. At each sample the columns of the matrix on the right hand side of Equation C.4 contain one of the six unique vector dipole responses. Specifically, $g_n^{pq,j}$ is the n^{th} -component synthetic ground displacement in response to a moment tensor whose (p, q) -element is unity, whereas all other elements are zero. As the waveforms that are used in moment tensor inversions usually consist of 100 samples or more, the system of equations shown in Equation C.4 is generally well overdetermined.

Appendix D

Overview of Seismic Measurements

D.1 Seismic Networks

Table D.1: Operational periods of the 2004, 2005, 2006 and 2007 seismometer networks.

Year	Time of Deployment	Installation and Supervision
2004	June 15 - July 8	N. Deichmann
2005	June 7 - July 7	N. Deichmann, F. Walter
2006	May 29 - July 28	N. Deichmann, F. Walter
2007	May 28 - July 22	F. Walter

This appendix provides an overview of the seismic field campaigns on Gornergletscher in the summers 2004, 2005, 2006 and 2007. The networks consisted of a setup usually applied to active seismology: The seismometers were connected to one, two or three seismographs ('Geodes' by Geometrics), one of which, the 'master Geode', was connected to a recording laptop. Synchronization was provided by the Geodes, whereas absolute time was given by the laptop clock. Most instruments were Lennartz LE-3D seismometers, which were placed on the glacier surface and had to be aligned every day. We also installed borehole seismometers (Geospace GS-11D and Geospace GS-20D). Only for the 2005 data have we made an effort to align these instruments retrospectively applying coordinate rotations to the horizontal components.

The seismometer locations were measured with GPS at least once during a field season. In Figures D.1, D.2, D.3 and D.4 the seismometer locations are indicated by green triangles on top of ortho-photographs. At locations of large dotted triangles a surface seismometer and a deep borehole seismometer were installed. The blue line represents the outline of Gornersee at its maximum level in the corresponding year. Exact locations and types of seismometers are listed in Tables E.1 and E.2. The seismic network of 2005 was installed about 1 km downglacier of the networks of 2004, 2006 and 2007, which were located near Gornersee.

The operational periods were chosen around the lake drainages and are listed in Table D.1. In 2004, the seismic measurements were terminated once the lake had emptied. In

2005 the lake drained unexpectedly early. The seismic installation was just finished, but other glaciological measurement had not been set up. Seismic records for an extended time period after the lake drainage are also available for 2006 and 2007.

2004 Network

In 2004 the network consisted of 13 surface (Lennartz LE-3D) and 1 borehole seismometer (Geospace GS-20D), which were operational for 3-4 weeks in trigger mode. In addition, continuous recording was made with one seismometer and a Taurus seismograph. In order to determine seismic velocities, shallow as well as borehole shots were recorded at a number of locations. The lake outburst started on July 2 and was rather drastic involving surface drainage, subglacial drainage as well as ice dam flotation (Huss, 2005; Huss et al., 2007; Sugiyama et al., 2007; Sugiyama et al., 2008).

2005 Network

In 2005 the network consisted of 13 surface (Lennartz LE-3D), 6 shallow borehole seismometers (Geospace GS-11D) and 3 deep borehole seismometers (Geospace GS-20D), which were operational for about 1 month in trigger mode. The lake started to drain subglacially on June 9 when it was only half filled (Huss et al., 2007; Werder et al., 2009a) at the beginning of the field campaign. Hence, most seismic recording was done after the lake drainage. The 2005 network was placed into a region of high surface seismicity as had been previously identified in the 2004 data. In order to determine seismic velocities, shallow as well as borehole shots were recorded at a number of locations. The results showed a slow seismic velocity layer near the surface. This was investigated and documented in a Semesterarbeit by Valentin Gischig in 2005.

2006 Network

The seismic network of 2006 was the largest one consisting of 15 surface (Lennartz LE-3D), 6 shallow borehole seismometers (Geospace GS-11D) and 3 deep borehole seismometers (Geospace GS-20D), which were operational for about 2 month in trigger mode. In addition to the passive seismic monitoring, a comprehensive active seismic investigation was conducted (Gischig, 2007): An arrival time-based seismic tomography study was performed based on surface as well as borehole profiles. Furthermore, we set off explosives in the moulin that the lake drained into to determine the passage of the lake water as it enters into the subglacial drainage system. In 2006 the lake drained rather slowly over the course of several weeks, because it overflowed superficially into a moulin (Chapter 4.2). The overflow began on July 5 (Werder and Funk, 2009b).

2007 Network

The seismic network of 2007 was the smallest one consisting of 7 shallow borehole seismometers (Geospace GS-11D and Geospace GS-20D) and 1 deep borehole seismometer

(Geospace GS-20D), which were operational for close to 2 months. The instruments were run in continuous mode with the goal to confirm or disprove the findings of the 2004 and 2006 networks concerning the activity of basal icequake clusters. This is further explained in Chapter 5.2. Starting on July 4 the lake first drained into a borehole and a moulin via the glacier surface. On July 8 the intraglacial and/or subglacial drainage began (Werder et al., 2009a).

D.2 Seismic Data

Table D.2: Approximate data volume.

Year	Number of files	Bytes per file	Bytes total	Record length
2004	35000	165 KB	5.8 GB	2.0 sec
2005	72000	200 KB	14.4 GB	1.5 sec
2006	52000	2000 KB	104.0 GB	1.5-2.0 sec
2007 (trig)	103000	87 KB	89.6 GB	2.0 sec
2007 (cont)	607000	954 KB	579.1 GB	10.0 sec

An overview of the seismic data volume is given in Table D.2. The raw data format as written during recording with the Geodes is called 'seg'. This data was usually converted into gse2 format (Appendix F), which was then used in the data analysis. In the years 2004, 2005 and 2006 the instruments recorded in trigger mode, whereas in 2007 they recorded continuously (Chapter 5.2). As part of the analysis, the continuous data of 2007 was post-triggered. The algorithm of this post-trigger and the trigger algorithm for the 2004-2006 data are both based on an STA/LTA method. However, unlike for the 2004-2006 data, the 2007 data does not simply compute the ratio of the STA and LTA windows. For more specific information on the post triggering see the source code of N. Deichmann's FORTRAN code seg2marstrig. Table D.3 summarizes the recording specifications of all years. Details of the STA/LTA trigger algorithm applied to the 2004-2006 data as well as definitions of the variables listed in Table D.3 can be found in Chapter 4.3.

As this thesis was focused on deep seismic events, only a small portion of the recorded seismograms has been analyzed. In 2004 and 2006 we searched the data set for basal icequakes in some detail. For the 2004 data, we have also applied array techniques to automatically locate surface events (Chapter 5.3). This is an ongoing effort. The data in 2005 has been scrutinized the least. The waveform discriminator identified a number of deep icequakes, however none of them were located at the glacier base. It is not clear if basal icequakes in the region of the 2005 array do not exist or if the glacier is too thick at that location to allow for recording of basal seismicity at the glacier surface. As the 2005 network was located in a region of high surface seismicity, the 2005 data may prove valuable when analyzing near-surface icequake sources further.

Table D.3: Recording specifications and parameters of the STA/LTA trigger. In 2007 the data was recorded continuously and then post triggered using the program `seg2marstrig` with the command line options: `'seg2marstrig fl:filist st:80 lt:800 er:4 up:8 po:1'`. This algorithm is different from the one used in 2004, 2005 and 2006.

	2004	2005	2006	2007
Sampling Frequency	1000 Hz	1000 Hz	4000 Hz	1000 Hz
threshold ratio	10	20	20	4
n_{trig}	4	10	10	7
t_{rec}	2 s	1.5 s	1 s	2 s
t_{pre}	0.5 s	0.5 s	0.4-0.5 s	0.5 s

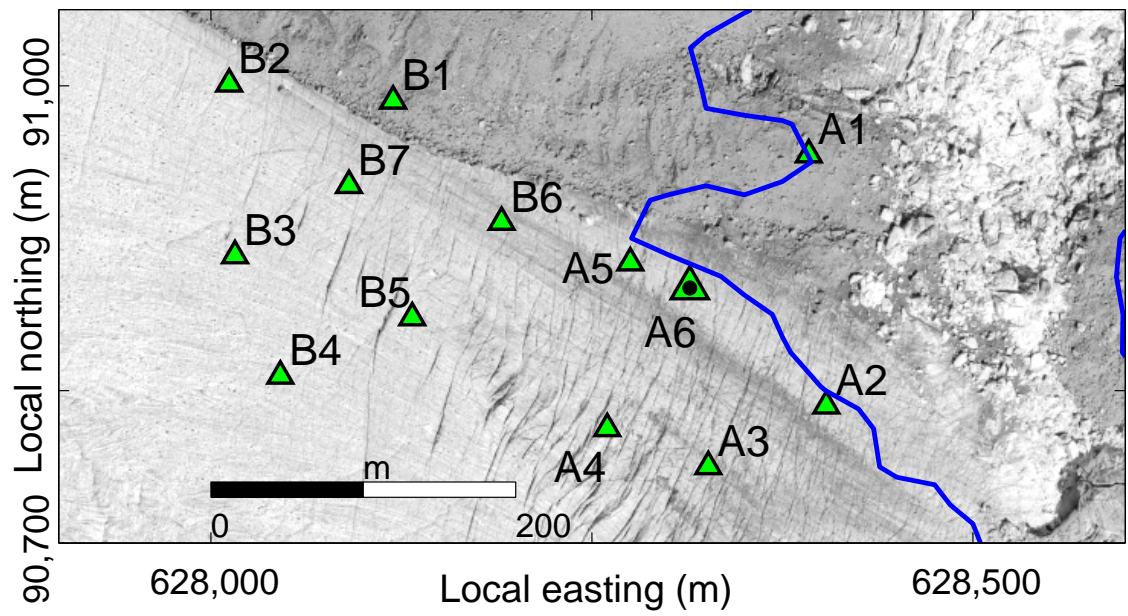


Figure D.1: 2004 seismic network.

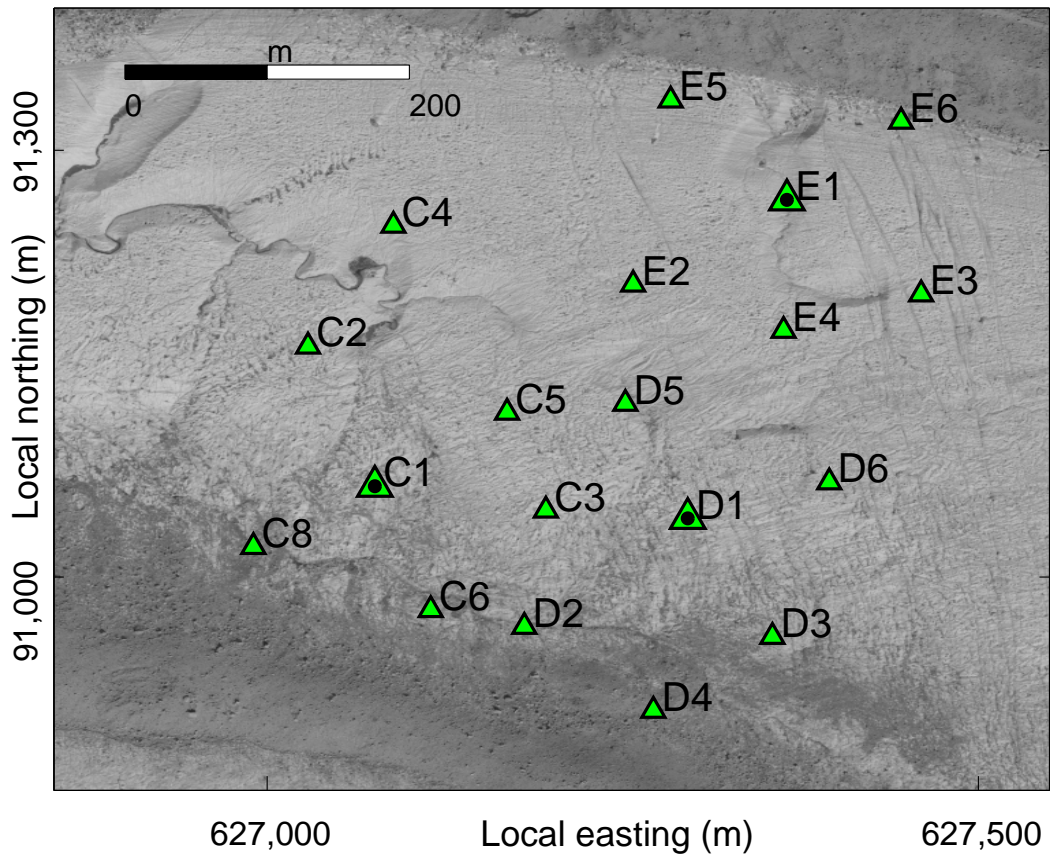


Figure D.2: 2005 seismic network.

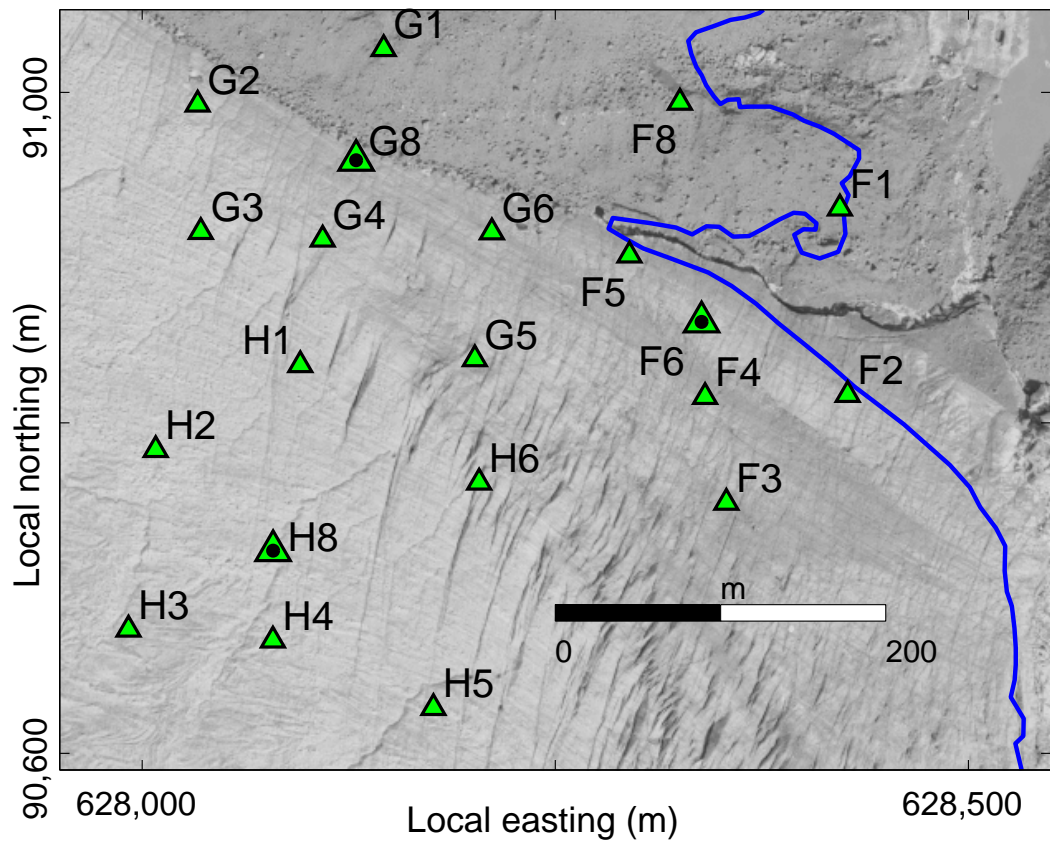


Figure D.3: 2006 seismic network.

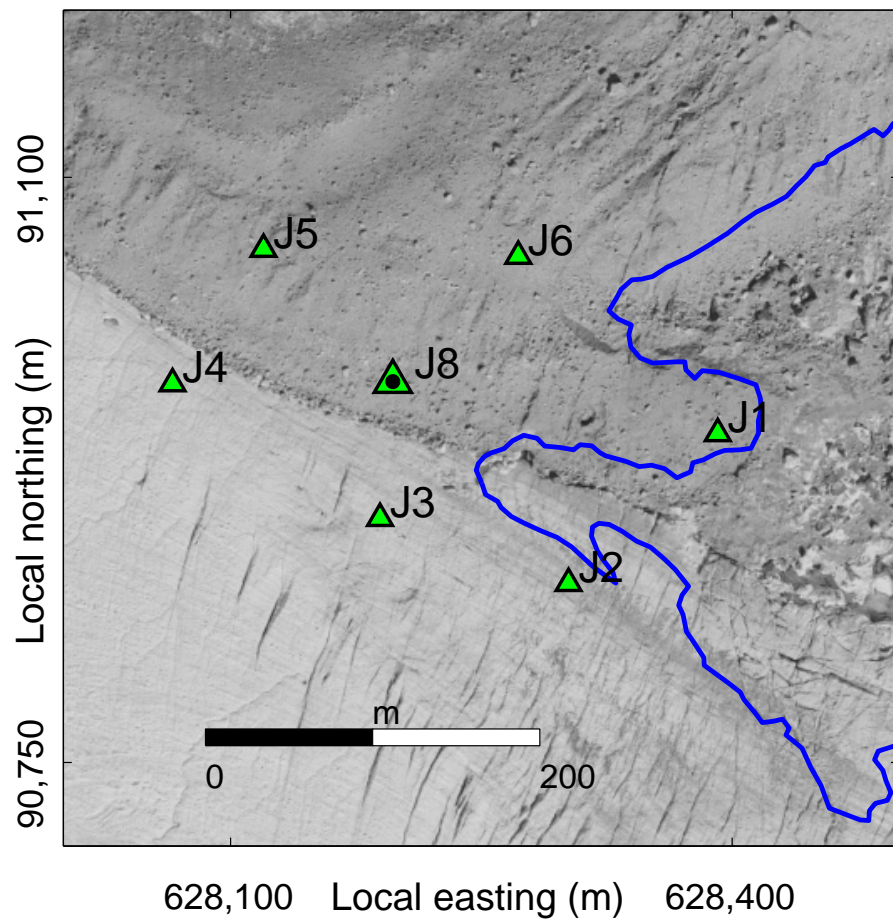


Figure D.4: 2007 seismic network.

Appendix E

Instrumentation

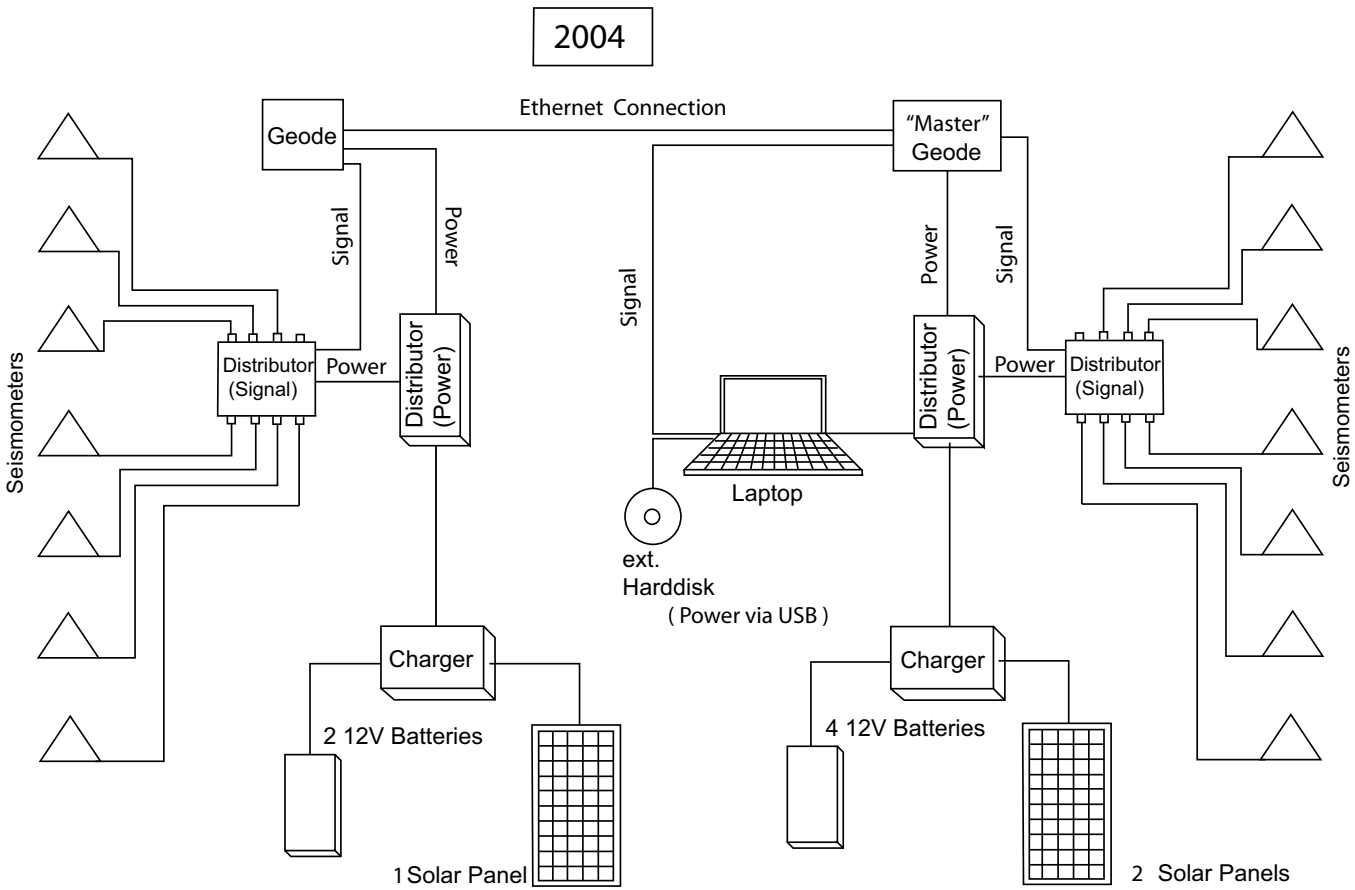


Figure E.1: 2004 seismic setup.

2005

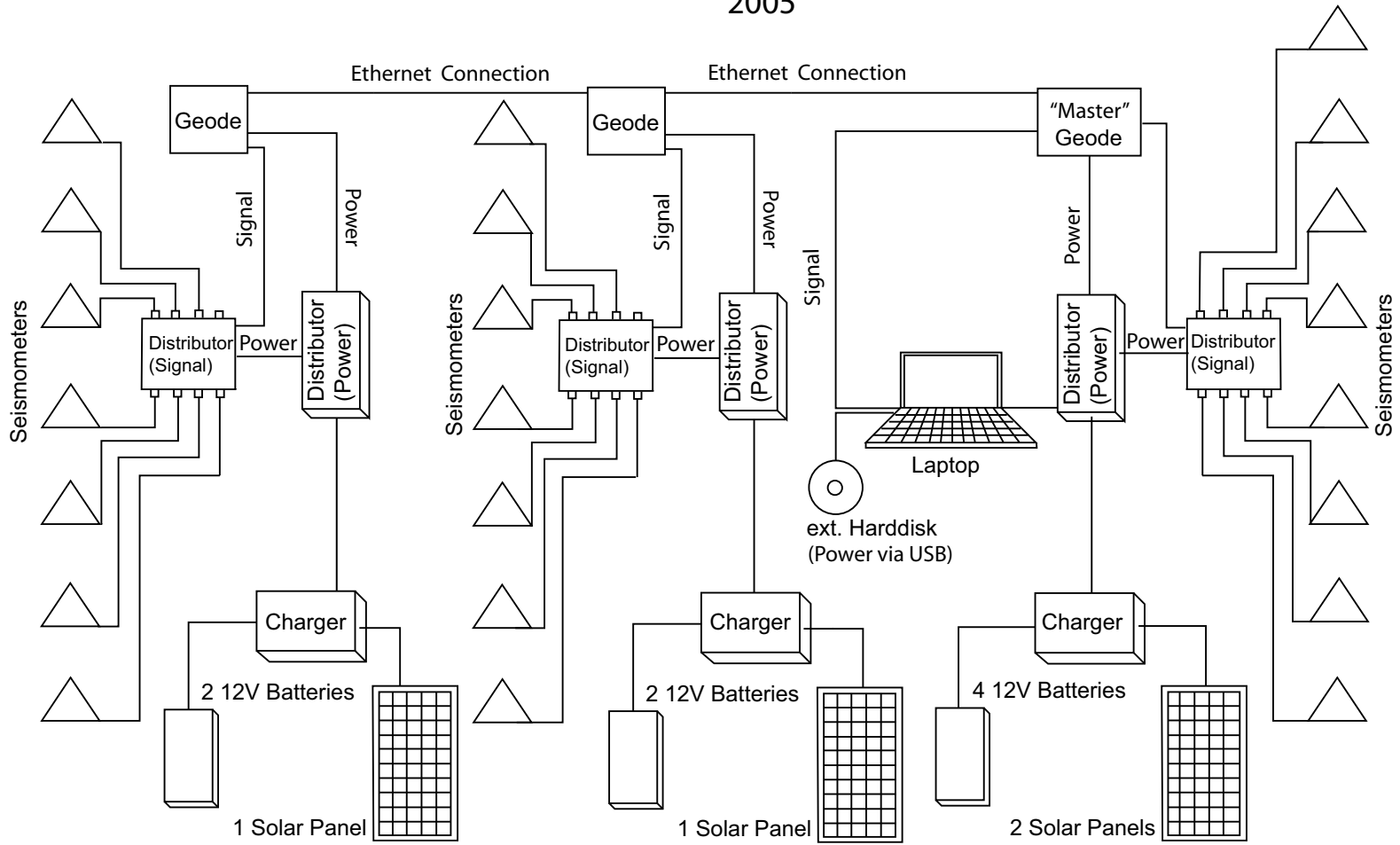


Figure E.2: 2005 seismic setup.

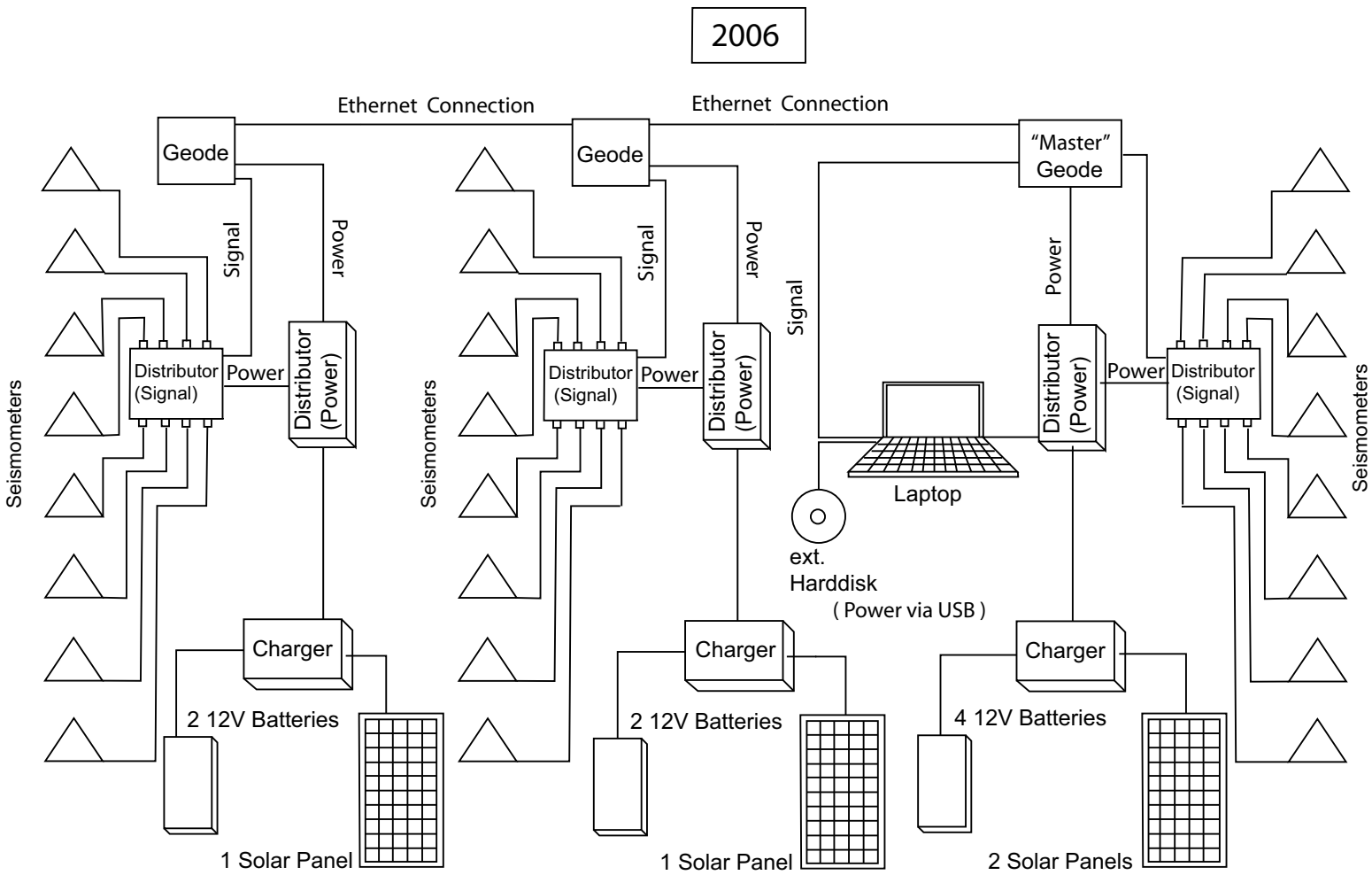


Figure E.3: 2006 seismic setup.

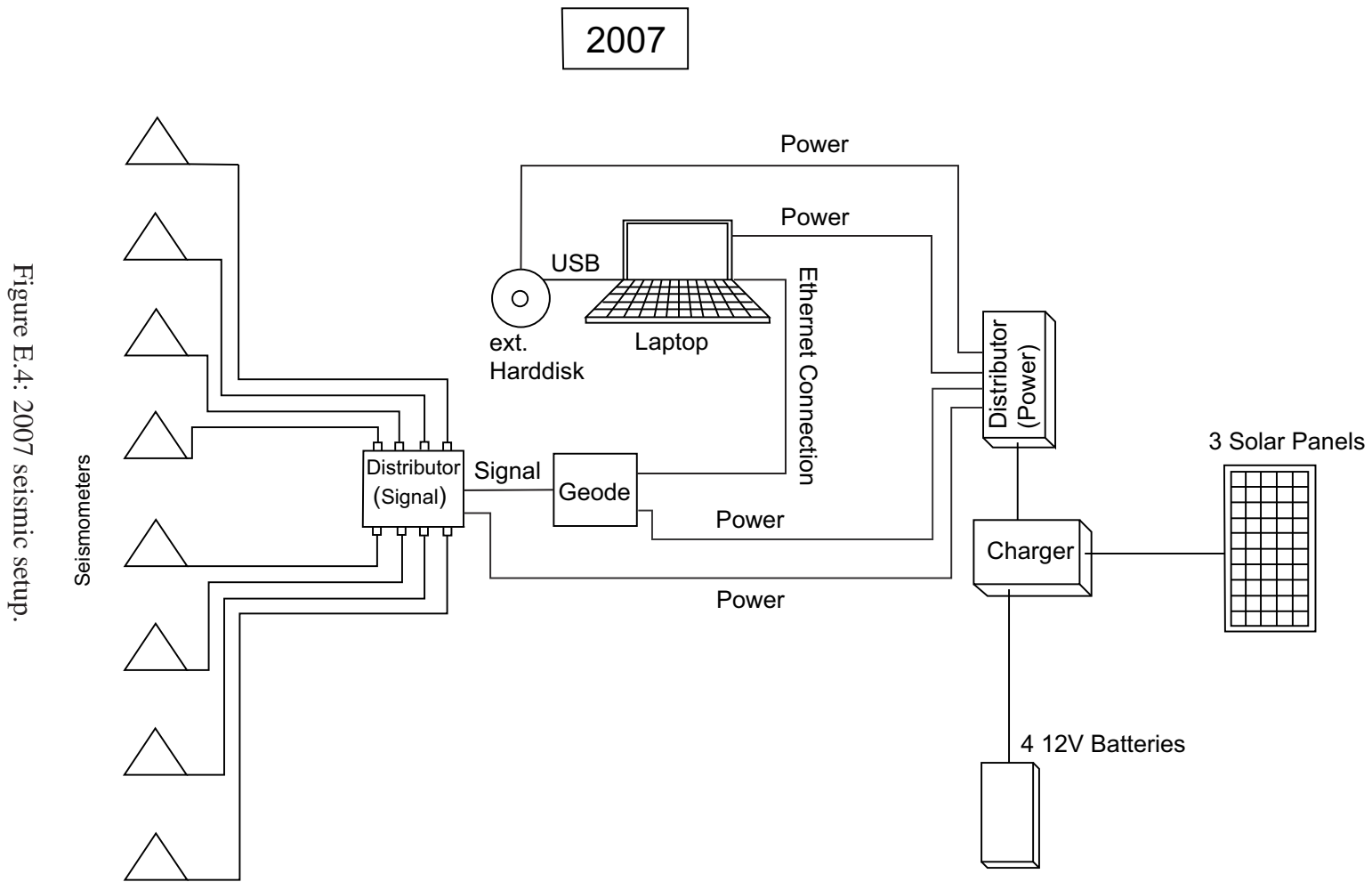


Figure E.4: 2007 seismic setup.

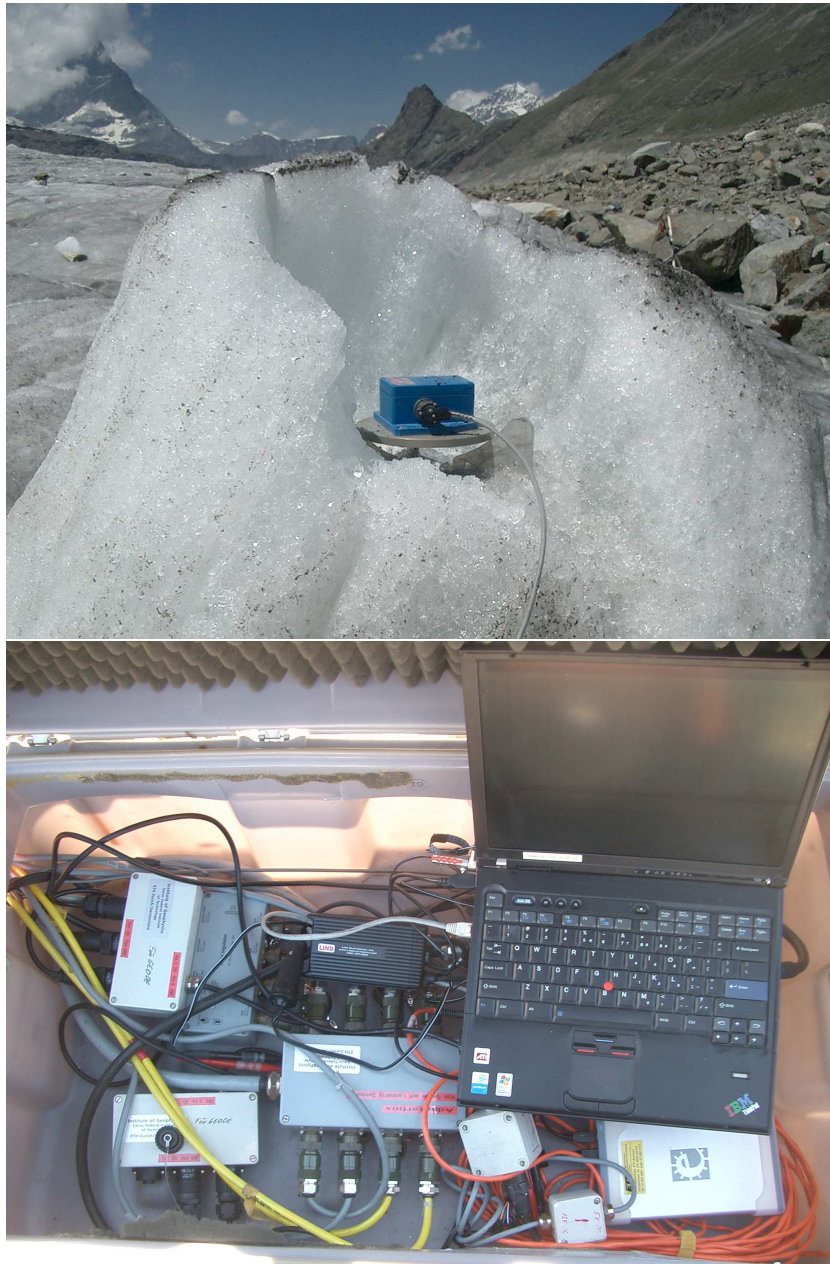


Figure E.5: Upper: Lennartz LE-3D seismometer installed on the glacier ice. These instruments were placed on tripods into small depressions dug with an icepick. They were subsequently covered by a tarpaulin. This reduced in the ablation around the seismometer and over the course of a few weeks the instruments were located on bumps as can be seen in the picture. Lower: Plastic box that contained the recording devices, including the master Geode located under the laptop.

E.1 Specification of Selected Components

- Gel Solar batteries, 12 V, 65Ah capacity, used in 2004, 2005 and 2007
- DC/DC converter (12 V to 15 V) for Laptop (LIND Automobile Adapter Model # CF-LND80S LG)
- DC/DC converter (12 V to 5 V) for external hard disk
- External hard disks
 - 2004,2005: Icy Box
 - 2006: SPD5210CC by Philips (80 GB)
 - 2007: Elements (500 GB)
- Seismograph: Geode Ultra-Light Exploration Seismograph (by Geometrics)
- Solar Panels: 110W Siemens SM110

E.2 Seismometer Specification

Table E.1: Seismometer specifications for 2004 (Figure D.1) and 2005 (Figure D.2) networks. Swiss Grid coordinates are given.

ID	Year	Make	Easting	Northing	Elevation
G4A1	2004	Lennartz LE-3D	628392.3	90954.9	2537.6
G4A2	2004	Lennartz LE-3D	628403.8	90790.0	2538.3
G4A3	2004	Lennartz LE-3D	628326.4	90750.3	2545.3
G4A4	2004	Lennartz LE-3D	628260.0	90775.2	2547.3
G4A5	2004	Lennartz LE-3D	628275.2	90883.9	2539.2
G4A6	2004	Lennartz LE-3D	628319.3	90863.4	2540.2
G4A7	2004	Geospace GS-20D	628314.2	90867.3	2439.3
G4B1	2004	Lennartz LE-3D	628119.5	90990.1	2541.7
G4B2	2004	Lennartz LE-3D	628012.0	91001.3	2542.4
G4B3	2004	Lennartz LE-3D	628015.7	90888.6	2547.9
G4B4	2004	Lennartz LE-3D	628045.5	90809.7	2550.9
G4B5	2004	Lennartz LE-3D	628132.1	90847.9	2547.3
G4B6	2004	Lennartz LE-3D	628190.7	90910.6	2539.1
G4B7	2004	Lennartz LE-3D	628090.6	90934.7	2543.7
G5C1	2005	Geospace GS-20D	627075.7	91063.8	2377.6
G5C2	2005	Geospace GS-11D	627028.7	91162.2	2507.8
G5C3	2005	Geospace GS-11D	627195.9	91046.8	2514.1
G5C4	2005	Lennartz LE-3D	627088.7	91247.1	2515.8
G5C5	2005	Lennartz LE-3D	627168.6	91115.7	2513.7
G5C6	2005	Lennartz LE-3D	627115.0	90976.9	2512.6
G5C7	2005	Lennartz LE-3D	627085.2	91066.7	2519.1
G5C8	2005	Lennartz LE-3D	626990.3	91021.2	2503.1
G5D1	2005	Geospace GS-20D	627295.7	91041.2	2245.4
G5D2	2005	Geospace GS-11D	627180.8	90965.1	2509.2
G5D3	2005	Geospace GS-11D	627355.3	90958.1	2521.5
G5D4	2005	Lennartz LE-3D	627271.5	90906.1	2519.2
G5D5	2005	Lennartz LE-3D	627251.9	91121.9	2519.9
G5D6	2005	Lennartz LE-3D	627395.2	91066.7	2526.4
G5D7	2005	Lennartz LE-3D	627308.1	91039.6	2526.0
G5E1	2005	Geospace GS-20D	627365.4	91265.2	2482.6
G5E2	2005	Geospace GS-11D	627257.3	91205.7	2515.3
G5E3	2005	Geospace GS-11D	627459.8	91198.8	2521.8
G5E4	2005	Lennartz LE-3D	627363.1	91173.2	2524.9
G5E5	2005	Lennartz LE-3D	627283.7	91335.2	2516.7
G5E6	2005	Lennartz LE-3D	627445.8	91320.3	2520.1
G5E7	2005	Lennartz LE-3D	627362.8	91275.2	2523.2

Table E.2: Seismometer specifications for 2006 (Figure D.3) and 2007 (Figure D.4) networks. Swiss Grid coordinates are given.

ID	Year	Make	Easting	Northing	Elevation
G6F1	2006	Geospace GS-11D	628422.2	90929.8	2525.2
G6F2	2006	Geospace LE-3D	628426.9	90817.0	2530.4
G6F3	2006	Geospace GS-11D	628353.5	90751.8	2534.9
G6F4	2006	Lennartz LE-3D	628340.7	90815.8	2535.6
G6F5	2006	Lennartz LE-3D	628294.9	90901.4	2531.2
G6F6	2006	Lennartz LE-3D	628340.1	90867.7	2533.7
G6F7	2006	Lennartz GS-20D	628338.5	90861.1	2492.2
G6F8	2006	Lennartz LE-3D	628325.4	90993.9	2532.9
G6G1	2006	Geospace LE-3D	628146.1	91026.3	2546.0
G6G2	2006	Geospace LE-3D	628033.5	90992.8	2536.7
G6G3	2006	Geospace GS-11D	628035.5	90915.6	2538.0
G6G4	2006	Lennartz LE-3D	628109.2	90911.1	2539.3
G6G5	2006	Lennartz GS-11D	628201.3	90838.6	2534.5
G6G6	2006	Lennartz LE-3D	628211.6	90915.4	2533.6
G6G7	2006	Lennartz GS-20D	628129.5	90958.9	2389.1
G6G8	2006	Lennartz LE-3D	628124.9	90955.5	2533.7
G6H1	2006	Geospace GS-11D	628095.7	90835.0	2540.9
G6H2	2006	Geospace LE-3D	628008.1	90783.7	2549.5
G6H3	2006	Geospace LE-3D	627991.7	90675.0	2550.8
G6H4	2006	Lennartz LE-3D	628079.1	90668.4	2553.8
G6H5	2006	Lennartz GS-11D	628176.2	90627.6	2548.2
G6H6	2006	Lennartz LE-3D	628203.9	90764.0	2544.7
G6H7	2006	Lennartz GS-20D	628079.2	90722.7	2301.2
G6H8	2006	Lennartz LE-3D	628076.0	90716.1	2552.1
G7J1	2007	Geospace GS-11D	628391.4	90946.7	2527.9
G7J2	2007	Geospace GS-11D	628302.2	90857.1	2527.4
G7J3	2007	Geospace GS-20D	628189.4	90896.0	2529.5
G7J4	2007	Lennartz GS-11D	628065.3	90976.6	2528.8
G7J5	2007	Lennartz LE-11D	628119.7	91057.0	2539.7
G7J6	2007	Lennartz LE-11D	628272.1	91052.8	2543.9
G7J7	2007	Lennartz GS-20D	628197.0	90977.7	2412.5
G7J8	2007	Lennartz GS-11D	628204.1	90979.0	2533.3

Appendix F

Description of Software

In this appendix we list and briefly explain some of the software packages and Matlab scripts that were used or developed in the course of the present work.

F.1 Data Processing

- **seg2gse2** by N. Deichmann. This FORTRAN program was used to convert the raw triggered data (seg) into gse2 format. For the 2007 continuous data, the trigger program seg2marstrig and the cross-correlation search seg2xcor were directly applied to the raw seg data.
- **gse2matrix** by N. Deichmann. This FORTRAN program can be used to convert gse2 data into ascii format, which can then be easily loaded into Matlab.
- **seg2marstrig** by N. Deichmann. This FORTRAN program was used to trigger the 10 s continuous data from 2007. It is applied to the raw seg data. The output is then processed by the Matlab script analyse_triggers.m, whose output is used by the FORTRAN program seg2gse2 to produce the triggered data set. In order to tune the trigger conditions, the Matlab script mars88trig.m is helpful.
- **Seismic Analysis Code (SAC)** by the University of California. This package is used by the moment tensor inversion packages for data processing such as filtering, interpolating and integrating time series. Besides its own format SAC can read other formats such as gse and ascii data. However, saving data from SAC in a format other than its own is very difficult according to my experience. I usually called SAC from PERL or shell scripts to automate processing. Straightforward Matlab routines to read and write SAC data are available.
- **gorsignals** by N. Deichmann. This FORTRAN program can be used to find maximum values in a seismogram. Together with the Matlab script findspikes.m it was used to identify so-called 'spikes' in the data set. Spikes are electronic impulses that falsely trigger recording.

F.2 Location and Waveform Discrimination

- **gorloc** by N. Deichmann. This FORTRAN program locates icequakes on Gornegletscher using hand-picked P and S arrival times. For a description see Chapter 4.
- **gse2xcor** by N. Deichmann. This FORTRAN program performs the cross-correlation search described in Chapter 4 using gse2 data.
- **seg2xcor** by N. Deichmann. This FORTRAN program performs an equivalent cross-correlation search to the one described in Chapter 4 using seg data.
- **filteralg.m** by F. Walter. This very simply but effective Matlab script searches a gse2 data set for events whose dominating phase is most likely a P or an S wave. It looks for the dominant phase in a seismogram and counts how many samples make up this phase. As surface events are dominated by low frequent Rayleigh waves, the program can sort this type of events out and can thus indicate deep icequakes.

F.3 Waveform Modelling

- **reflectivity** by T. Forbriger. This FORTRAN and C package was used to model seismograms at glacier dimensions. It played an important role in the verification of the frequency-distance scaling originally used in the moment tensor inversion (Chapter 2). However, I ended up using the FKRPROG software by C. Saikia together with putmt_minson more frequently to model seismograms.
- **tdmt_inv** by D. Dreger. This software package was used in the moment tensor inversions using scaled 1D Green's Functions as described in Chapter 2. Two versions are available. The first one can only be used to calculate deviatoric moment tensors, whereas the second one can be applied to deviatoric as well as full moment tensors with an isotropic component. In order to process the data prior to the inversion, the package makes use of the SAC and the helm format, the latter being an ascii-based format developed at Caltech, I believe. I wrote a Matlab routine, called read_helm.m, which can read this format. SAC has to be used to convert the gse2 icequake data into SAC format. Subsequently, the PERL script prepdata.pl writes the necessary entries into the SAC header and filters, integrates and interpolates the time series. It also performs the frequency and distance scaling. Green's Functions used by the inversion are calculated with the program FKRPROG by C. Saikia, which is also part of this package. The actual moment tensor inversion is performed with the programs tdmt_invc (deviatoric) and tdmtiso_invc (full), which are also part of this package. These inversion schemes use the fundamental fault formalism as described in Chapter 2. Note that the plotting of the output of the moment tensor inversions by D. Dreger and S. Minson requires conversion to postscript using the program psigl.
- **grid_cdc** by D. Dreger and S. Minson. This software package performs a grid search moment tensor inversion constraining the solution to be tensile crack plus double-couple (Chapter 2). The Green's Functions of the tdmt_inv inversion are

used. I slightly changed it to allow for variable Poisson's ratios, which can be specified in the input file. In order to plot the waveform fits of a specific tensile crack plus double-couple moment tensor, the program `grid_cdc_plot` can be used. A program that allows for a grid search of explosion plus double-couple mechanism is also available (`grid_expdc`).

- **putmt_minson** by D. Dreger and S. Minson. This program can be used to produce synthetic seismograms of a user-specified moment tensor source and source-station azimuth using the binary output of the FKRPROG software.
- **putmt_walter** by F. Walter. This is equivalent to `putmt_minson`, however it uses vector dipoles rather than fundamental faults.
- **stplot** by B. Julian. Software package that can be used to produce source-type plots after Hudson et al. (1989).
- **fd3d** by K. Olsen. This is a parallelized finite difference FORTRAN code used to produce synthetic seismograms in a 3D medium. It can be applied to glacier dimensions. The code was used to generate the vector dipole Green's Functions used in the moment tensor inversions of the basal events described in Chapter 3.
- **mt_3dinv.m** by F. Walter. This is a Matlab script, which performs the moment tensor inversion using 3D Green's Functions. The data and Green's Functions preparation is equivalent to `tdmt_inv`, however, the inversion is based on vector dipole Green's Functions and not on fundamental fault Green's Functions. Note that this script reads time series in helm format.
- **mtgrid.m** and **mtgrid_cdc.m** by F. Walter. These are the grid search moment tensor inversions equivalent to `grid_cdc` with and without double-couple component, respectively. However, they are based on vector dipole Green's Functions and not on fundamental fault Green's Functions. The same Green's Functions as in `mt_3dinv.m` are used. Note that this script reads time series in helm format.

Bibliography

- Aki, K. and Richards, P. G. (2002). *Quantitative Seismology*. University Science Books, Sausalito, California, second edition.
- Akima, H. (1978). A method of bivariate interpolation and smooth surface fitting for irregularly distributed data points. *ACM Transactions on Mathematical Software*, 4:148–159.
- Almendros, J., Ibáñez, J. M., Aluacil, G., and Del Pezzo, E. (1999). Array analysis using circular-wave-front geometry: an application to locate the nearby seismo-volcanic source. *Geophysical Journal International*, 136:159–170.
- Anandkrishnan, S. and Alley, R. B. (1994). Ice Stream C, Antarctica, sticky spots detected by microearthquake monitoring. *Annals of Glaciology*, 20:183–186.
- Anandkrishnan, S. and Alley, R. B. (1997a). Tidal forcing of basal seismicity of ice stream C, West Antarctica, observed far inland. *Journal of Geophysical Research*, 102(B7):15183–15196.
- Anandkrishnan, S. and Alley, R. B. (1997b). Stagnation of ice stream C, West Antarctica by water piracy. *Geophysical Research Letters*, 24(3):265–268.
- Anandkrishnan, S. and Bentley, C. R. (1993). Micro-earthquakes beneath Ice Streams B and C, West Antarctica: observations and implications. *Journal of Glaciology*, 39(133):455–462.
- Aschwanden, A. (1992). Gletscherbeben: Untersuchungen am Gornergletscher 1979, Diplomarbeit an der VAW/ETH-Zürich (unpublished).
- Aschwanden, H. and Leibundgut, C. (1982). Die Markierung der Wasser des Gornerseesausbruchs mit drei Fluoreszenztracern. In Leibundgut, C. and Weingartner, R., editors, *Tracermethoden in der Hydrologie, Beiträge zur Geologie der Schweiz*, volume 28, pages 535–549.
- Bensen, G. D., Ritzwoller, M. H., Barmin, M. P., Levshin, A. L., Lin, F., Moschetti, M. P., Shapiro, N. M., and Yang, Y. (2007). Processing seismic ambient noise data to obtain reliable broad-band surface wave dispersion measurements. *Geophys. J. Int.*, 169:1239–1260.
- Bezinge, A., Perreten, J., and Schafer, F. (1973). Phénomènes du lac glaciaire du Gorner. In *Symposium on the Hydrology of Glaciers, Cambridge 1969*, volume 95, pages 65–78. Association Internationale d’Hydrologie Scientifique.

- Björnsson, H. (2002). Subglacial lakes and jökulhlaups in Iceland. *Global and Planetary Change*, 35:255–271.
- Boatwright, J. (1980). A spectral theory for circular seismic sources; simple estimates of source dimension, dynamic stress drop, and radiated seismic energy. *Bull. Seism. Soc. Am.*, 68:1117–1131.
- Bowers, D. and Hudson, J. A. (1999). Defining the scalar moment of a seismic source with a general moment tensor. *Bull. Seism. Soc. Am.*, 89(5):1390–1394.
- Brüstle, W. and Müller, G. (1983). Moment and duration of shallow earthquakes from Love-wave modelling for regional distances. *Physics of the Earth and Planetary Interiors*, 32:321–324.
- Burtin, A., Bollinger, L., Vergne, J., Cattin, R., and Nábělek, J. L. (2008). Spectral analysis of seismic noise induced by rivers: A new tool to monitor spatiotemporal changes in stream hydrodynamics. *Journal of Geophysical Research*, 113(B05301). doi:10.1029/2007JB005034.
- Chouet, B. (1979). Sources of seismic events in the cooling lava lake of kilauea iki, hawaii. *Journal of Geophysical Research*, 84(B5):2315–2330.
- Clarke, G. K. C. (2003). Hydraulics of subglacial outburst floods: new insights from the Spring-Hutter formulation. *Journal of Glaciology*, 49(165):299–313.
- Clinton, J. F., Hauksson, E., and Solanki, K. (2006). An evaluation of the scsn moment tensor solutions: Robustness of the m_w magnitude scale, style of faulting and automation of the method. *Bulletin of the Seismological Society of America*, 96(5):1689–1705.
- Danesi, S., Bannister, S., and Morelli, A. (2007). Repeating earthquakes from rupture of an asperity under an Antarctic outlet glacier. *Earth and Planetary Science Letters*, 253:151–158.
- Das, S. B., Joughin, I., Behn, M. D., Howat, I., King, M. A., Lizarralde, D., and Bhatia, M. P. (2007). Direct Observations of Melt-Water Lake Drainage and the Establishment of an Efficient Surface to Basal Water Connection on the Greenland Ice Sheet. *Eos Trans. AGU*, 88(52). Fall Meet. Suppl.
- Deichmann, N., Ansorge, J., Scherbaum, F., Aschwanden, A., Bernhardt, F., and Gudmundsson, G. H. (2000). Evidence for deep icequakes in an Alpine glacier. *Annals of Glaciology*, 31:85–90.
- Deichmann, N. and Garcia-Fernandez, M. (2002). Rupture geometry from high-precision relative hypocenter locations of microearthquakes clusters. *Geophys. J. Int.*, 110:501–517.
- Del Pezzo, E., Rocca, M. L., and Ibanez, J. (1997). Observations of high-frequency scattered waves using dense arrays at teide volcano. *Bulletin of the Seismological Society of America*, 87(6).
- Dreger, D. S. (2003). TDMT_INV: time domain seismic moment tensor inversion. in *International Handbook of Earthquake and Engineering Seismology*, W. H. K. Lee, H. Kanamori, P. C. Jennings, and C. Kisslinger (Editors), Vol. B, Academic Press, London:1627 pp.

- Dreger, D. S., Tkalčić, H., and Johnston, M. (2000). Dilatational processes accompanying earthquakes in the long valley caldera. *Science*, 288(5463):122–125.
- Dreger, D. S. and Woods, B. (2002). Regional distance seismic moment tensors of nuclear explosions. *Tectonophysics*, 356(1-3):122–125.
- Dufumier, H. and Rivera, L. (1997). On the resolution of the isotropic component in moment tensor inversion. *Geophys. J. Int.*, 131(3):595–606.
- Eisen, O., Bauder, A., Lüthi, M., Riesen, P., and Funk, M. (2008). Deducing the thermal structure in the tongue of Gornergletscher, Switzerland, from radar surveys and borehole measurements (in press). *Annals of Glaciology*.
- Ekström, G., Nettles, M., and Abers, G. (2003). Glacial earthquakes. *Science*, 302(5645):622–624.
- Ekström, G., Nettles, M., and Tsai, V. C. (2006). Seasonality and Increasing Frequency of Greenland Glacial Earthquakes. *Science*, 311:1756–1758.
- Faillietaz, J., Pralong, A., Funk, M., and Deichmann, N. (2008). Evidence of log-periodic oscillations and increasing icequake activity during the breaking-off of large ice masses. *Journal of Glaciology*, 54(187):725–737.
- Fountain, A. G., Schlichting, R. B., Jacobel, R. W., and Jansson, P. (2005). Fractures as main pathways of water flow in temperate glaciers. *Nature*, 433:618–621.
- Funk, M. and Röthlisberger, H. (1989). Forecasting the effects of a planned reservoir that will partially flood the tongue of Unteraargletscher in Switzerland. *Annals of Glaciology*, 13:76–80.
- Gischig, V. (2007). Seismic Investigations on Gornergletscher. Diplomarbeit, Abteilung für Glaziologie, VAW (unpublished), ETH–Zürich.
- Haeberli, W. (1983). Frequency and characteristics of glacier floods in the Swiss Alps. *Annals of Glaciology*, 4:85–90.
- Hanks, T. C. and Kanamori, H. (1979). A moment magnitude scale. *Journal of Geophysical Research*, 84(B5):2348–2350.
- Harper, J. T. and Humphrey, N. F. (1995). Borehole video analysis of a temperate glacier's englacial and subglacial structure: Implications for glacier flow models. *Geology*, 23(10):901–904.
- Hudson, J. A., Pearce, R. G., and Rogers, R. M. (1989). Source type plot for inversion of the moment tensor. *Journal of Geophysical Research*, 94:765–774.
- Huss, M. (2005). Gornergletscher — Gletscherseeausbrüche und Massenbilanzabschätzungen (in German with English summary). Diplomarbeit, Abteilung für Glaziologie, VAW (unpublished), ETH–Zürich. pp. 176.
- Huss, M., Bauder, A., Werder, M., Funk, M., and Hock, R. (2007). Glacier-dammed lake outburst events of Gornensee, Switzerland. *Journal of Glaciology*, 53(181):189–200.

- Iken, A. (1981). The effect of the subglacial water pressure on the sliding velocity of a glacier in an idealized numerical model. *Journal of Glaciology*, 27(97):407–421.
- Jean-Philippe Métaixian, Sebastián Araujo, M. M. and Lesage, P. (2003). Seismicity related to the glacier of Cotopaxi Volcano, Ecuador. *Geophysical Research Letters*, 30(9).
- Jost, M. L. and Herrmann, R. B. (1989). A Student's Guide to and Review of Moment Tensors. *Seismological Research Letters*, 60(2):37–57.
- Joughin, I., Howat, I., Alley, R. B., Ekstrom, G., Fahnestock, M., Moon, T., Nettles, M., Truffer, M., and Tsai, V. (2008). Ice-front variation and tidewater behavior on Helheim and Kangerdlugssuaq Glaciers, Greenland. *Journal of Geophysical Research*, 113:F01004(11 pp.).
- Julian, B. R., Miller, A. D., and Foulger, G. R. (1998). Non-double-couple earthquakes (theory). *Reviews of Geophysics*, 36(4):525–549.
- Julian, B. R. and Sipkin, S. A. (1985). Earthquake processes in the long valley caldera area, California. *Journal of Geophysical Research*, 90:11,155–11,169.
- Knecht, H. and Süssstrunk, A. (1952). Bericht über die seismischen Sondierungen der schweizerischen Gletscherkommission auf dem Unteraargletscher, 1936 - 1950. Bericht No. 512.
- Knopoff, L. and Randall, M. J. (1970). The compensated linear vector dipole: A possible mechanism for deep earthquakes. *Journal of Geophysical Research*, 75:4957–4963.
- Lee, W. H. K. and Stewart, S. W. (1981). *Principles and application of microearthquake networks, Advances in Geophysics Suppl. II*. Academic Press.
- Meierbachtol, T. W., Harper, J. T., Humphrey, N. F., and Bradford, J. (2006). Englacial and subglacial water flow elucidated by active and passive borehole experiments: Bench Glacier, Alaska. *Eos Trans. AGU*, 87(52). Fall Meet. Suppl., Abstract C31A-1229.
- Menke, W. (1989). *Geophysical Data Analysis: Discrete Inverse Theory*. Academic Press, San Diego, California.
- Minson, S. E. and Dreger, D. S. (2008). Stable inversions for complete moment tensors. *Geophysical Journal International*, 174(2):585–592.
- Minson, S. E., Dreger, D. S., Bürgmann, R., Kanamori, H., and Larson, K. M. (2007). Seismically and geodetically determined nondouble-couple source mechanisms from the 2000 Miyakejima volcanic earthquake swarm. *Journal of Geophysical Research*, 112. B10308.
- Müller, G. (1985). The reflectivity method: A tutorial. *Journal of Geophysical Research*, 58:153–174.
- Müller, G. (2001). Volume change of seismic sources from moment tensors. *Bulletin of the Seismological Society of America*, 91:880–884.
- Neave, K. G. and Savage, J. C. (1970). Icequakes on the Athabasca glacier. *Journal of Geophysical Research*, 75(8):1351–1362.

- Nye, J. F. (1976). Water flow in glaciers: jökulhlaups, tunnels and veins. *Journal of Glaciology*, 17(76):181–207.
- Olsen, K. B. (1994). *Simulation of three-dimensional wave propagation in the Salt Lake Basin*. Ph. D. Thesis, University of Utah, Salt Lake City.
- O’Neel, S., Marshall, H., McNamara, D., and Pfeffer, W. T. (2007). Seismic detection and analysis of icequakes at Columbia Glacier, Alaska. *Journal of Geophysical Research*, 112. F03S23.
- O’Neel, S. and Pfeffer, W. T. (2007). Source mechanisms for monochromatic icequakes produced during iceberg calving at Columbia Glacier, AK. *Geophysical Research Letters*, 34. L22502.
- Paterson, W. S. B. (1994). *The Physics of Glaciers*. Pergamon, New York, third edition.
- Prieto, G. A. and Beroza, G. C. (2008). Earthquake ground motion prediction using the ambient noise field. *Geophysical Research Letters*, 35. doi:10.1029/2008GL034428.
- Raymond, M., Wegmann, M., and Funk, M. (2003). Inventar gefährlicher Gletscher in der Schweiz. Mitteilung 182, Versuchsanstalt für Wasserbau, Hydrologie und Glaziologie der ETH Zürich.
- Richardson, S. and Reynolds, J. (2000). An overview of glacial hazards in the Himalayas. *Quaternary International*, 66(8):31–47.
- Riesen, P. (2007). Investigation of glacier flow during two ice-dammed lake outburst events on Gornergletscher, Valais, Switzerland, by using a three-dimensional numerical model (unpublished). Diplomarbeit, Abteilung für Glaziologie, VAW, ETH–Zürich.
- Roberts, M. J. (2005). Jökulhlaups: a reassessment of floodwater flow through glaciers. *Reviews of Geophysics*, 43(RG1002):doi:10.1029/2003RG000147.
- Roberts, M. J., Russell, A. J., Tweed, F. S., and Knudsen, O. (2000). Ice fracturing during jökulhlaups: implications for englacial floodwater routing and outlet development. *Earth Surface Processes and Landforms*, 25:1429–1446.
- Rost, S. and Thomas, C. (2002). Array seismology: methods and applications. *Reviews of Geophysics*, 40(3).
- Roux, P.-F. (2008). *Méthodes sismologiques pour l’étude de la fracturation dans les glaciers alpins: glaciers d’Argentière et du Gorner*. Ph. D. Thesis, Université de Savoie.
- Roux, P.-F., Marsan, D., Métaixian, J.-P., O’Brien, G., and Moreau, L. (2008). Microseismic activity within a serac zone in an alpine glacier (Glacier d’Argentière, Mont Blanc, France). *Journal of Glaciology*, 54(184):157–168.
- Saikia, C. K. (1994). Modified frequency-wavenumber algorithm for regional seismograms using Filon’s quadrature: Modelling Lg waves in eastern North America. *Geophys. J. Int.*, 118(1):142–158.
- Shapiro, N. M., Campillo, M., Stehly, L., and Ritzwoller, M. H. (2005). High-resolution surface-wave tomography from ambient seismic noise. *Science*, 307:1615–1618.

- Smith, A. M. (2006). Microearthquakes and subglacial conditions. *Geophysical Research Letters*, 33(24).
- Spring, U. and Hutter, K. (1981). Numerical studies of Jökulhlaups. *Cold Regions Science and Technology*, 4:221–244.
- Stuart, G. (2005). Seismic emissions from a surging glacier: Bakaninbreen svarlbard. *Annals of Glaciology*, 42:151–157.
- Sugiyama, S., Bauder, A., Huss, M., Riesen, P., and Funk, M. (2008). Triggering and drainage mechanisms of the 2004 glacier-dammed lake outburst in Gornergletscher, Switzerland (in press). *Journal of Geophysical Research*.
- Sugiyama, S., Bauder, A., Weiss, P., and Funk, M. (2007). Reversal ice motion during the outburst of a glacier-dammed lake on Gornergletscher, Switzerland. *Journal of Glaciology*, 53(181):172–180.
- Sugiyama, S. and Gudmundsson, G. H. (2003). Diurnal variations in vertical strain observed in a temperate valley glacier. *Geophysical Research Letters*, 30(2):1090. doi:10.1029/2002GL016160, 2003.
- Sugiyama, S. and Gudmundsson, G. H. (2004). Short-term variations in glacier flow controlled by subglacial water pressure at Lauteraargletscher, Bernese Alps, Switzerland. *Journal of Glaciology*, 50(170):353–362.
- Templeton, D. C. and Dreger, D. S. (2006). Non-double-couple earthquakes in the long valley volcanic region. *Bulletin of the Seismological Society of America*, 96(1):69–79.
- Tsai, V. C. and Ekström, G. (2007). Analysis of glacial earthquakes. *Journal of Geophysical Research*, 112(F03S22).
- Tsai, V. C., Rice, J. R., and Fahnstock, M. (2008). Possible mechanisms for glacial earthquakes. *Journal of Geophysical Research*, 113(F03014).
- Turcotte, D. L. and Schubert, G. (2002). *Geodynamics*. Cambridge University Press, second edition.
- Ungerer, J. (1990). Berechnung von Nahfeldseismogrammen mit der Reflektivitätsmethode. Diplom, Institut für Geophysik, Universität Stuttgart, Germany.
- Van der Veen, C. J. (1998a). Fracture mechanics approach to penetration of bottom crevasses on glaciers. *Cold Regions Science and Technology*, 27(3):213–223.
- Van der Veen, C. J. (1998b). Fracture mechanics approach to penetration of surface crevasses on glaciers. *Cold Regions Science and Technology*, 27(1):31–47.
- Van der Veen, C. J. (2007). Fracture propagation as means of rapidly transferring surface meltwater to the base of glaciers. *Geophysical Research Letters*, 34(L01501):doi:10.1029/2006GL028385.
- Walter, F., Clinton, J. F., Deichmann, N., Dreger, D. S., Minson, S. E., and Funk, M. (2009). Moment Tensor Inversions of Icequakes on Gornergletscher, Switzerland. *Bulletin of the Seismological Society of America*, 99-2A. doi:10.1785/0120080110.

- Walter, F., Deichmann, N., and Funk, M. (2008). Basal icequakes during changing subglacial water pressures beneath Gornergletscher, Switzerland. *Journal of Glaciology*, 54(186):511–521.
- Weaver, C. S. and Malone, S. D. (1979). Seismice evidence for discrete glacier motion at the rock-ice interface. *Journal of Glaciology*, 23(89):171–183.
- Weiss, P. (2005). Gletscherdynamik vor und nach der Entleerung des Gornersees im Sommer 2004. Diplomarbeit, Abteilung für Glaziologie, VAW (unpublished), ETH–Zürich. pp. 149.
- Werder, M. A. and Funk, M. (2009b). Dye tracing a jökulhlaup (Part ii): Testing a jökulhlaup model against measured flow speeds (submitted). *Journal of Glaciology*.
- Werder, M. A., Loye, A., and Funk, M. (2009a). Dye tracing a jökulhlaup (Part i): Subglacial water-flow speeds and water-storage mechanisms (submitted). *Journal of Glaciology*.
- Wiens, D. A., Anandakrishnan, S., Winberry, J. P., and King, M. A. (2008). Simultaneous teleseismic and geodetic observations of the stick-slip motion of an Antarctic ice stream. *Nature*, 453:770–775.
- Wilhelm, G. (1967). Gornersee. Rapport interne Grande Dixence (unpublished).

Acknowledgements

During the preparation of this thesis I benefitted from valuable support of my colleagues, friends and family. Whether I received help in form of advice in different areas of geophysics, financial support, technical help with software packages and physical labor or in form of patience and encouragement, I would like to extend my gratitude to all people who assisted me during my Ph. D. work in one way or another.

First, I would like to thank my doctoral supervisor (“Doktorvater”) Professor Martin Funk for giving me the opportunity to perform research in the fields of glaciology and seismology. Since the beginning of my Ph. D. work I have been convinced that no other topic would have equally appealed to my interests and academic background. Prof. Funk gave me the freedom to direct my research towards aspects of source seismology which led to the calculation of moment tensors of icequake sources. In general, I always felt sure of his support as he made it possible for me to attend several helpful conferences, provided means to conduct extensive field measurements and offered financial support throughout my time at VAW. His willingness to help, listen and share his competence promptly at any time and without hesitation is highly appreciated.

Furthermore, I am grateful to my advisor Dr. Nicholas Deichmann, who provided help particularly with the seismological component of this work. He offered indispensable knowledge and practical experience in glacier seismology both in front of a computer screen and on glacier ice. When processing and analyzing seismic data, installing seismometers or interpreting seismograms I could build on his experiences and knowledge, which he had acquired over decades of research.

By offering expertise on moment tensor inversions Dr. John Clinton made the core part of my research possible. He thus initiated my interest in source seismology and broadened my horizon in many fields of seismological research. I appreciate very much his high interest in icequake source physics and in helping me out whenever I felt stuck or needed to discuss parts of my research.

As the external co-referee of my thesis, Professor Douglas Dreger not only provided valuable insights into source seismology but also made available his software packages for the 1D moment tensor inversion and helped implement the 3D inversion scheme. I very much benefitted from the stay with his group at the Berkeley Seismological Laboratory and from the time he took to assist me in my thesis and to explain seismological principles.

I would also like to express gratitude to Professor Domenico Giardini for serving on my thesis committee and for his interest in the project and collaboration with the VAW. He offered very constructive and precise comments that significantly enhanced the quality of my thesis.

In the field as well as in the office I had the support of a number of colleagues who helped me to get things done, shared their knowledge or were good company when I waited for Gornersee to drain. I benefitted a lot from the work with my fellow Ph. D. student Mauro Werder, who always offered help with programming problems, and numerous times took care of the seismic recording during my absence on Gornergletscher. Our discussions helped me understand many aspects of the Gornersee drainage better. The sunrises on Jägerhorn, the evenings at the “Gorner Base Camp”, and the Pollux attempt were some of the experiences which more than compensated for the hard work, stress and frustration often related to Ph. D. research. Similarly, I would like to thank the third Ph. D. student of the Gorner project, Patrick Riesen, who helped me analyze surface flow data and also spent many days on Gornergletscher with me. Witnessing the calving event in 2007, we arguably spent the two most eventful minutes of fieldwork on Gornergletscher together. As another faithful field companion, Bruno Nedela deserves much of my appreciation. Besides being good company during the “waiting periods” he also took care of our culinary needs and thus was an important component of the fieldwork and of the entire project.

I very much enjoyed working with Valentin Gischig, who as a diploma student performed a seismic tomography study on Gornergletscher with data from active seismic measurements. His help with field work and the findings of his diploma thesis were valuable contributions to my research. Furthermore, I would like to thank Jed Brown and Stefan Heimers for their explanations, time, help and patience concerning installing and debugging C and Fortran code. Without their help I could not have installed and modified the source codes needed to perform the moment tensor inversion.

This work was funded by the Swiss National Science Foundation, grants No. 200021-103882/1 and 200020-111892/1. Prof. Hansrudolf Maurer and Prof. Alan Green of the Applied and Environmental Geophysics group at ETH Zürich were very generous in loaning seismic instruments to the Gorner project. Without their support, the research presented in this thesis would not have been possible. The Swiss military supported the Gorner project through transportation of equipment with helicopters. The Grande Dixence kindly offered accomodation during field seasons and shared discharge data of the Gornera with VAW. I would also like to thank the Gornergrat Railway for providing transportation and the Kulmhotel Gornergrat for offering access to the internet, which helped with data analyses during fieldwork. In view of accomodation, the warm welcomes at the Monte-Rosa Hütte were much appreciated.

During the installation and maintenance of the seismic networks on Gornergletscher I was heavily dependent upon the help of fellow students and volunteers. As the monotonous task of reinstalling and aligning seismometers was rather laborious yet absolutely crucial on a daily basis, I owe much thanks to a number of people from inside as well as outside of ETH. In addition, the installation and dissembling of the networks as well as the conducting of active seismic measurements were possible only with willing and enthusiastic helpers. Their names are (in alphabetical order): Pablo Ampuero, Caro Antoni, Sacha Barman, Andreas Bauder, Andre Blanchard, Christina Bucher, Ruzica Dadic, Olaf Eisen, Flurina Gerber, Rico Gutzler, Jörg Hillesheim, Huw Horgan, Stephan Husen, Matthias Huss, Albin Kretz, Alexandre Loye, Martin Lüthi, Beat Rinderknecht, Pierre-Francois Roux, Cornerlius Senn, Shin Sugiyama, Stephen Szoradi, Patrik Weiss and Thomas Wyder.

In general I benefitted from the friendly atmosphere at VAW during mensa lunches, Ar-

venstübli breaks and the dinners in the kitchen tent during field work. I would like to express gratitude to all who contributed to this atmosphere and who took time to talk, laugh and discuss with me. In this context I would like to mention the names of (in alphabetical order) Andy Aschwanden, Hermann Bösch, Pierre Dalban, Urs Fischer, Jakob Helbing, Arne Keller, Sarah Minson, Antoine Pralong, Marie Rousselot, Roger Ruegg, Claudia Ryser, Aurel Schwerzmann, Tetsuo Sueyoshi, Martin Truffer, Giuliana Turi, Stephanie Usselman, as well as my two office mates Daniel Farinotti and Melanie Raymond Pralong.

Finally, I would like to express the deepest gratitude to my parents. They always wanted the best for me, showed great interest in my studies of natural sciences, took time to listen to my problems and suffered with me through difficult times. Needless to say that without their support my academic development, culminating with this thesis, would not have been possible.